

Université du Québec  
Institut National de la Recherche Scientifique  
Center for Materials, Energy and Telecommunications

**PARTICLE SIZE EFFECT ON THE PHOTOCATALYTIC KINETICS OF  
PYROELECTRIC BARIUM TITANATE PARTICLES**

By

Ifeanyichukwu Chinedu, AMAECHI

Thesis presented for the degree of  
Doctor of Philosophy, Ph.D.  
in Materials Science and Energy

**Evaluation committee**

President of the Jury: (Internal examiner)	Prof. Fiorenzo VETRONE Institut National de la Recherche Scientifique Centre Énergie Matériaux et Télécommunication
External examiner:	Prof. Bertrand VILQUIN Institut des Nanotechnologies, Ecole Centrale de Lyon, France
External examiner:	Prof. Rüdiger-A. EICHEL Institut für Energie- und Klimateforschung, Forschungszentrum Jülich, Germany
Research co-supervisor:	Prof. Shuhui SUN Institut National de la Recherche Scientifique Centre Énergie Matériaux et Télécommunication
Research supervisor:	Prof. Andreas RUEDIGER Institut National de la Recherche Scientifique Centre Énergie Matériaux et Télécommunication



# Dedication

To God Almighty, my lovely (♡) wife, Seraphine and son, Ifeanyichukwu (Jnr.) and finally in loving memory of my parents, Mr. & Mrs. Vincent Amaechi.



# Acknowledgments

While the journey was a bit tiresome and adventurous, the hope of better tomorrow became the gentle nudge and I wholly thank God for HIS divine enablement and providence. First of all, I am grateful to the Center for Energy, Materials and Telecommunications, Institut National de la Recherche Scientifique, EMT-INRS (Varennes, Canada) that provided the conducive environment to carry out my Ph.D. research. Again, this would not have been possible without the financial support through the prestigious MATECSS Excellence scholarship. I therefore sincerely acknowledge the coordinators especially Prof. Federico Rosei and Dr. Louis Vervoort of the UNESCO Chair in Materials and Technologies for Energy Conversion, Saving and Storage (MATECSS) for this wonderful outreach.

My profound gratitude goes to my research supervisors, Profs. Shuhui Sun (Co-supervisor) and Andreas Ruediger (Supervisor) for their encouragement, patience, and ultimately the support given to me in various forms. The day-to-day fruitful discussions culminating to this very piece of work are deeply appreciated and will not be forgotten in a haste. Many thanks to you, Andreas especially for completely changing my understanding about science. You do everything possible to expand students' knowledge. I won't forget your common statement, "come on, let's go to my office" :-). One of my native adages says "Uzo di mma, aga ya ugboro abuo" but with the joint supervision of both of you, I say "Uzo di mma, aga ya ugboro iri". I wish to let you know that gratitude will never cease the tongue. I am also thankful to Prof. Jérôme Claverie of the University of Sherbrooke (Sherbrooke, Canada) whose collaboration launched the superficial consideration of the surface chemistry related to the photocatalytic activity section, though yet to be fully explored. Lest I forget, I thank Prof. Carlos Gomez-Yáñez for his assistance in carrying out the Brunauer-Emmett-Teller (BET) surface area and differential scanning calorimetry (DSC) measurements during my one month visit to his laboratory at the Instituto Politécnico Nacional, (Mexico city, Mexico).

A special thanks goes to my family for their support throughout the dark times. I would rather say that “we have seen misfortune, and felt the sting of defeat; the humility of empty stomach and vacant purse; some believed we would never reclaim the former glories that we will fade from memories forsaken by history but we have proved them wrong. I know it is not all that wished it, yet it is DONE! It is DONE!!”. To my lovely wife, I would like to express my deepest appreciation for taking care of our son; Ifeanyichukwu (Jnr.), even though am yet to lay eyes, I love you from the moment you opened your eyes and most importantly for keeping watch while am away. My baby girl, Nkwachi, many thanks to you for taking care of things in my absence. Prof. (Mrs.) Rose U. Osuji, you have always been a mother and aimed a favour towards all of us; finding out how we all in diaspora are faring. May God still preserve you. Am also beholden to my amiable Head of Department of Physics/Astronomy of the University of Nigeria Nsukka, Prof. Azubike B. C. Ekwealor for his pieces of advice. I am grateful to Chief & Mrs. Kenneth Duru for providing a second home for me. Your family indeed provided the comfort I really needed and made me less homesick, an association that must be studied, emulated and reproduced in kind. For your countless supports and encouragements amid the dark times, I would rather say “onye dika gi akola m”.

Notwithstanding the academic hitch and pressure, I would not fail to appreciate the companionship of colleagues that made my stay even more memorable all this years. Colleagues from my group (Nanophotonics-Nanoelectronics), I just hope the chronological order is correct: Jiawei Zhang, Mohamed Swaisi, Mohamed Delfag, Aura Daniela Lubio, Maria Dekermenjian, Yoandris González-Hernández, Lilian Skokan, Peipei Liu, Andreas Doerfler, Drs. Azza Hadj Youssef, Bernhard Huber, Chahinez Dab, Binod Bastola, Fabian Ambriz-Vargas, Julien Plathier, Gitanjali Kolhatkar and Rajesh Katoch, your friendship and contributions had never gone unnoticed. I therefore thank you all for your individual supports especially Azza, Yoandris, Julien, Gitanjali & Rajesh. Another special thanks goes to Azza for assisting me with the French translation of this work. In the same vein, my appreciation goes to the group members of my co-supervisor, Prof. Shuhui Sun. They have all been wonderful especially Xiaohua Yang. Lest I forget, my sister, Ivy Asuo, you are one in a million; thank you once again for being there. The INRS soccer team (Drs. Alonso Moreno, Etienne Yvenou, Riad Nechache; Saeed Mohammadkhani, Andrea La Monaca, Mohamed Fatahine, Mohamed Delfag, Patrick Soucy etc.), you people made it less boring coming to INRS. Christophe Chabanier, Hélène Tanguay, Hélène Sabourin and all the administrative staffs, many thanks to you all.

# Abstract

Provision of portable and safe drinking water is currently challenging and one of the ways to meet this need is through sustainable wastewater treatment technology. The technology is considered energy and also chemically intensive. We pursued both goals by using a scalable non-centrosymmetric nanomaterial with enhanced visible-light absorption. Thus, a facile and viable microwave-assisted hydrothermal technique was adopted for the synthesis of photo-pyroelectric Cr- and Fe-doped barium titanate nanoparticles. Since bimetallic oxide pyroelectrics generally suffer from leakage current, our synthetic strategy is through hydroxylation with hydrogen peroxide to scavenge excess protons. This regulates the internal lattice defects manifesting in form of lattice hydroxyl group,  $(OH)_O^\bullet$  incorporated on oxygen site in the oxide perovskite responsible for the leakage current. We next demonstrated the implementation of these photo-pyroelectric nanostructures in the photocatalytic degradation of one of the standard industrial effluents, methylene orange (MO) under simulated solar irradiation. The optical absorption studies investigated through UV-Vis-NIR absorption spectroscopy revealed a substantial absorption band due to strong electron-phonon coupling in the material (especially for the 8 mol% Fe of the co-doped system). The additional absorption band corresponding to an absorption edge of 2.7 eV (Cr-doped) and 2.4 eV (Fe-doped) as against the intrinsic absorption band (3.18 eV) of undoped  $BaTiO_3$  nanoparticles were obtained. Further redshift of the absorption edge was even obtained for the co-doped pyroelectric systems when Cr, Fe and Ti cationic orderings are modulated. For instance, the Fe and Cr compositional ratio of 1:1 yielded an absorption edge of 2.3 eV whereas that of 2:1 gave 1.7 eV. The photocatalytic activity of both mono- and co-doped  $BaTiO_3$ pyroelectrics prepared by this method exceeded that of the undoped lattice and showed strong correlation with intense light absorption under identical conditions. In terms of the degradation kinetics, the co-doped pyroelectrics with compositional ratio of 1:1 exhibited nearly a three-fold increase i.e.  $\sim (28.0 \pm 0.5) \times 10^{-3}$  min<sup>-1</sup> in

comparison to the undoped structure i.e.  $\sim (8.4 \pm 0.1) \times 10^{-3}$  min<sup>-1</sup>. As total quantum efficiency depends on efficiency of various processes expressed as  $\eta_T = \eta_{absorption} \times \eta_{e^-/h^+ separation} \times \dots$ , which have multiplicative effect, the enhancement is not only attributed to light absorption but also other factors like sufficient polarization-induced charge carrier separation furnished by a bulk photovoltaic effect due to the broken-inversion symmetry of the material. While optical excitation of the defect centers may yet be advantageous in creating extra absorption, they are hub for charge carrier recombination and reduce the density of charges available for surface chemistry which in turn affects the photochemical catalyzation as witnessed when the Fe 3+ content was higher than a threshold. Based on XPS analysis, the trend of molar fraction of Ti 4+ state in these systems indicated an increasing number of defects (i.e. Ti 3+ state compensated by oxygen vacancy) especially for the co-doped lattices. Moreover, the complementary result from XRD shows that for a 1:1 compositional ratio, a biphase of tetragonal and hexagonal coexist, which favours the latter in the presence of high volume of oxygen vacancies,  $V_O^{..}$ .

The nanoscale optimization of bulk photovoltaic effect for a better catalytic design led to the study of particle size effect on the photocatalytic kinetics. To this effect, both commercially available and microwave-assisted hydrothermally synthesized BaTiO<sub>3</sub> ultrafine particles are used. Varying particle sizes ranging from  $\sim 3$   $\mu$ m to 9 nm confirmed through TEM were used to degrade aqueous solution of MO. The properties such as unit cell distortion ( $c/a - 1$ ) and Curie temperature ( $T_C$ ) investigated by means of XRD and Raman spectroscopy were used as indicators to monitor the size-driven transition into the centrosymmetric phase. The experimental results were compared to two models, namely the Landau-Ginzburg-Devonshire (LGD) model - for structure, and the thermodynamic model - mass transport at the solid catalyst-liquid interface. Experimental results obtained from UV-Vis-NIR absorption spectroscopy confirmed that the band structures were slightly adjusted i.e.  $V_{CB} - V_{VB} > E_g$  as particle size decreases due to quantum confinement effect. The energy gap widening guarantees additional free radicals for effective photodegradation of MO. The highest photocatalytic activity was obtained when the particle size is 19 nm before experiencing a downturn; a behaviour depicting substantial loss of bulk photovoltaic effect (BPVE) in the material. Intriguingly, by using the Landau-Ginzburg-Devonshire (LGD) phenomenological model we demonstrated that the smallest particle size to retain non-centrosymmetry and therefore a BPVE contribution to the charge carrier transport and charge-consuming catalysis is in the range of  $10 \pm 4$  nm below

which the surface-specific catalytic activity would decrease. The thermodynamics formalism on the other hand yields a maximum photoactivity for particle size distribution in the range 15 - 25 nm below which processes like nanoclustering and possibly surface reconstruction dominate.

**Keywords:** Photo-pyroelectric, BaTiO<sub>3</sub>, tetragonality, photochemical catalyzation, size effect, thermodynamic, Landau-Ginzburg-Devonshire model, UV-Vis-NIR spectroscopy, Raman spectroscopy, XRD, Bulk photovoltaic effect, and XPS.



# Résumé

L'approvisionnement en eau potable est actuellement difficile et l'un des moyens pour répondre à ce besoin est de recourir à une technologie durable de traitement des eaux usées. Cette technologie est considérée comme une source d'énergie et de produits chimiques. Pour réaliser notre objectif de recherche, nous avons opté pour un nanomatériau non centrosymétrique avec une meilleure absorption de la lumière visible, le titanate de baryum ( $\text{BaTiO}_3$ ). Ainsi, la technique de synthèse hydrothermale assistée par micro-ondes a été adoptée pour la synthèse de nanoparticules de  $\text{BaTiO}_3$  dopées aux ions chromes (Cr) et aux ions fer (Fe). Étant donné que les oxydes bimétalliques et pyroélectriques sont plus sensibles aux courants de fuite, notre stratégie de synthèse est basée sur l'hydroxylation avec du peroxyde d'hydrogène pour éliminer l'excès de protons. Cela permet de contrôler les défauts du réseau interne qui se manifestent sous la forme d'un groupe hydroxyle ( $\text{OH}\cdot$ ) incorporé sur le site de l'oxygène dans la structure pérovskite responsable du courant de fuite. Nous avons démontré la mise en œuvre de ces nanostructures photo-pyroélectriques dans la dégradation photocatalytique de l'un des colorants industriels standard, le méthylène orange (MO) sous irradiation solaire simulée. Les études d'absorption optique réalisées par spectroscopie d'absorption UV-Vis-NIR ont révélé une bande d'absorption importante due à un fort couplage électron-phonon dans le matériau (en particulier pour les 8% molaires de Fe du système codopé). Cette étude a permis d'obtenir une bande d'absorption supplémentaire qui correspond à un front d'absorption de 2,7 eV (cas dopé au Cr) et de 2,4 eV (cas dopé au Fe) alors que la bande d'absorption intrinsèque des nanoparticules de  $\text{BaTiO}_3$  non dopées a été estimée de 3,18 eV. Un nouveau décalage vers le rouge du bord d'absorption a même été obtenu pour les systèmes pyroélectriques co-dopés lorsque les ordres cationiques Cr, Fe et Ti sont modulés. Dans ce projet de thèse, les résultats obtenus ont démontrés qu'une composition de 1:1 en Fe et en Cr a donné un front d'absorption de 2,3 eV alors que celle de 2:1 a donné lieu à une bande interdite de 1,7 eV.

L'activité photocatalytique des pyroélectriques BaTiO<sub>3</sub> mono- et co-dopés préparés par cette méthode dépasse celui du réseau non-dopé et met en évidence une forte corrélation avec une absorption intense de la lumière dans des conditions identiques. En termes de cinétique de dégradation, la pyroélectrique du système co-dopée avec un rapport de composition de 1:1 présente une augmentation de deux fois c'est à dire  $\sim (28,0 \pm 0,5) \times 10^{-3} \text{ min}^{-1}$  par rapport à la structure non-dopée c'est à dire  $\sim (8,4 \pm 0,1) \times 10^{-3} \text{ min}^{-1}$ . Comme l'activité quantique totale dépend de l'efficacité de divers processus exprimée par  $\eta_T = \eta_{absorption} \times \eta_{e^-/h^+ separation} \times \dots$ , qui ont un effet multiplicatif, l'amélioration n'est pas seulement attribuée à l'absorption de la lumière mais aussi à d'autres facteurs tels que la séparation des porteurs de charge induite par la polarisation fournie par un effet photovoltaïque massif dû à la symétrie d'inversion du matériau. Alors que l'excitation optique des centres de défauts peut être avantageuse en créant une absorption supplémentaire, elles sont le centre de la recombinaison des porteurs de charges et réduisent la densité des charges disponibles pour la chimie de surface qui, à son tour, influence la catalyse photochimique quand la teneur de Fe 3+ est supérieure à au seuil. Sur la base de l'analyse XPS, la tendance de la teneur molaire en Ti 4+ dans ces systèmes indiquait un nombre croissant de défauts (c'est-à-dire que Ti 3+ est compensé par la vacance d'oxygène) surtout pour les mailles co-dopés. En outre, le résultat complémentaire de la DRX montre que pour un rapport de composition de 1:1, les deux phases tétragonal et hexagonale coexistent ensemble, ce qui favorise cette dernière en présence d'un volume élevé de lacunes d'oxygène,  $V_O^{..}$ .

L'optimisation à l'échelle nanométrique de l'effet photovoltaïque pour une meilleure conception catalytique a conduit à l'étude de l'effet de la taille des particules sur la cinétique photocatalytique. A cet effet, les particules commercialisées ainsi que les nanoparticules de BaTiO<sub>3</sub> synthétisées avec la méthode hydrothermale assistées par micro-ondes sont utilisées. Des particules de tailles variables allant de  $\sim 3 \mu\text{m}$  to 9 nm, ont été observées avec le microscope électronique de transmission (TEM) et ont été utilisées pour dégrader une solution aqueuse de MO. Les propriétés telles que la distorsion des cellules unitaires ( $c/a - 1$ ) et la température de Curie ( $T_C$ ) étudiée par la DRX et la spectroscopie Raman confocal ont été utilisées comme indicateurs pour identifier la transition vers la phase centrosymétrique déterminée par l'effet de taille des nanoparticules de BaTiO<sub>3</sub>. Les résultats expérimentaux ont été comparés à deux modèles, le modèle Landau-Ginzburg-Devonshire (LGD) pour la structure, et le modèle thermodynamique - transport de masse au niveau de l'interface du catalyseur solide

– liquide. Les résultats expérimentaux obtenus par spectroscopie d'absorption UV-Vis-NIR ont confirmés que les structures des bandes ont été légèrement ajustées, équation quand la taille des particules diminue en raison de l'effet de confinement quantique. L'élargissement du fossé énergétique garantit des radicaux libres additionnels pour une photodégradation efficace du MO. L'activité photocatalytique la plus élevée a été obtenue lorsque la taille des particules est de 19 nm avant qu'elle connaisse un ralentissement; un comportement de perte substantielle de l'effet photovoltaïque du bulk (BPVE) dans le matériau. Curieusement, en utilisant le modèle de Landau-Ginzburg-Devonshire (LGD), nous avons démontré que la taille minimale nécessaire pour conserver la non-centrosymétrie et donc une contribution de BPVE au transport des porteurs de charge et à la catalyse consommatrice de charge est située dans la plage de  $10\pm4$  nm en dessous de laquelle l'activité catalytique de la surface spécifique diminue. Le formalisme de la thermodynamique d'autre part, produit une photoactivité maximale pour la distribution de la taille des particules dans la gamme 15 - 25 nm en dessous de laquelle domine des processus comme la nanoclusterisation et éventuellement la reconstruction de surface.

**Mots-clés:** Photo-pyroélectrique, BaTiO<sub>3</sub>, tétragonalité, catalyse photochimique, effet de taille, thermodynamique, modèle Landau-Ginzburg-Devonshire, UV-Vis-NIR, spectroscopie Raman, XRD, effet photovoltaïque du bulk, et XPS.



# Table of Contents

<b>Dedication</b>	iii
<b>Acknowledgments</b>	v
<b>Abstract</b>	vii
<b>Résumé</b>	xi
<b>Table of Contents</b>	xv
<b>List of Figures</b>	xix
<b>List of Tables</b>	xxiii
<b>List of Symbols &amp; Abbreviations</b>	xxv
<b>1 Introduction, objectives and plan</b>	1
1.1 Introduction . . . . .	1
1.2 Motives . . . . .	4
1.3 Research objectives . . . . .	7
1.4 Thesis plan . . . . .	8
1.5 Scientific publications . . . . .	9
<b>2 Literature review</b>	11
2.1 General principle/mechanism of redox photocatalytic process . . . . .	11
2.2 Photocatalytic semiconductors . . . . .	14
2.3 A brief overview of titanium dioxide, TiO <sub>2</sub> : Merits and demerits . . . . .	19
2.4 Barium titanate, BaTiO <sub>3</sub> , and its properties . . . . .	20

2.5	Additional mechanism of charge carrier separation in non-centrosymmetric materials: Bulk photovoltaic effect (BPVE) . . . . .	24
2.6	Relationship between crystal structure and presence of permanent dipoles . . . . .	26
2.7	Approaches to study particle size effect in non-centrosymmetric materials . . . . .	28
2.7.1	Phenomenological Landau-Ginzburg-Devonshire (LGD) formalism . . . . .	29
2.8	Size effect on the catalytic kinetics of redox reaction . . . . .	31
<b>3</b>	<b>Experimental techniques</b>	<b>35</b>
3.1	Synthesis of BaTiO <sub>3</sub> nanoparticles: Microwave-assisted hydrothermal technique . . . . .	35
3.2	Characterization techniques . . . . .	37
3.2.1	X-ray diffraction . . . . .	37
3.2.2	Raman spectroscopy . . . . .	38
3.2.2.1	Principles . . . . .	40
3.2.2.2	Modes of vibration . . . . .	40
3.2.3	X-ray photoelectron spectroscopy . . . . .	42
3.2.4	Transmission electron microscopy . . . . .	43
3.2.5	Optical absorption (UV-Vis-NIR) spectroscopy . . . . .	44
<b>4</b>	<b>Experimental results and discussion</b>	<b>47</b>
4.1	Pyroelectric doped BaTiO <sub>3</sub> nanoparticles . . . . .	48
4.1.1	Structural and textural properties . . . . .	48
4.1.2	Chemical composition . . . . .	54
4.1.3	Optical absorption properties . . . . .	57
4.1.4	Photocatalytic performance . . . . .	58
4.1.5	Summary of pyroelectric undoped and doped BaTiO <sub>3</sub> systems . . . . .	63
4.2	Size effects on the photocatalytic kinetics of polar BaTiO <sub>3</sub> particles: Thermo-dynamic and LGD phenomenological approaches . . . . .	65
4.2.1	Textural properties . . . . .	65
4.2.2	Microstructural properties (Size effect on tetragonality, <i>c/a</i> ratio and Curie temperature, <i>T<sub>C</sub></i> ) . . . . .	67
4.2.3	Optical absorption properties (size effect on energy bandgap, <i>E<sub>g</sub></i> ) . . . . .	74
4.2.4	Size effect on the reaction kinetics . . . . .	77

4.2.5	Summary of size effects on the photocatalytic activity of polar BaTiO <sub>3</sub> particles . . . . .	82
<b>5</b>	<b>Conclusion and perspectives</b>	<b>85</b>
5.1	Conclusion . . . . .	85
5.2	Perspectives . . . . .	87
<b>Appendix A</b>		<b>91</b>
A.1	Experimental details (Section 4.1) . . . . .	91
A.1.1	Materials . . . . .	91
A.1.2	Microwave-assisted hydrothermal synthesis of doped pyroelectric BaTiO <sub>3</sub> nanoparticles . . . . .	91
A.1.3	Characterization of samples . . . . .	92
A.1.4	Photocatalytic activity measurement . . . . .	93
A.2	Band structure determination using XPS quantification . . . . .	94
<b>Appendix B</b>		<b>95</b>
B.1	Experimental details ( Section 4.2) . . . . .	95
B.1.1	Materials . . . . .	95
B.1.2	Microwave-assisted hydrothermal synthesis of pyroelectric BaTiO <sub>3</sub> particles . . . . .	95
B.1.3	Characterization of samples . . . . .	96
B.1.4	Time evolution of MO photodegradation by <i>in-situ</i> Raman spectroscopy	98
<b>References</b>		<b>103</b>
<b>Résume en Français</b>		<b>125</b>
1.1	Introduction . . . . .	125
1.2	Objectifs de recherche . . . . .	128
2.1	Considération théorique . . . . .	129
2.2	Méthodologie . . . . .	130
2.2.1	Préparation de nanoparticules pyroélectriques de BaTiO <sub>3</sub> . . . . .	130
2.2.2	Caractérisation des échantillons . . . . .	131
2.2.3	Mesure de l'activité photocatalytique . . . . .	132

2.3	Résultat expérimentaux et discussion . . . . .	133
2.3.1	Nanoparticules de BaTiO <sub>3</sub> pyroélectrique . . . . .	133
2.3.2	L'effet de la taille des particules sur l'activité photocatalytique des particules polaires de BaTiO <sub>3</sub> : Thermodynamique et Landau-Ginzburg-Devonshire (LGD) phénoménologique approches . . . . .	138
2.4	Conclusion . . . . .	142

# List of Figures

1.1	Solar spectral irradiance at air mass 1.5 (AM1.5) . . . . .	3
1.2	Energy band alignment of traditional photocatalyst, anatase titanium dioxide ( $a\text{-TiO}_2$ ) and some titanium-based oxide perovskites at $pH = 0$ . Data are extracted from [33, 34]. The conduction band and valence band are shown in green and purple, respectively. . . . .	7
2.1	Mechanism of photocatalytic reaction using semiconductor-based photocatalyst. AS <sub>1/2</sub> denotes negatively and positively adsorbed species (AS) of the pollutant. . . . .	13
2.2	Basic concept used in semiconductor-electrolyte photochemistry. $E_{ion}$ is the ionization energy. . . . .	14
2.3	Illustration of Sabatier principle for the design of a catalyst. . . . .	15
2.4	The band (a) modification through doping; alignment of some metal (b) oxides, and (c) metal chalcogenides. (b) and (c) are adapted from Haque et al. [70]. . . . .	17
2.5	A typical unit cell (right) of $\text{ABO}_3$ perovskite structure. . . . .	21
2.6	The structural phase transitions in $\text{BaTiO}_3$ as temperature is lowered (a) cubic (b) tetragonal (c) orthorhombic, and (d) rhombohedral. . . . .	22
2.7	The photo-excitation process in a typical (a) $p\text{-}n$ junction, (b) centrosymmetric, and (c) non-centrosymmetric material. . . . .	25
2.8	Structural transitions in $\text{BaTiO}_3$ showing the variation of dielectric permittivity, spontaneous polarization and tetragonality upon cooling down. Figure adapted from Aksel and Jones [125]. . . . .	27
2.9	The composite structure model used in explaining tetragonal-to-cubic phase transition in non-centrosymmetric crystal. . . . .	28
2.10	The size dependent reaction rate for different values of $\eta$ according to equation 2.19. Figure is adapted from Murzin [142]. . . . .	33

3.1	The schematic illustration of a (a) standard microwave oven operating at a frequency of 2.45 GHz, and (b) magnetron. . . . .	36
3.2	(a) The major components of X-ray diffractometer (b) Illustration of diffraction of monochromatic X-ray incident on atomic planes of a material. . . . .	38
3.3	A typical Raman system indicating the major components. . . . .	39
3.4	The different scattering processes (a) Rayleigh (b) Stokes, and (c) Anti-Stokes. The broken lines denote the virtual state. . . . .	41
3.5	Distinction between (a) acoustic, and (b) optical phonon modes. . . . .	41
3.6	Emission processes leading to both Auger and photoelectrons in X-ray photo-electron spectroscopy. . . . .	42
3.7	The major components of a typical transmission electron microscopy. . . . .	43
3.8	A schematic showing various components of a UV-Vis-NIR spectrometer. . . . .	45
4.1	The (a) X-ray diffraction patterns of (i) BaTiO <sub>3</sub> , (ii) 4 mol% Cr:BaTiO <sub>3</sub> , (iii) 2 mol% Fe:BaTiO, (iv) 4 mol% Fe 4 mol% Cr:BaTiO <sub>3</sub> , and (v) 8 mol% Fe 4 mol% Cr:BaTiO <sub>3</sub> pyroelectrics, (b) expanded view of (002) and (200) diffraction lines marked by the shaded portion in (a), (c) dopant dependent lattice parameters and unit cell distortion, ( $c/a - 1$ ), and (d) unit cell volume variation of the samples. . . . .	49
4.2	The Raman spectra of (i) BaTiO <sub>3</sub> , (ii) 4 mol% Cr:BaTiO <sub>3</sub> (iii) 2 mol% Fe:BaTiO <sub>3</sub> , (iv) 4 mol% Fe 4 mol% Cr:BaTiO <sub>3</sub> & (v) 8 mol% Fe 4 mol% Cr:BaTiO <sub>3</sub> samples. The “gray” and “green” bars denote the Raman modes for TiO <sub>2</sub> and Cr-O vibrations, respectively. . . . .	51
4.3	TEM images of (i) BaTiO <sub>3</sub> , (ii) 4 mol% Cr:BaTiO <sub>3</sub> (iii) 2 mol% Fe:BaTiO <sub>3</sub> , (iv) 4 mol% Fe 4 mol% Cr:BaTiO <sub>3</sub> & (v) 8 mol% Fe 4 mol% Cr:BaTiO <sub>3</sub> samples. 53	53
4.4	Particle size distribution of (i) BaTiO <sub>3</sub> , (ii) 4 mol% Cr:BaTiO <sub>3</sub> (iii) 2 mol% Fe:BaTiO <sub>3</sub> , (iv) 4 mol% Fe 4 mol% Cr:BaTiO <sub>3</sub> & (v) 8 mol% Fe 4 mol% Cr:BaTiO <sub>3</sub> samples. L and D denote the length and diameter of nanorods as in the case of (ii). . . . .	53
4.5	(a) Energy dispersive X-ray spectroscopy (EDS), and (b) XPS survey spectra of (i) BaTiO <sub>3</sub> , (ii) 4 mol% Cr:BaTiO <sub>3</sub> (iii) 2 mol% Fe:BaTiO <sub>3</sub> , (iv) 4 mol% Fe 4 mol% Cr:BaTiO <sub>3</sub> & (v) 8 mol% Fe 4 mol% Cr:BaTiO <sub>3</sub> samples. Marked rectangles denote the peak intensity associated with Fe for samples containing iron. . . . .	54

4.6	The XPS high resolution scan of Ba 3d <sub>5/2</sub> , Fe 2p, Cr 2p, O 1s, and Ti 2p (from left to right) for (i) BaTiO <sub>3</sub> , (ii) 4 mol% Cr:BaTiO <sub>3</sub> (iii) 2 mol% Fe:BaTiO <sub>3</sub> , (iv) 4 mol% Fe 4 mol% Cr:BaTiO <sub>3</sub> & (v) 8 mol% Fe 4 mol% Cr:BaTiO <sub>3</sub> samples (in rows from bottom to top). Peaks labeled H <sub>2</sub> O, OH <sup>-</sup> and O <sup>2-</sup> denote surface adsorbed water, hydroxyl/defect oxygen, and oxygen bonded to lattice. . . . .	55
4.7	Optical absorption spectra of the as-synthesized undoped and doped photocatalysts. . . . .	57
4.8	The time-dependent (a) photodegradation of MO over as-synthesized pyroelectric samples, (b) kinetics for adsorption (c) kinetics for photodegradation, (d) the plot of photon energy against normalized spectral irradiance integrated over all the wavelengths of the solar spectrum. Bar charts show reaction rate constants obtained for the (e) adsorption, and (f) photochemical catalyzation, respectively. The solid lines depict exponential (a) and linear (b and c) fits to data. (g) The variation of reaction rate constant with catalyst mass in order to determine the catalyst loading for 4 mol% Fe 4 mol% Cr:BaTiO <sub>3</sub> nanoparticle. (h) The schematic band structures of the samples. . . . .	61
4.9	TEM images of (a) 3 μm, (b) 2 μm, (c) 100 nm, (d) 50 nm, (e) 26 nm, (f) 19 nm, and (g) 9 nm barium titanate particles. . . . .	65
4.10	The particle size distribution of (a) 3 μm, (b) 2 μm, (c) 100 nm, (d) 50 nm, (e) 26 nm, (f) 19 nm, and (g) 9 nm barium titanate particles. . . . .	66
4.11	(a) The XRD pattern of the different sizes of barium titanate particles; (b) The expended view of line profile at 45°. The red solid line is the fit to experimental data; The size-dependent (c) lattice parameters, <i>a</i> -axis and <i>c</i> -axis, and (d) tetragonality, <i>c/a</i> ratio. Inset of (d) is the expanded view of <i>c/a</i> ratio in the range, 0 - 150 nm. . . . .	70
4.12	The Raman spectra of the different sizes of BaTiO <sub>3</sub> particles acquired at room temperature. . . . .	71
4.13	(b) The variation of estimated <i>T<sub>C</sub></i> versus particle size. . . . .	74
4.14	(a) - (c) with insets and (d) are the energy bandgap determined via UV-vis-NIR spectroscopy. . . . .	75
4.15	The variation of the energy bandgap with the average particle size. The solid line is the fit using equation 4.3. . . . .	76

4.16 The adsorption (a), and degradation (b) kinetics of the particles. Solid lines are linear fits to data between 0 - 30 min corresponding to the L-H mechanism. (c) The bar chart showing the variation of reaction rate constant with particle size extracted from (a) . . . . .	78
4.17 (a) The variation of first-order reaction constant for degradation of MO with particle sizes. (b) The half degradation time variation with particle size. . . . .	79
4.18 The plot of $k$ as a function of particle size, $x$ . Solid lines are numerical fit according to (a) equation 2.19 and (c) equation 4.5. The expanded view for particle sizes between 0 - 120 nm are shown in (b) and (d), respectively. The unit cells in green and blue depict the tetragonal-to-cubic phase transition due to decrease in particle size. . . . .	81
A.1 The setup for measurement of photocatalytic activity. . . . .	93
B.1 Temperature evolution of Raman spectra for (a) 3 $\mu\text{m}$ , (b) 2 $\mu\text{m}$ , (c) 100 nm, (d) 50 nm, (e) 26 nm, (f) 19 nm, and (g) 9 nm particles. . . . .	98
B.2 The Raman spectrum of methylene orange (MO). . . . .	99
B.3 (a) Time evolution of photodegradation of MO over 50 nm BaTiO <sub>3</sub> powder by <i>in-situ</i> Raman spectroscopy. (b) Lorentzian fit of Raman band of water. . . . .	100
B.4 Proposed photocatalytic degradation pathway of MO over pyroelectric BaTiO <sub>3</sub> nanoparticles. . . . .	101

# List of Tables

2.1	Summary showing similarities and differences between TiO <sub>2</sub> (anatase) and BaTiO <sub>3</sub> (tetragonal). . . . .	23
4.1	The photodegradation rate constant and half-life period for the different sizes of barium titanate. . . . .	80
A.1	The values of electronegativity, and molar ratio of the samples. Literature values of electronegativity of elements were extracted from the work of Pearson [215]. . . . .	94



# List of Symbols & Abbreviations

AOP	- Advanced oxidation process
BPVE	- Bulk photovoltaic effect
UV-Vis-NIR	- Ultraviolet (250 - 400 nm) - Visible (400 - 700 nm) - Near infrared
CB	- Conduction band
VB	- Valence band
$E_g$	- Energy bandgap (eV)
$V_{CB}$	- Conduction band potential (eV)
$V_{VB}$	- Valence band potential (eV)
TM	- Transition metal
$\Delta G$	- Gibbs free energy (J)
NHE	- Normal hydrogen energy
$V^e$	- Potential energy of free electron (eV)
$P$	- Electric polarization ( $\mu\text{C}/\text{cm}^2$ )
$\beta_{ijk}$	- Bulk photovoltaic tensor
$T$	- Temperature (K)
$\hbar\omega$	- Photonic energy (eV), $\hbar$ is reduced Planck's constant
GLSL	- Gradient lattice strain layer
LGD	- Landau-Ginzburg-Devonshire model
$\delta$	- Extrapolation length (m)
$\phi$	- Work function (eV)
$V_M$	- Molar volume ( $\text{m}^3/\text{mol}$ )
L-H	- Langmuir-Hinshelwood model
$R$	- Universal gas constant, $8.314 \text{ JK}^{-1}\text{mol}^{-1}$
$E_{ion}$	- Ionization energy (eV)

- $\sigma$  - Surface tension ( $\text{J/m}^2$ )  
 $\emptyset$  - Quantum yield over a wavelength range  
 $\mu$  - Reduced mass of electron and hole  
 $T_C$  - Curie temperature ( $^\circ\text{C}$ )  
PTFE - Polytetrafluoroethylene  
 $\zeta$  - Excitation asymmetry  
MO - Methylene orange (Azo dye)  
S-Q - Shockley–Queisser limit  
 $\lambda$  - Wavelength (nm)  
 $k$  - Degradation rate constant ( $\text{min}^{-1}$ )  
IEF - Internal electric field ( $\text{Vm}^{-1}$ )  
ToF - Turnover frequency

## **Part 1**

**Main work:**

**Introduction, Literature review & Discussion**



# Chapter 1

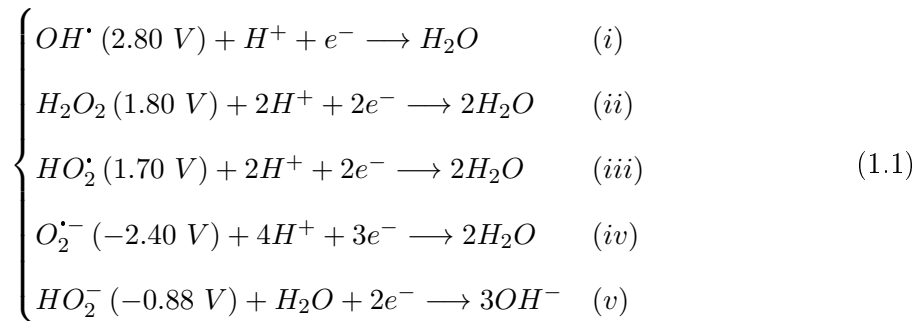
## Introduction, objectives and plan

### 1.1 Introduction

One of the basic needs of man according to United Nations (UN) is water. Unfortunately, the ever-increasing population coupled with industrialization not only pressurized but also tainted the limited water resources available. The degree of pollution can be determined by various anthropogenic and sometimes geogenic activities. The discharge of these effluents containing dyes, pigments, pesticides, pharmaceuticals etc. into waterbodies are considered anthropogenic and makes water unsafe for drinking. This further endangers the lives of aquatic organisms [1]. In other words, water pollution has become a major global challenge that is yet to be addressed. In this regard, treatment technologies exist and include chemical [2], electrochemical [3], membrane filtration, biological and catalysis [4]. Catalysis, which is widely used in large-scale centralized water treatment plants essentially uses a semiconductor material (i.e. catalyst) to accelerate a chemical reaction by “turbocharging” the chemical process in order to break bonds of complex chemical structures [1]. However, the intensive use of energy and chemical plays down on the technology. On the part of chemical (catalyst), reducing the treatment time and cost have always been the key factors to developing novel industrially relevant catalyst. For many industrial catalytic processes, noble metals have been frequently used owing to their high catalytic activity, chemical stability, and even resistance to photocorrosion. Cost seems to be the major factor driving the shift away from the use of noble metals. To have a guide towards a cost-driven catalyst development, let us introduce a benchmark metric. Recently, the price of gold (Au) has notably increased to \$62.36/gram, platinum (Pt) - \$29.14/gram, iridium (Ir) - \$52.89/gram, rhodium (Rh) - \$398.67/gram, palladium (Pd)

- \$75.65/gram etc. (at the time of writing) [5] apparently due to increasing demand for industrial catalysts. For example, in the catalytic process leading to production of cured silicones, platinum-based catalysts are used and up to  $\sim 4$  - 6 metric tons of the catalyst are lost in the process annually [6]. This translates to \$117 million - \$175 million and overall it is a huge cost. Therefore, to make catalysis sustainable, it is important to develop a replacement catalyst. Earth-abundant materials such as the transition metals (TMs) are  $\sim 10^4$  times in abundance compared to noble metals and also exhibit promising distinct reactivity profiles [7]. In other words, transitioning from noble metal-based catalysts to earth-abundant-based catalysts would reduce the cost of chemicals used in catalysis.

One cannot completely rule out that each of the treatment technologies demonstrate potentials in depolluting contaminated water, the disadvantages tend to undermine their deployment and applicability particularly in the remote areas where waterborne diseases are significantly on the rise. In the bid to decentralize conventional water treatment facilities, a more viable, affordable, and sustainable technology is required. Photocatalysis emerges as an option. It is a green technology and its activity relying on the principles of advanced oxidation processes (AOPs) is richly rewarded by the abundant sunlight. After the photoelectrolysis of water to produce hydrogen using single crystalline  $TiO_2$  in 1972 [8], photocatalysis has risen to prominence. Though, its use for hydrogen generation suffered a notable drawback, the exploitation of its oxidative power was demonstrated later by oxidation of industrial pollutant, cyanide ion in 1977 [9]. Basically, reactive species of radicals with different reducing and oxidizing potentials [10] are generated according to equation 1.1:



Inasmuch as cascades of radicals produced particularly the  $OH^\bullet$  are highly oxidative ( $V^0 = 2.80$  V [11]), the semiconductor photocatalyst,  $TiO_2$  however was later observed to be constrained by, but not limited to these factors namely; (i) wide energy bandgap - the intrinsic absorption is in the ultraviolet (UV) region which accounts for only 3 - 5% of the solar spectrum [12, 13] (see

figure 1.1); (ii) high recombination rate - it suffers from low quantum yield as a result of poor charge carrier separation i.e.  $\sim 90\%$  of the photo-generated charge carriers recombine rapidly after electron-hole pair separation leaving nearly 10% for hole/electron-driven chemistry [14].

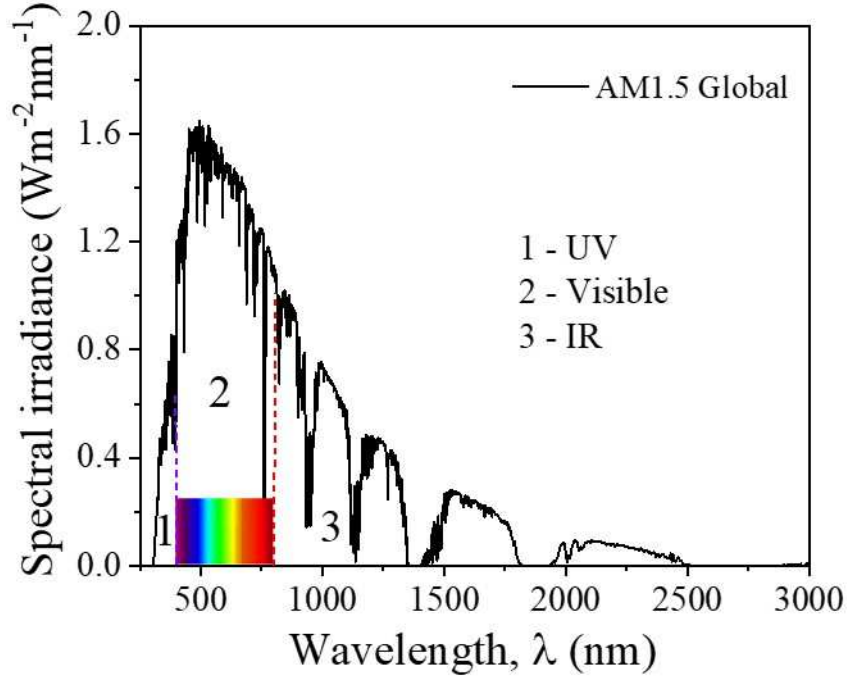


Figure 1.1: Solar spectral irradiance at air mass 1.5 (AM1.5).

Non-metal/metal doping and heterojunctions have been among the strategies to enhance the light absorption and catalytic properties of  $\text{TiO}_2$ . Metal doping, especially with plasmonic materials such as silver (Ag), gold (Au), copper (Cu) etc. have been shown to be effective as excited electrons in the conduction can easily be attracted by the metal particles due to the difference in the work function between the metal and  $\text{TiO}_2$ . Apart from the plasmonic metals acting as electron scavenger to increase the electron-hole pair separation upon photo-generation, they exhibit surface plasmon resonance (SPR) effect which in turn enhances its catalytic efficiency. In SPR effect, there is a coupling of electromagnetic field of the incident light and oscillating conduction electrons culminating to strong-field enhancement of the local electromagnetic fields near the surface of plasmonic material [15]. In particular, Ag and Au exhibit strong SPR absorption peak in the visible region making them good candidates for visible-light active photocatalyst. For example, the photocatalytic evaluation carried out using plasmonic Au: $\text{TiO}_2$  [16] and Ag: $\text{TiO}_2$  [17] photocatalysts showed significant photocatalytic activity, higher than the pristine  $\text{TiO}_2$ . This shows that the noble metals loaded on

TiO<sub>2</sub> provide synergistic activity through efficient electron transfer process. However, the degradation rate constants of Au:TiO<sub>2</sub> (0.0241 min<sup>-1</sup>) and Ag:TiO<sub>2</sub> (0.0041 min<sup>-1</sup>) for the first-order reaction appears to be lower when compared to a non-centrosymmetric material such as BaTiO<sub>3</sub> (0.032±0.003 min<sup>-1</sup>) [18]. This may be attributed to additional charge carrier separation through bulk photovoltaic effect, which will be discussed in details in Chapter 2.

Nanotechnologically, the recent advances in photocatalysis are much more centered on materials design. The activities of some of these materials appear to be rivaled as major issues like the material properties and kinetics were not put into consideration [1, 19]. To address these challenges, a material with enhanced photoabsorption cross-section, adsorption capacity, and localized surface charges will be considered promising. This should form a basic design parameter in the fabrication of new functional materials. Barium titanate, BaTiO<sub>3</sub> with perovskite structure ( $A^{2+}B^{4+}O_3^{2-}$ ) is an interesting material in this regard and exhibits the shift current mechanism otherwise known as the bulk photovoltaic effect (BPVE). The long-range surface electric field contributes to charge carrier separation particularly for the non-centrosymmetric configuration of the material [20]. Similar to the bandgap of the anatase form of TiO<sub>2</sub>, it has an absorption edge at ∼390 nm [21] and can be considered as an alternating stacked layers of BaO and TiO<sub>2</sub> along (001) with the latter exhibiting the catalytic properties. Technically, the extension of photosensitivity of the ecofriendly barium titanate by doping is not novel but the exploitation of the localized surface charges culminating from BPVE holds the promise to improving the charge transport properties of the material, which is entirely beneficial for photocatalytic applications.

## 1.2 Motives

Quantum efficiency is an important factor for both endergonic and exergonic reactions. Since the ratio of “useful” charge carriers to the number of photons incident on a photocatalyst defines the term, quantum efficiency, it implies that it is zero for photons with energy below the photocatalyst’s bandgap. The quantum efficiency is a product quantity expressed as  $\eta_T = \eta_1 \times \eta_2 \times \eta_3 \dots \eta_n$ , where  $\eta_1$  to  $\eta_n$  represent different processes such as photon absorption, exciton separation, transport etc. up to the efficiency of the  $n$ th process considered during photocatalysis. Using it as a good descriptor, the individual efficiencies can further be

simplified as

$$\begin{cases} \eta_T = \frac{\eta_{photochemistry}}{\eta_{photon\ absorption}} & (i) \\ \frac{\eta_{photochemistry}}{\eta_{photon\ absorption}} = \frac{\eta_{photochemistry}}{\eta_{e^-/h^+ transport}} \times \frac{\eta_{e^-/h^+ transport}}{\eta_{e^-/h^+}} \times \frac{\eta_{e^-/h^+}}{\eta_{photon\ absorption}} \times \dots & (ii) \end{cases} \quad (1.2)$$

While the numerator of equation 1.2(i) is normally obtained from photocatalytic experiments, the denominator evaluates the rate of photon absorption for the photocatalyst. Since the efficiency of  $n$ th process depends on the efficiency of  $(n - 1)$ th process and so on, this means that any of the processes with low efficiency introduces a multiplicative effect, thereby reducing the total quantum efficiency. Therefore, an efficient catalyst takes the material design, process (i.e. material properties) and the surface reaction into consideration. It is well known that in catalysis involving light-activated semiconductor materials, there are some fundamental steps when illuminated with a light whose energy is greater than the bandgap ( $E_g$ ) of the material.

- ◊ The light absorption leading to photogeneration of electron-hole pairs in which the electrons are excited into the conduction band (CB) leaving the highly oxidizing holes in the valence band (VB). Hence, the number of photogenerated charge carriers depends on the absorption cross-section of the material, which is entirely determined by the nature of bandgap and may be charge transfer center of the ionizable impurity atom, i.e. defect absorption. For example, as most  $3d$  elements show multivalent electronic states, the concept of modulating the electronic properties by creating point defects in a controlled and confined region is possible. In the oxide perovskite structure with aliovalent substitution at B-site, usually an oxygen vacancy,  $V_O^{..}$  is initiated through charge compensation mechanism resulting to transfer of electrons to the  $3d$  orbitals of the B-site ion along the  $B - V_O^{..} - B'$  axis [22]. In principle, the  $B'$  centers are constantly photoionized when illuminated. The overall process is reversible and requires an intervalence switching between different electronic states of the charge transfer centers following the photoreaction,  $B'^{(x+/y+)} \leftrightarrow B^{(z+/y+)}$  [23–25]. In any case, there is an Coulombic interaction between photogenerated electrons and holes resulting to excitons.
- ◊ The charge carrier separation (i.e. dissociation of excitons). The obtention of free charge carriers is indirectly governed by  $q^2/4\pi\epsilon_0\epsilon_r r^2$ , where  $q$  is the charge i.e. either hole or electron,  $r$  is the distance apart, and  $\epsilon_r$  is relative permittivity. This means that if the Coulombic force binding the hole and electron is low due to large value of  $\epsilon_r$ , then charge

carriers can be separated with ease [26].

- ◊ The diffusion of free charge carriers. The mobility of these charges should be as high as possible to enable them diffuse to the target surface sites where reaction takes place. For this purpose, the reduced effective mass (electron and hole) should be less than  $0.5m_0$  [26]. Only then can the holes effectively react with  $\text{H}_2\text{O}$  to produce hydroxyl  $\text{OH}^\cdot$  radical. This in turn decomposes any organic molecules adsorbed at the surface of the semiconductor material, ideally to  $\text{CO}_2$  and  $\text{H}_2\text{O}$ . However, the scenario is only possible if the valence band potential where the holes occupy is more positive in comparison to the oxidation potential of the target redox couple. In addition, the photogenerated electrons needs to be scavenged by adsorbed oxygen on the surface of the semiconductor to avert unnecessary recombination. This demonstrates the importance of the conduction band potential aligning with the reduction potential of the target redox couple.
- ◊ The recombination of these photogenerated charge carriers limits the overall quantum efficiency of the process. The quantum yield that describes the number of separated charge carriers participating in a catalytic reaction depends on the recombination rate. The recombination of charge carriers requires a few picoseconds and occurs on a much faster time scale than the charge transport and charge-consuming catalysis [27]. The first three shows how crucial material design and energy band alignment are in selecting a material. For clarity, figure 1.2 shows the energy band diagram of the traditional photocatalyst (anatase  $\text{TiO}_2$ ) and some selected oxide perovskites from the titanate family.

Inorganic oxide perovskites are mostly wide bandgap semiconductors. The choice of A- and B-site cations offers a versatile approach towards tailoring the properties for a desired application. From the perspective of catalysis for in/outdoor purposes, a choice perovskite material will have to be environmentally benign and affordable. The TM-based perovskites, in particular the titanate prototype can easily be scaled to commercial quantity due to the availability of titanium, which constitutes roughly 0.63% of the Earth's crust [28]. Although, most A-site-transition-metal oxide perovskites such as  $\text{FeTiO}_3$  [29],  $\text{CoTiO}_3$  [30],  $\text{NiTiO}_3$  [31] etc. show visible light absorption, they are more susceptibility to photocorrosion as they are thermodynamically unstable for photocatalytic applications [32].

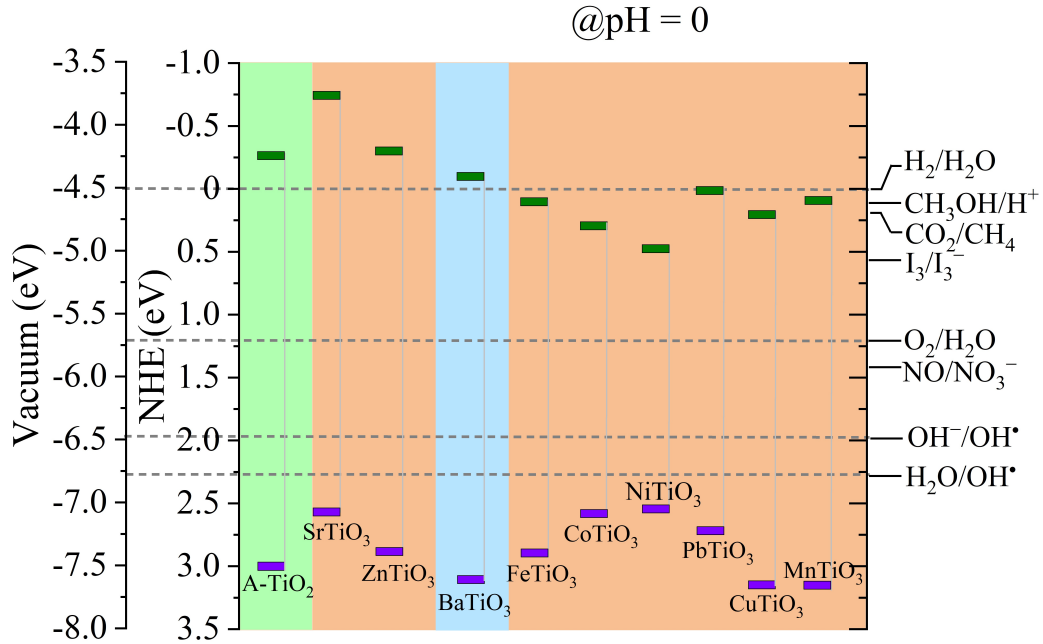


Figure 1.2: Energy band alignment of traditional photocatalyst, anatase titanium dioxide (*a*-TiO<sub>2</sub>) and some titanium-based oxide perovskites at *pH* = 0. Data are extracted from [33, 34]. The conduction band and valence band are shown in green and purple, respectively.

SrTiO<sub>3</sub> on the other hand, crystallizes in non-polar cubic phase at room temperature [35], which lacks the innate BPVE helpful for charge carrier separation. BaTiO<sub>3</sub> therefore emerges as a promising candidate for this purpose. Just as most oxide perovskites, it exhibits high stability and chemical resistance in both aqueous and non-aqueous solution [36]. At room temperature, BaTiO<sub>3</sub> is pyroelectric and possesses crystal polarity that generates microscopic depolarization fields across respective domains due to broken-inversion symmetry of the crystal. The potential barrier towards its application in photocatalysis remains poor light absorption and low carrier mobility. It has an absorption edge in the UV region, which is only 3 - 5% of the solar spectrum. To address the issue and improve its photocatalytic activity, we doped with TMs whose charge transfer centers are associated to strong absorption bands in the visible region.

### 1.3 Research objectives

Fast recombination of charge carriers is one of the major bottlenecks militating against the practical use of AOPs for sustainable decontamination of wastewater. The contribution of

surface generated electric fields has been found useful but rarely forms an important parameter during material design. The approach in designing visible-light sensitive pyroelectrics (i.e non-centrosymmetric materials coupled with sufficient light absorption) could be a better way of improving the photocatalytic performance of a wide range of inorganic perovskite photocatalysts. To this effect, the use of defect chemistry based on earth-abundant TMs are explored. Hence, our overall goals of the thesis are: (1) to use gap-state engineering to fabricate visible-light-active pyroelectric BaTiO<sub>3</sub>, and (2) to investigate the effect of particle size on the photocatalytic kinetics and mass transport of pyroelectric BaTiO<sub>3</sub>. To pursue this, the following forms the specific objectives:

- ◊ to deploy a scalable microwave-assisted hydrothermal technique for the synthesis of the visible-light-active pyroelectric barium titanate nanoparticles.
- ◊ to understand the effect of chromium in Cr-doped barium titanate nanoparticles.
- ◊ to replace chromium with non-toxic iron (Fe) in the Cr-doped barium titanate nanoparticles and investigate its potentials for environmental remediation.
- ◊ to understand the interplay between particle size and the bulk photovoltaic effect responsible for polarization-induced charge carrier separation in the tetragonal BaTiO<sub>3</sub>.

## **1.4 Thesis plan**

The dissertation is organized based on the thesis by articles structure otherwise referred to as “thèse par articles”. It basically consists of five (5) chapters which are as follows:

- ◊ Chapter 1 is the introduction to the dissertation.
- ◊ Chapter 2 gives a background review on the mechanism of redox photocatalytic process followed by brief assessment of photocatalytic semiconductors commonly used in redox processes. (Dis)advantages of titanium dioxide, TiO<sub>2</sub> are equally reviewed in relation to tetragonal barium titanate, *t*-BaTiO<sub>3</sub>, which offers the benefit of polarization-assisted charge carrier separation. The chapter also elaborates on two approaches to study particle size effect in catalytic materials which were deployed to analyze experimental data in Chapter 4.

- ◊ Chapter 3 highlights the principles of microwave oven, X-ray diffraction technique, X-ray photoelectron spectroscopy, Raman spectroscopy and UV-Vis-NIR absorption spectroscopy used in carrying out this research.
- ◊ The detailed experimental results are presented in Chapter 4. For clarity, the chapter is partitioned into two sections i.e. Section 4.1 and 4.2. In section 4.1, the benefit of light absorbing Cr-doped BaTiO<sub>3</sub> nanoparticles over the undoped system is discussed. Further benefit is elaborated by co-doping BaTiO<sub>3</sub> nanoparticles with chromium and iron. In addition, the far reaching consequence of the co-doping effect is highlighted when deployed for photocatalytic degradation of azoic methylene orange. While the use of chromium is potentially unsafe especially in hexavalent state, we replaced chromium with iron and discussed its extensive advantages in terms of enhanced light absorption and non-toxicity. Section 4.2 deals with the effect of particle size on the photocatalytic kinetics of pyroelectric barium titanate particles. The observations of a particle size-dependent catalytic activity beyond the expected change of surface is quantitatively discussed in the framework of two models: the first is describing the loss of the bulk photovoltaic effect upon a size-driven phase transition into a centrosymmetric phase for ultra-small particles while the second model discusses modified material transport kinetics at the nanoscale.
- ◊ Chapter 5 gives a brief summary on the photocatalytic performances of the doped photocatalysts, particle size effect on the photocatalytic kinetics and mass transport at the solid catalyst-liquid interface. The chapter further highlights recommendations which may form basis for future studies.

## 1.5 Scientific publications

Overall, the Ph.D. project so far generated a total number of four (4) journal publications with one still under preparation; three of which are summarized in Section 4.1 and the other in Section 4.2. Furthermore, two (2) publications culminating from a collaborative projects are included here albeit unrelated to the topic. While the first three highlight the comparative advantage of co- over mono-doping of BaTiO<sub>3</sub>, the last paper examines the size effect on the kinetics of photocatalytic activity of ultrafine particles of nanoscale BaTiO<sub>3</sub>.

**List of publications:**

- ◊ I. C. Amaechi, A. Hadj Youssef, D. Rawach, J. P. Claverie, S. Sun, and A. Ruediger, “Ferroelectric Fe–Cr codoped BaTiO<sub>3</sub> nanoparticles for the photocatalytic oxidation of azo dyes”, ACS Applied Nano Materials, 2 (2019) 2890–2901.
- ◊ I. C. Amaechi, G. Kolhatkar, A. Hadj Youssef, D. Rawach, S. Sun, and A. Ruediger, “B-site modified photoferroic Cr<sup>3+</sup>-doped barium titanate nanoparticles: Microwave-assisted hydrothermal synthesis, photocatalytic and electrochemical properties”, RSC Advances, 9 (2019) 20806–20817.
- ◊ I. C. Amaechi, A. Hadj Youssef, G. Kolhatkar, D. Rawach, C. Gomez-Yáñez, J. P. Claverie, S. Sun, and A. Ruediger, “Ultrafast microwave-assisted hydrothermal synthesis and photocatalytic behaviour of ferroelectric Fe<sup>3+</sup>-doped BaTiO<sub>3</sub> nanoparticles under simulated sunlight”, Catalysis Today, 360 (2021) 90–98.
- ◊ I. C. Amaechi, R. Katoch, G. Kolhatkar, S. Sun, and A. Ruediger, “Particle size effect on the photocatalytic kinetics of barium titanate powders”, Catalysis Science & Technology, 10 (2020) 6274–6284.

**Collaborative projects:**

- ◊ A. Hadj Youssef, F. Ambriz-Vargas, I. C. Amaechi, A. Sarkissian, A. Merlen, R. Thomas, and A. Ruediger, “Impact of negative oxygen ions on the deposition processes of RF-magnetron sputtered SrTiO<sub>3</sub> thin films”, Thin Solid Films, 661 (2018) 23–31.
- ◊ A. Hadj Youssef, G. Kolhatkar, I. C. Amaechi, R. Katoch, Y. Gonzalez, A. Merlen, and A. Ruediger, “Giant step bunching on unintentionally Mg-doped thin films grown epitaxially on vicinal MgO (100) surfaces”, Submitted (2020).

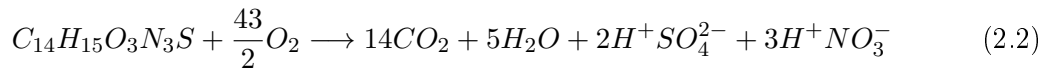
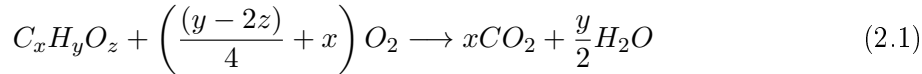
# Chapter 2

## Literature review

### 2.1 General principle/mechanism of redox photocatalytic process

The use of semiconductor-based heterogeneous photocatalysis for environmental remediation dates back to the report on catalytic oxidation of carbon monoxide using ZnO in 1964 [37]. The resurgence, however took another dimension in 1972 following the photoelectrolysis of water using single crystalline TiO<sub>2</sub> [8]. Despite the transition which purportedly aroused the interest in the search for a visible-light-active material that will serve as a replacement for TiO<sub>2</sub>, it does not negate the fact that heterogeneous photocatalysis is technologically sustainable and promising since the by-products of catalyzation are generally and chemically inoffensive and pose no threat to humans [38, 39]. The heterogeneous photocatalysis is comparatively advantageous and unmatched in terms of the following: (i) cost-effectiveness, (ii) absence of sludge, (iii) complete degradation, and (iv) thermodynamics of reaction are considerably mild [40]. These extending advantages spring from the physicochemical (i.e. grain size, crystal structure etc.), intrinsic (pyroelectricity, band structure etc.) properties of the material [1, 41] and the use of abundant solar energy. In principle, the performance of a photocatalytic process is based on a combination of functionalities like harvesting of energy from sunlight, charge carrier generation and separation, and surface area/available active sites among others [42]. Generally, the mechanistic principle of heterogeneous photocatalysis rely on the advanced oxidation processes (AOPs) and can be treated in the framework of photophysics and photochemistry. Technically, the AOP has ultimately shown numerous benefits in areas such as

hydrogen gas generation, oxygen evolution, and decontamination of organic pollutants (e.g. pesticides, herbicides, insecticides, fungicides, dyes etc.) non-selectively [43–46]. The AOP constitutes of highly reactive cascades of radicals (superoxide  $O_2^{\cdot-}$ , hydroxyl  $OH^{\cdot}$ , singlet oxygen  $O_2^1$ , hydroperoxyl  $HO_2^{\cdot}$ , alkoxy RO $^{\cdot}$ , hypochlorous acid HOCl etc. [47]) generated upon illumination with light of substantial energy and potentially capable of degrading harmful compounds found in polluted water. Water and molecular adsorbed oxygen are essential to moderate the degradation of organic pollutant of the type  $C_xH_yO_z$  from the initial chemical structure to intermediates and finally to non-toxic composition of carbon dioxide and water as shown in equation 2.1 [48]. Complex organic structures with nitrogen and sulphur such as found in azo dyes (e.g. methylene orange) are degraded to sulphate and nitrate in addition to products of equation 2.1 [48, 49] (see equation 2.2).



In principle, the photonic activation of semiconductor photocatalyst results to generation of excitons in the bulk of the material. The generated excitons ( $e^- - h^+$ ) dissociate (i.e. charge separation) into free charge carriers accessible either in the conduction or valence band as electrons or holes, respectively. A possible competing process is the non-radiative recombination of these charge carriers which occurs on a time scale of a few nanosecond and produces heat as a consequence [27]. This arises normally due to the Coulombic interaction between electrons and holes [50]. However, the charge transport can be relatively fast depending on the diffusion length such that the migration to the surface triggers a redox reaction [28, 51]. For clarity, the schematic illustration of this reduction and oxidation (redox) processes is given in figure 2.1 while the global redox reaction can be written as:



where  $AS_{1/2}$  denotes the adsorbed species which get reduced ( $Red_1$ ) or oxidized ( $Ox_2$ ), respectively. Equation 2.3 shows that the thermodynamic quantity, Gibbs free energy ( $\Delta G$ ) is non-zero for a photochemical reaction. It suffices therefore to state that the change in Gibbs free energy may be negative, in which case the global reaction is considered photocatalytic

and proceeds downhill, otherwise photosynthetic and uphill in the case of positive Gibbs free energy; and this could be a preliminary confirmation for any redox process [52]. For example,  $\Delta G$  is positive ( $+237 \text{ kJ mol}^{-1}$ ) for a photosynthetic production of hydrogen from water splitting [53].

For a liquid phase interaction with a photocatalyst, often occurring at the semiconductor-electrolyte interface, the kinetics follow similar pattern except that the photochemistry is initiated by charge disequilibrium between the Fermi energy of the solid and electrochemical redox potential of the electrolyte. As depicted in figure 2.2, equation 2.4 is normally employed in estimating the potential energy of the conduction band edge once the energy bandgap of the material is determined through optical spectroscopy [54]:

$$\begin{cases} V_{CB} = \chi - V^e - 0.5E_g & (i) \\ V_{VB} = E_g - V_{CB} & (ii) \end{cases} \quad (2.4)$$

where  $V_{VB}$  and  $V_{CB}$  are valence and conduction band potential  $\chi$  is the electronegativity,  $V^e$  is the potential energy of free electron (4.50 eV [55]) on the normal hydrogen energy (NHE) scale, and  $E_g$  is the energy bandgap of the material. Therefore, effects like termination of the bonding network at the surface, adsorption of ions, and charge transfer between the semiconductor material and electrolytic solution could lead to charge redistribution and equilibration which creates a space charge region with internal electric field that contributes in the charge separation.

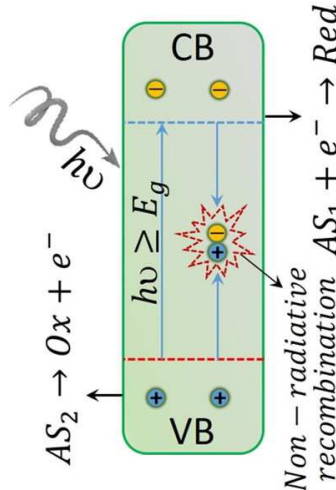


Figure 2.1: Mechanism of photocatalytic reaction using semiconductor-based photocatalyst.  $AS_{1/2}$  denotes negatively and positively adsorbed species (AS) of the pollutant.

Hence, adsorbed species will get oxidized or reduced depending on whether they possess redox potential more negative or positive, respectively than the  $V_{FB}$  of the valence band or conduction band [56, 57]. It suffices that the degradation kinetics of the reaction to be triggered by separated charge carriers is subject to band potentials possessed by the catalytic material. In any case, the holes interact with the pollutant-dissolved water to form a thermodynamically and highly stable oxidizing  $\text{OH}^\cdot$  radical with an oxidation potential and bimolecular reaction rate constants of 2.80 V and  $10^8\text{--}10^{11}\text{M}^{-1}\text{s}^{-1}$ , respectively [58]. Apart from fluorine, the hydroxyl radical provides a spectacular non-selective reaction with organic compounds in contact. It is important to know that the degradation process is not only through the indirect generation of the aforesaid radical but also electrophilic oxygen culminating to superoxide ( $\text{O}_2^{\cdot-}$ ) anion radical and possibly hydrogen peroxide from counter-reaction of  $\text{OH}^\cdot$  radicals. However, reports have shown that the contribution of superoxide in photo-oxidation of organic pollutant is rather less pronounced compared to hydroxyl radicals and holes [59]. Nevertheless, the mechanistic pathway of degradation remains similar and is independent of the energy input whether UV or visible-light.

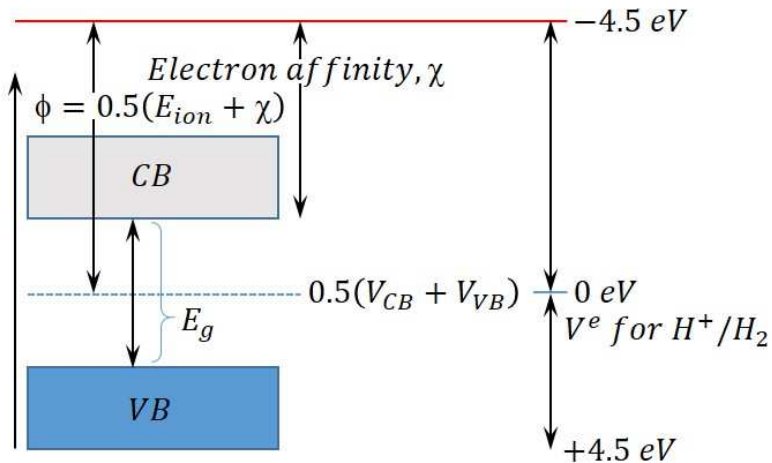


Figure 2.2: Basic concept used in semiconductor-electrolyte photochemistry.  $E_{ion}$  is the ionization energy.

## 2.2 Photocatalytic semiconductors

Catalysis being a surface phenomenon, understanding the functionality of a catalytic surface is the key to optimization. This conceptual framework is proposed by Sabatier principle that a good catalyst should bind atoms and molecules with an intermediate bond strength:

not too weak so that reaction can be initiated, and not too strong so that products can sufficiently desorb (see figure 2.3) [60]. Although, the principle lacked a quantitative approach in predicting molecular compositions for optimum catalytic throughput, it is seemingly successful in providing a qualitative understanding of catalytic materials. While the predictive power deep-rooted in computational chemistry is beyond the scope of this thesis, a chequered transition of myriad of catalytic semiconductor materials appears to validate the fact that the principle could be trivial in material design consideration [61, 62].

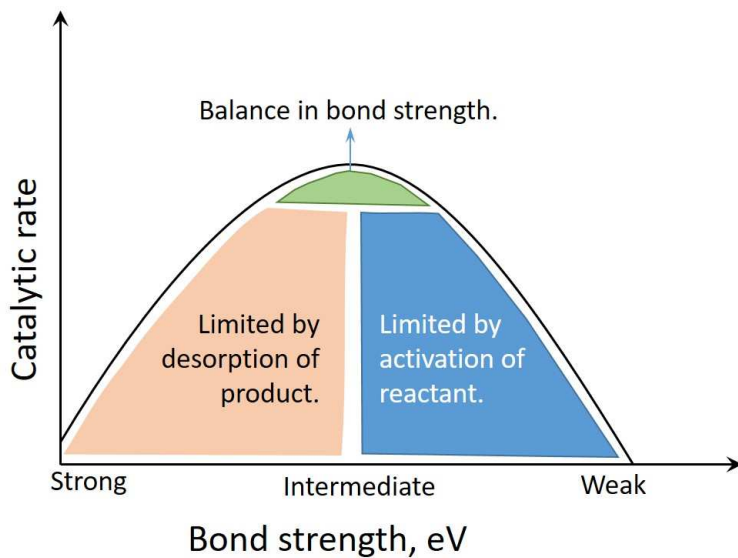


Figure 2.3: Illustration of Sabatier principle for the design of a catalyst.

Generally, semiconductors (and to some extent, insulators) are widely used in catalysis. The lack of continuum of inter-electronic band states in solids constitutes the category of materials referred to as semiconductors (or insulators when the  $E_g > 3$  eV). The bandgap,  $E_g$  can also be distinguished by direct or indirect depending on the band transition. The conduction band minimum (CBM) and valence band maximum (VBM) are defined by a certain crystal momentum i.e.  $k$ -vector in the Brillouin zone. When the bands (i.e. CBM and VBM) lie in the same  $k$ -vector, then the band transition is direct otherwise it is indirect. This has an implication in catalysis in terms of lifetime of excited charge carriers prior to recombination. For example, the direct band transition requires an absorption or emission of photon whereas the indirect band transition involves an absorption or emission of phonon. The latter process makes recombination slower and thus increases the lifetime of charge carriers. These class of materials with indirect band transition are thus more useful in photocatalysis as the energy gap

provides sufficiently long lifetime for charge carriers to migrate to the surface of the material where redox reaction is triggered, a situation which is almost unrealistic in metals due to coexistence of both bands. Inasmuch as the presence of this gap may yet be an asset, there is a tendency of the material's activation energy being restricted to UV portion of solar spectrum thereby limiting the application of such material. Based on this, photocatalytic materials are discussed based on four (4) different classes namely:

◇ Metal oxides

Following the Fujishima and Honda's historic Nature report on water splitting in 1972 [8], there was a shift of attention in search for visible-light materials to replace TiO<sub>2</sub> since its use in hydrogen production technology suffered from both poor light absorption and low quantum efficiency. In this regard, both co-/mono-doping of TiO<sub>2</sub> and transition metal oxide (TMO) photocatalysts have been extensively explored. Studies reveal that oxides of various metals such as V, Cr, Mn, Fe, W, Ta, Zn etc. have been extensively studied [28, 63, 64], with a few of them e.g. ZnO having tendency of photocorroding and being susceptible to dissolution depending on pH medium of the reaction [65]. Nevertheless, a Z-scheme (employing the concept of two photocatalytic semiconductors mediated with/out a shuttle redox mediator) [66, 67], dye-sensitization [66, 68] and perhaps non-/metal doping remain the top materials-design strategies developed to enhance the photocatalytic properties of these oxide materials. Metal oxides are generally known to be stable and have valence band (VB) electrons from the highest occupied molecular O 2p orbitals and conduction band (CB) electrons from the lowest unoccupied metal M<sup>n+</sup> orbitals, where n is the number of charge. The O 2p energy level is to some extent deep; and in terms of band potential, it lies at a more positive band potential which defines its stability as against doped systems which their apparent VB is less positive [69] (see figure 2.4(a) for illustration). In particular, co-/mono-doping provides structural band modifications through localized interstate bands that appears to shift the chemical potentials of CB and VB, though this is at the expense of fast recombination of charge carriers [70]. In figure 2.4(b), we show the band structure of typical metal oxides that has been used for photocatalytic applications.

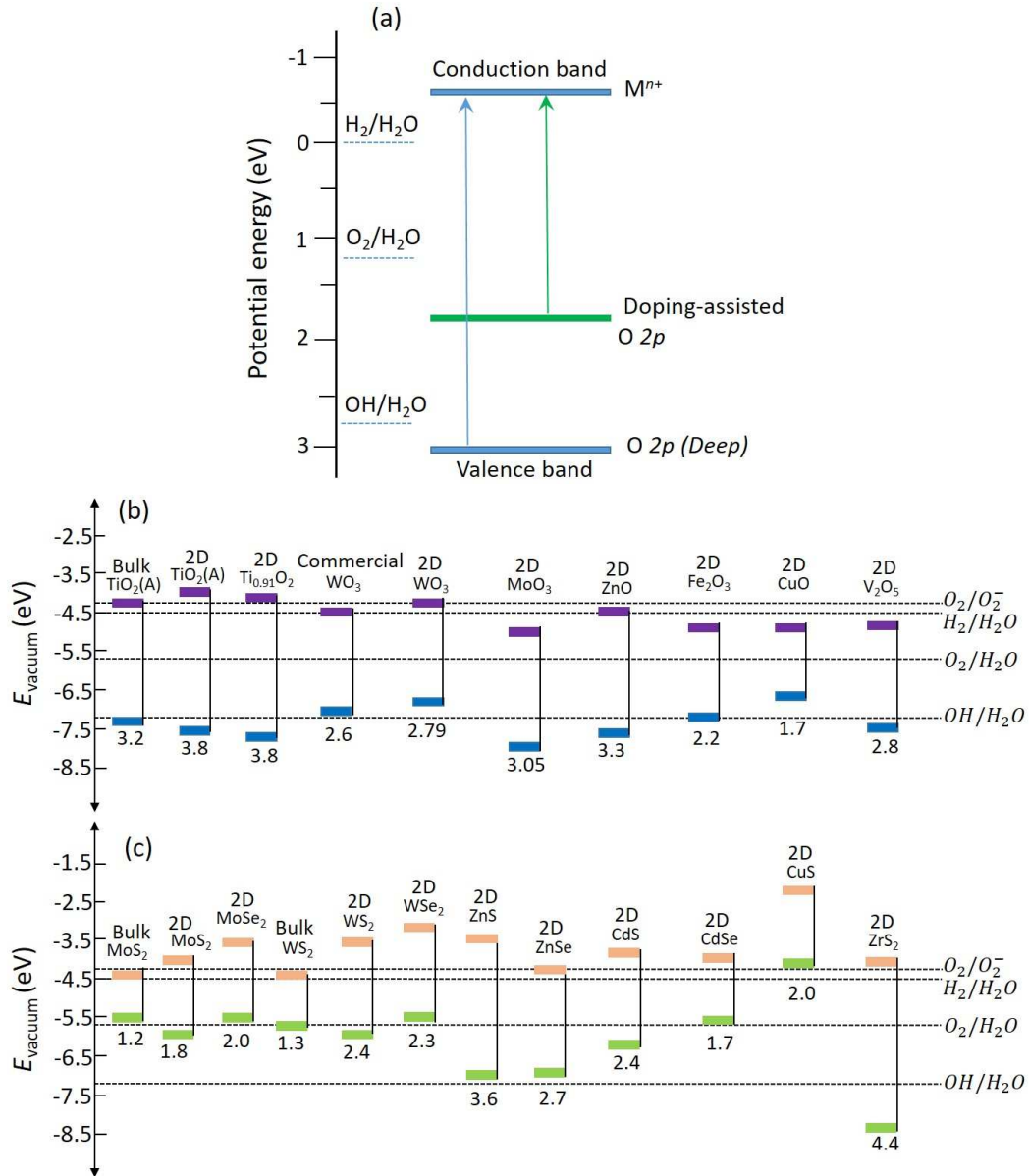


Figure 2.4: The band (a) modification through doping; alignment of some metal (b) oxides, and (c) metal chalcogenides. (b) and (c) are adapted from Haque et al. [70].

#### ◇ Metal sulfides (Chalcogenides)

Chalcogens comprise of elements from the periodic table mainly sulphur (S), selenium (Se) and tellurium (Te). Their reaction with some highly electropositive metals form compounds referred to as metal chalcogenides. These class of materials are important and find technological application in photocatalysis. There has been a resurgence of interest in chalcogenides particularly cadmium ( $\text{CdS}$ ,  $E_g \approx 2.4$  eV) and zinc sulfide ( $\text{ZnS}$ ,  $E_g \approx 3.6$  eV) not only for wastewater degradation but also water splitting, reduction of

carbon dioxide ( $\text{CO}_2$ ), aldehydes, and reductive dehalogenation of benzene derivatives [70, 71]. While a number of these metal chalcogenides have narrow bandgaps which their optoelectronic properties favour photocatalytic applications, the S  $3p$  state corresponding to the valence band however is unstable and again susceptible to photocorrosion [63, 70]. These characteristics alongside wide energy bandgap (for some chalcogenides like ZnS) are undesirable and restrain their application in photocatalysis. Figure 2.4(c) shows the band structure of some commonly used metal chalcogenides.

#### ◊ Metal nitrides

The search for efficient and environmentally benign materials with high photoactivity and stability led to the emergence of metal nitrides. For example, the band potentials of gallium nitride (GaN) can be straddled easily and have been applied for sensing [72], water splitting [73] and wastewater degradation [74]. In addition, some other metal nitrides [75–79] have been developed thereafter in the bid to enhance the photocatalytic activity. Recently, organic ( $\text{C}_3\text{N}_4$ ) photocatalyst, a member of the nitride family has also emerged competitively given that it exhibits the following characteristics: (i) intrinsic visible light response, (ii) high nitrogen content, (iii) high thermal and chemical stability, (iv) tunable texture and structure, and (v) starting materials are abundant and inexpensive [80, 81]. Notably, the fascinating structural tunability of this material helped to construct a polymeric covalently-bonded nitride ( $\text{g-C}_3\text{N}_4$ ) with graphite structure. The graphite-like nature which is isostructural to poly(heptazine imide) presumably originates from a thermal treatment of carbon- and nitrogen-containing monomers and oligomers [81]. Despite the impressive graphite structure, the catalytic activity however was again impeded by some of the following factors viz: (i) solvent accessible surface area, (ii) low electric conductivity, (iii) high exciton binding energy, and (iv) rapid rate of charge-carrier recombination [82]. This led to fabrication of heterostructures in order to address the inherent deficiencies [80, 83–85].

#### ◊ Qua/ternary materials

Multinary system nanostructures are remarkably important for energy and environmental remediation. These systems are synthesized in form of alloys, oxides, oxychalcogenides, and oxynitrides; and have also been investigated extensively for energy and environmental application due to their well-defined band structures and multifunctional

properties. For the qua/ternary oxide systems, they comprise of majorly metallates such as titanates, niobates, ferrites, tungstates etc. The metallates are known to be chemically stable and often crystallize in either  $\text{ABO}_3$ (simple) or  $\text{A}_2\text{B}'\text{BO}_6$  (double-layered) perovskite structures [86], where the latter is derived from the parent structural (simple  $\text{ABO}_3$ ) model with  $\text{BO}_6$  and  $\text{B}'\text{O}_6$  octahedrally coordinated in the lattice. By combining precursors of interest, solid solutions through heterovalent substitution can also provide a combinatorial diversity of this material of the Aurivillius type [87, 88].

### 2.3 A brief overview of titanium dioxide, $\text{TiO}_2$ : Merits and demerits

The photocatalytic oxidation of titanium dioxide,  $\text{TiO}_2$  has long been demonstrated. The catalytic activities resulting from the photoinduced process of  $\text{TiO}_2$  are mainly reported for the anatase (tetragonal, I41/amd) and rutile (tetragonal, P42/mnm) phases [89, 90]. On the other hand, the use of brookite (orthorhombic, Pbca) phase for photocatalytic applications are scarcely reported for reason of instability [91]. The anatase and rutile structural phases are structurally distinguished based on the distortion and arrangement of  $\text{TiO}_6$  octahedra in the unit cell. For the anatase, it consists of  $\text{TiO}_6$  octahedrally coordinated by the vertices while the rutile phase shows a coordination through the edges of the  $\text{TiO}_6$  octahedra. The thermodynamic study of phase stability has indicated that the rutile is most stable under ambient conditions in comparison to the anatase phase [92]. However, in terms of particle size, the anatase is most stable for particle sizes  $< 11$  nm whereas the stability for the rutile occurs for particle sizes  $> 35$  nm [28, 93]. With the presence of oxygen vacancy ( $V_O^{\cdot\cdot}$ ) formed through  $O_O^{\times} \xrightarrow{\text{TiO}_2} V_O^{\cdot\cdot} + 2e^- + \frac{1}{2}O_2$ ,  $\text{TiO}_2$  is generally known to exhibit  $n$ -type semiconductivity with the energy bandgap of the anatase phase  $\sim 0.2$  eV larger than that of the rutile (3.0 eV) [28, 94]. The band structures calculated by the first-principle density functional theory (DFT) show that the anatase and rutile undergo an indirect and direct band transitions, respectively [95]. In any case, this translates to a cut-off wavelength of  $\sim 390$  nm in the UV region, which accounts for only 3 - 5% of the solar spectrum and responsible for its poor light absorption. The behaviour raises concern over the photonic efficiency. In terms of photocatalytic activity of the two phases, the anatase performs better than the rutile while the common commercially available mixture, Degussa P25, shows an increased photoactivity owing to the synergistic

effect of both. While the explanation for the difference in their photocatalytic activity is yet to gain wide acceptance, it is generally believed the reason for anatase being better than rutile could be due to: (i) indirect band transition in anatase - this offers the advantage of long lifetime of electron-hole pair as recombination is only possible with the assistance of phonon momentum when  $k \neq 0$  for the CBM and VBM; (ii) the transport of electron-hole pair from the bulk to the surface - the mobility of charges to the surface is faster in anatase due to lighter effective mass of charges roughly  $\sim 1:8$  compared to rutile; and (iii) the  $\sim 0.2$  eV difference in the energy bandgaps - even though this limits the light absorption, there is an advantage of adjusting the VBM by 0.2 eV to more positive potential energy thereby increasing its photooxidation capability.

Besides, downscaling the particle size of  $\text{TiO}_2$  hampers the bulk separation of excitons due to spatial proximity of the charge carriers [96]. In order to address these challenges, a suitable semiconducting material which has the following properties: (i) non-toxic constituents, (ii) chemically stable in aqueous solutions, and (iii) photoresistant to corrosion would be technically promising. In mitigating the recombination process to enhance the quantum efficiency, the strategy of employing internal electric field domiciled in polarizable semiconductor materials has always been preferably adopted. In principle, the internal electric field is directly connected to the electric polarization (surface charge density) in these polarizable material. Unfortunately, titanium dioxide does not possess this unique property but is a sublattice of the titanate class of polarizable semiconductors which the aforesaid property is omnipresent and will be discussed in the next section.

## 2.4 Barium titanate, $\text{BaTiO}_3$ , and its properties

Barium titanate,  $\text{BaTiO}_3$  sharing prototypical structure as the parent perovskite ( $\text{CaTiO}_3$ ) has been one of the extensively studied solid-state structures since 1945 [97]. As an archetype titanate perovskite, the general chemical formula follows the  $\text{ABO}_3$ ; where A- and B-site are di- and tetra-valent cations mostly composed of alkaline-earth (e.g. Sr, Ba etc.) and TM (e.g Ti, V, Fe etc.) respectively, and O is oxygen. In a typical unit cell, the  $\text{ABO}_3$  structure crystallizes with A-site cation located within the cuboctahedral cavities in 12-fold coordination, B-site cation at the center in 6-fold coordination while the O-anion are face-centered in 6-fold coordination (see figure 2.5). Therefore, each A-site cation shares a link by corner with a

net contribution of three (3)  $\text{TiO}_6$  octoedra i.e.  $1/2$  of each  $\text{TiO}_6$  octahedron. In the high temperature regime above  $130$  °C, it stabilizes in the centrosymmetric (cubic/paraelectric) phase where  $\text{Ti}^{4+}$  ion has no cooperative displacement with respect to  $\text{O}^{2-}$  ions.

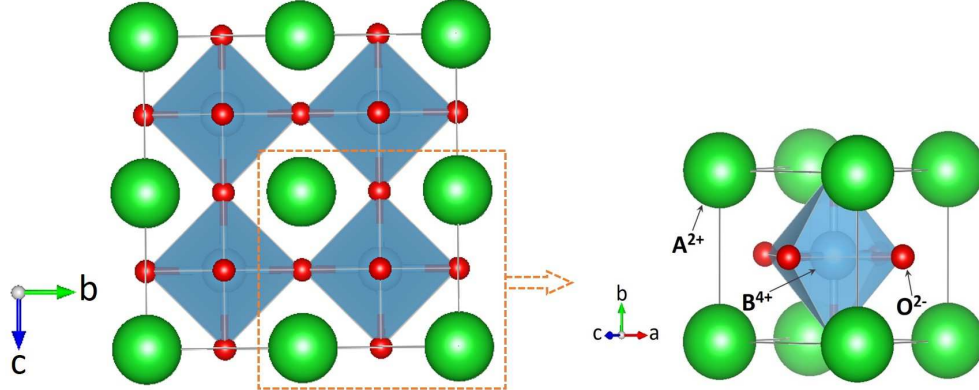


Figure 2.5: A typical unit cell (right) of  $\text{ABO}_3$  perovskite structure.

Since temperature affects the structural phase of barium titanate, other thermodynamic stable phases are also known to exist as a function of temperature. As displayed in figure 2.6, the successive phase transition sees the tetragonal phase ( $t\text{-BaTiO}_3$ , P4mm) stable between  $> 5$  °C and  $< 130$  °C, orthorhombic ( $o\text{-BaTiO}_3$ , Amm2) between  $< 0 - 5$  °C and rhombohedral ( $r\text{-BaTiO}_3$ , R3m) below  $< -80$  °C [98, 99]. In addition to the aforementioned phases, there exists a phase stabilizing above  $1460$  °C [100] known as the hexagonal,  $h\text{-BaTiO}_3$  (P4/mmm) for which the unit cell consists of  $2/3$  of  $\text{TiO}_6$  octahedra by face sharing to form  $\text{Ti}_2\text{O}_9$  dimer and  $1/3$  of  $\text{TiO}_6$  octahedra by corner sharing. Since off-centering of the transition-metal-occupied B-site is responsible for the ferroelectricity [101], the tetragonal, orthorhombic, rhombohedral and hexagonal phases are non-centrosymmetric and therefore polar. By considering the centrosymmetric phase in which ideally the lattice parameters,  $a = b = c$  and  $\alpha = \beta = \gamma = 90^\circ$ , it is seen that the lattice constant is related to the ionic radii of the individual lattice sites,  $a = \sqrt{2}(r_{\text{Ba}} + r_O) = 2(r_{\text{Ti}} + r_O)$ . The degree of distortion in the unit cell resulting from the off-centering of  $\text{Ti}^{4+}$  towards the oxygen atoms is estimated from the ratio of both lengths often called the Goldschmidt's tolerance factor,  $t$  [102]. Hence, the Goldschmidt's tolerance factor,  $t$  in this case is given as

$$t = \frac{(r_{\text{Ba}} + r_O)}{\sqrt{2}(r_{\text{Ti}} + r_O)} \quad (2.5)$$

where  $r_{\text{Ba}}$ ,  $r_{\text{Ti}}$ , and  $r_O$  are the ionic radii of  $\text{Ba}^{2+}$  (1.61 Å),  $\text{Ti}^{4+}$  (0.605 Å) and  $\text{O}^{2-}$  (1.40 Å),

respectively according to Shannon revised effective ionic radii [103]. For a stable structure,  $t = 1$  (mostly the cubic phase). When  $t > 1$ , the octahedron shows some degree of distortion and this lowers the crystal symmetry. Also,  $t < 1$  indicates instability resulting from A-site cation being probably too small. Apart from the tolerance factor estimation, another complementary assessment for stability of the  $\text{ABO}_3$  structure is through the fit of tetravalent cation (B-site) in the octahedron. It is expected that it satisfies the octahedral factor,  $\mu = \frac{r_{Ti}}{r_O} \geq 0.41$  [104] which is the stability limit before the  $\text{ABO}_3$  structure grows unstable.

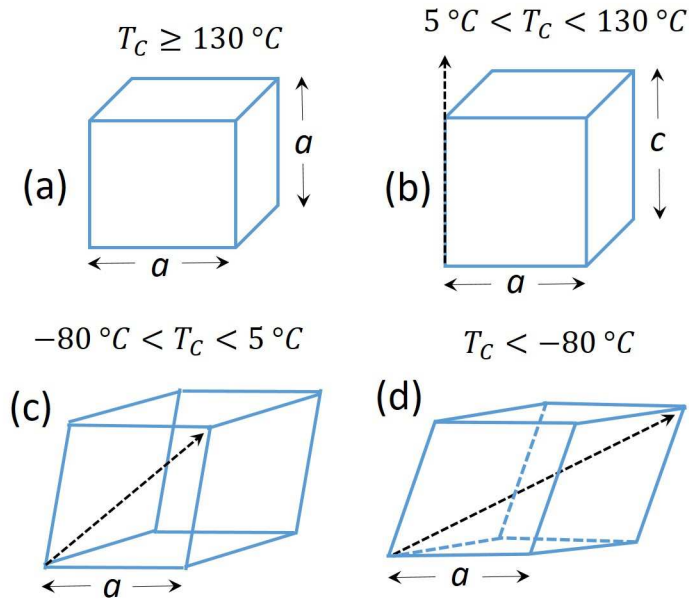


Figure 2.6: The structural phase transitions in  $\text{BaTiO}_3$  as temperature is lowered (a) cubic (b) tetragonal (c) orthorhombic, and (d) rhombohedral.

$\text{BaTiO}_3$  has a bandgap of 3.2 eV [105] as most  $\text{ABO}_3$  perovskites with wide bandgap, attributed to the bonding behaviour in Ba-O and Ti-O (and in a more generic way, A-O and B-O). Barium titanate has an optical band transition which is undefined [106, 107]. This implies the band transition comprises of both the direct and indirect. However, several optical absorption studies on barium titanate report the dominant transition i.e. indirect [105, 107, 108]. Similar to anatase  $\text{TiO}_2$ , the optical excitation in barium titanate is mainly indirect and emanates from the charge transfer mechanism between the O  $2p$  state valence band and the Ti  $3d$  state of the conduction band. For indirect transition, the charge carrier pathway furnishes the material with a prolonged lifetime sufficient enough for surface chemistry to take place before recombination occurs. In other words, non-radiative recombination constitutes

the major recombination in indirect transition. For instance, the time-resolved photoluminescence properties of  $\text{TiO}_2$  and  $\text{BaTiO}_3$  showed two different timescales i.e. the short and long corresponding to the surface-state and self-trapped exciton, respectively [109]. The time constants, extracted from these decay curves for the surface-state recombination are  $\sim 0.03$  ns ( $\text{TiO}_2$ ) [110, 111] and  $\sim 10$  ns ( $\text{BaTiO}_3$ ) [109, 112]. Comparatively,  $\text{BaTiO}_3$  has a carrier lifetime, two orders of magnitude larger than that of  $\text{TiO}_2$ , implying the photogenerated charges would remain separated long enough for a photochemical reaction. Again, the separation and ballistic transport of charges to the catalyst surface active sites is determined by the dielectric permittivity of the material. As shown in Chapter 1, the exciton's binding strength varies as the inverse of dielectric permittivity and reduces for a material with high dielectric permittivity. For the two prevalent phases of  $\text{TiO}_2$ , the relative dielectric permittivity,  $\epsilon_{\perp}$  is  $\sim 45$  (anatase) and  $\sim 110$  (rutile) [113, 114] whereas  $\text{BaTiO}_3$  is  $\sim 5000$  [115, 116] (i.e.  $\sim 111$  times more compared to the anatase and 46 times more compared to the rutile) implying a weak binding strength of the exciton and thus a high carrier mobility in return. While the properties of the oxides have been discussed to some extent, the complementary advantage pyroelectric  $\text{BaTiO}_3$  brings in comparison to the extensively used  $\text{TiO}_2$  are summarized in table 2.1.

Table 2.1: Summary showing similarities and differences between  $\text{TiO}_2$  (anatase) and  $\text{BaTiO}_3$  (tetragonal).

S/N	Factors considered	<i>a</i> - $\text{TiO}_2$	<i>t</i> - $\text{BaTiO}_3$
1.	Crystal symmetry & space group	Tetragonal & I41/amd	Tetragonal & P4mm
2.	Toxicity	No	No
3.	Chemical stability	Yes	Yes
4.	Dielectric permittivity, $\epsilon_{\perp}$	$\sim 45$ [113, 114]	5000 [115, 116]
5.	Carrier lifetime	$<< 1$ ns	$> 10$ ns
6.	Carrier separation mechanisms	None	BPVE
7.	Energy bandgap	3.2 eV	3.2 eV
8.	Scalability	Yes	Yes

## 2.5 Additional mechanism of charge carrier separation in non-centrosymmetric materials: Bulk photovoltaic effect (BPVE)

As stated previously, one of the key challenges in photocatalysis is the minimization of charge recombination upon absorption of photons. Therefore, enhancing the efficiency of the spatial separation ( $\eta_{e^-/h^+ \text{ separation}}$ ) and transport ( $\eta_{e^-/h^+ \text{ transport}}$ ) of excitons according to equation 1.2 is imperative. To address this, the use of non-centrosymmetric materials such as piezo-, pyro-, ferroelectrics etc. has been found useful. Its role in photochemistry with respect to spatial separation and ballistic transport of excitons to the photocatalyst surface is thus elaborated. The phenomenon first observed in 1956 [117] is advantageous in terms of enhanced quantum yield compared to conventional photovoltaic effect found in *p-n* junctions. In the latter, the mechanism is based on an asymmetry in the electric potential across the junction resulting in a net flow of photogenerated electrons and holes. The asymmetry in the electric potential creates an in-built electric field which separates the charge carriers. Due to the thermodynamic Shockley–Queisser (S-Q) limit, the open-circuit voltage is normally limited to the energy bandgap of the semiconductor. For the BPVE, it involves a coherent evolution of electron and hole wave-functions [118] and relates directly to the optical excitation process [119]. It is associated with the excitation of non-thermalized carriers i.e. hot carriers in the material, where the asymmetric distribution of momenta of these non-thermalized carriers gives rise to the mechanism of BPVE. These hot charge carriers typically relax at the bottom of the energy band through inelastic scattering over a free path length,  $l$  [120, 121]. Due to the path length, the electron distribution in this case is asymmetric and there is a net photocurrent density unlike in centrosymmetric material where the electron distribution is symmetric and the net photocurrent density is zero. The photo-excitation process of the two scenarios are depicted in figure 2.7. As a consequence, the ballistic transport of these charge carriers contributes maximally to charge-consuming catalysis. The omnipresence of this effect lies in the broken-inversion symmetry of the crystal which is a structural requirement and does not necessarily mean that the enhanced crystal electric polarization guarantees high magnitude of BPVE. Strictly speaking, the requirement being non-centrosymmetry and how much light the crystal can absorb holds when polarized light is applied. In a case of unpolarized light, the requirement is that the material must be polar and non-centrosymmetric. Pyro-/ferroelectric oxide perovskites are examples of these polar non-centrosymmetric crystals.

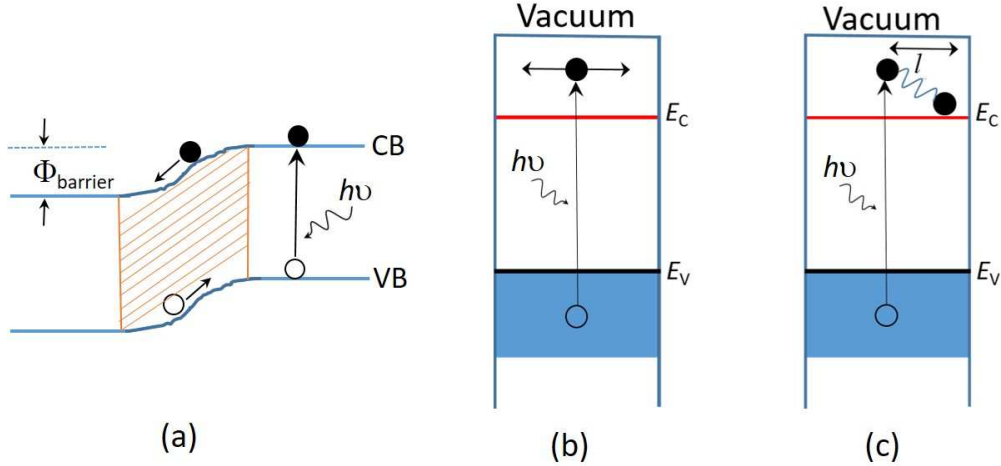


Figure 2.7: The photo-excitation process in a typical (a) *p-n* junction, (b) centrosymmetric, and (c) non-centrosymmetric material.

Although, polar crystals with strong distortion exhibit good photoresponse, light doping occupying the non-centrosymmetric site is usually the typical approach for an optimized yield. Consequently, the BPVE is expressed as a third rank tensor,  $\beta_{ijk}$ , which relates the photoinduced current density,  $J_i$  to the impinging optical electric field vectors, which in general do not need to be collinear as expressed in equation 2.6 [120]:

$$J_i = e_j e_k^* \beta_{ijk} I_0 \quad (2.6)$$

where  $e_{j/k}$  is the anisotropic electric field polarization vector in the  $j/k$  direction,  $\beta_{ijk}$  is the bulk photovoltaic tensor and  $I_0$  is the intensity of light incident on the non-centrosymmetric material. By using microscopic quantities, the photocurrent density can also be expressed as shown in equation 2.7 whereas the amplitude of the bulk photovoltaic tensor derived from this equation follows in equation 2.8 [122]:

$$J_i = e \alpha \left( \frac{I_0}{\hbar \omega} \right) l \quad (2.7)$$

$$\beta_{ijk} = e l \zeta \emptyset \left( \frac{1}{\hbar \omega} \right) \quad (2.8)$$

wherein  $e$  is the elementary charge,  $\alpha$  is the absorption coefficient,  $l$  is the mean free path of excited charge carriers,  $\zeta$  is the excitation asymmetry,  $\emptyset$  is the quantum yield, and  $\hbar \omega$  corresponds to the photonic energy. As can be seen from the tensorial property of  $\beta_{ijk}$  in

equation 2.6, the photocurrent is not necessarily in the same direction as the electric field polarization. Moreover, the flow of photocurrent dissipating energy implies that the BPVE cannot exist in the absence of light absorption. Again, the photocurrent (just as the BPVE) is enhanced when the size of the non-centrosymmetric material is of the order of  $l$ , since all the photoexcited charge carriers contribute to current density in the case of photovoltaics and charge-consuming catalytic reaction in the case of photocatalysis (see equation 2.7).

## 2.6 Relationship between crystal structure and presence of permanent dipoles

While the presence of spontaneous polarization in polar materials is only an evidence of the broken-inversion symmetry (i.e. non-centrosymmetry), there is no one-to-one correlation between the strength of spontaneous polarization and BPVE [123]. This shows that a structural requirement is mandatory for the manifestation of the latter. Out of the 32 crystallographic space groups, 20 are non-centrosymmetric, and therefore meets the requirement for third rank tensors. This shows that there is a relationship between structure and the BPVE. The structural prerequisite for the BPVE is non-centrosymmetry. The existence of a spontaneous polarization (volume integral of all dipoles) goes beyond the requirement of non-centrosymmetry and restricts the choice to 10 crystal classes, all of which are now lacking inversion symmetry and exhibiting pyroelectricity, for which a spontaneous polarization is required. While it is difficult to quantify a degree of non-centrosymmetry in general, the amplitude of the spontaneous polarization in pyroelectric systems (including the room temperature phase of  $\text{BaTiO}_3$ ) is an indicator of the degree of non-centrosymmetry. In particular, the loss of spontaneous polarization will then coincide with a loss of all odd-rank tensors, including the BPVE.

### ◊ Temperature dependence of spontaneous polarization

A typical unit cell of the high temperature phase of barium titanate (figure 2.6a) is centrosymmetric (cubic) and belongs to the  $m3m$  space group. In the cubic phase, the temperature dependence of relative dielectric permittivity follows the well-known Curie-Weiss law,  $\varepsilon = C/(T - T_C)$ , where  $C$  is the Curie-Weiss constant, and  $T_C$  is the Curie temperature [124]. Cooling below the  $T_C$ , there is an emergence of spontaneous polarization as it undergoes a series of structural transitions. Moreso, the dielectric

permittivity and tetragonality changes as a function of temperature as shown in figure 2.8. The presence of which is due to the net electric dipole moment arising from the displacement of  $\text{Ti}^{4+}$  and  $\text{O}^{2-}$  ions.

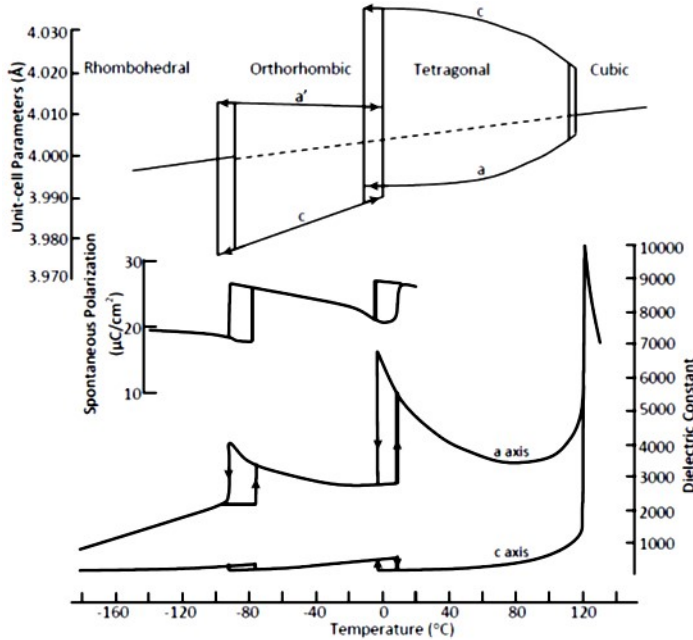


Figure 2.8: Structural transitions in  $\text{BaTiO}_3$  showing the variation of dielectric permittivity, spontaneous polarization and tetragonality upon cooling down. Figure adapted from Aksel and Jones [125].

The displacive phase transitions herein are first order with softening of relative dielectric permittivity in accordance with the Lyddane-Sachs-Teller (LST) relation which links the ratio of longitudinal and transverse optic mode frequencies to the ratio of relative dielectric permittivities at frequencies lower and higher than the ionic relaxation's resonance frequency i.e.  $\frac{\omega_{LO}^2}{\omega_{TO}^2} \simeq \frac{\varepsilon_s}{\varepsilon_\infty}$  [126]. Therefore, for the three main structural transitions from the high temperature cubic phase, the dielectric permittivity although distinct in magnitude is maximum at the various transition temperatures [127].

#### ◊ Particle size dependence of spontaneous polarization

Spontaneous polarization is mainly affected by the structural properties and in some cases, the chemical composition of the crystal. Apart from the Curie temperature which decreases with grain size, the distortion of the unit cell,  $c/a - 1$  tends to zero and vanishes at a critical particle size. This phenomenon referred to as superparaelectric limit has been explained by different models [128–130]. In particular, the composite structure

model (figure 2.9) illustrating the variation of spontaneous polarization as the particle is reduced demonstrates that for a non-centrosymmetric crystal in spherical geometry, it comprises of a tetragonal core whose tetragonality ( $c/a$ ) is always larger than unity i.e. ( $c > a$ ), a gradient lattice strain layer (GLSL) where there is a gradual change in tetragonality i.e.  $c$  and  $a$  decreases and increases, respectively; and a surface which is predominantly cubic ( $c = a$ ). Therefore, below the critical size it is impossible to sustain the tetragonal core.

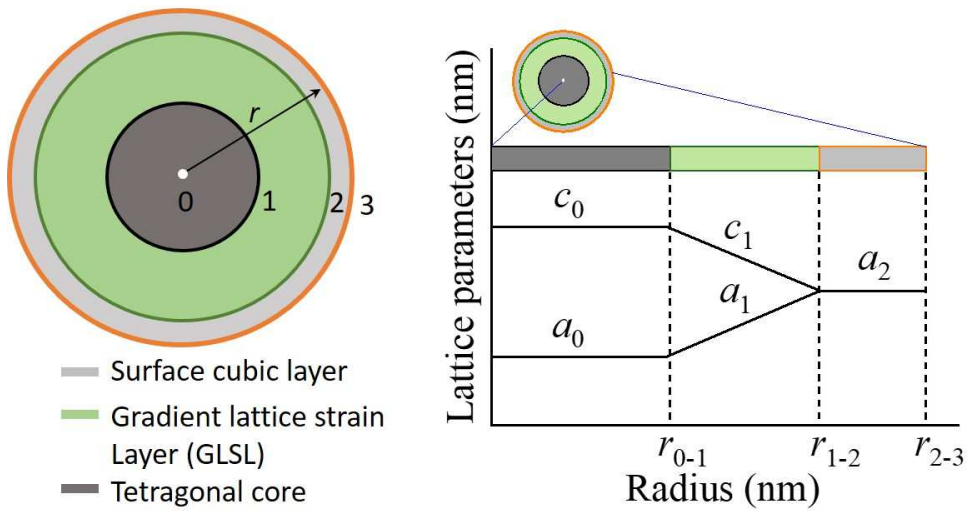


Figure 2.9: The composite structure model used in explaining tetragonal-to-cubic phase transition in non-centrosymmetric crystal.

## 2.7 Approaches to study particle size effect in non-centrosymmetric materials

At nanoscale, the spontaneous polarization in polar materials completely disappears below a certain critical size and the high symmetry cubic phase is favoured instead. Both experimental and theoretical results [131–134] elaborating the size effect on tetragonality, Curie temperature, spontaneous polarization, soft mode Raman frequency, dielectric permittivity, latent heat etc. have been reported. In principle, some approaches have been satisfactorily applied in explaining the size-driven phase transition in pyroelectrics namely: (i) the local field theory based on the Ising model [135], and (ii) a more quantitative approach based on the Landau-Ginzburg-Devonshire (LGD) formalism [133]. The Ising model considers the nearest-neighbour interactions between spins of distinct binary states. In the electrostatic

interpretation, the Ising spin variables can be taken as the two equilibrium configuration of spontaneous polarization i.e.  $\pm P_S$ . For the LGD model, also referred to as the mean field theory, the conceptual framework is based on a system with long-range interactions and the spatial averaging of the all local fluctuations [136]. Within the scope of this thesis, we considered the LGD and it is valid for particles in the regime,  $x > x_0$ ; where  $x_0$  is the critical particle size.

### 2.7.1 Phenomenological Landau-Ginzburg-Devonshire (LGD) formalism

In the context of composite structure model, the LGD phenomenological theory expresses the Gibbs free energy density function in terms of an independent order parameter like polarization, magnetization or stress; allowing the expansion to be used to determine its coefficients via some measured observables of the material. For polar materials, the Gibbs free energy of a system as a function of the order parameter, polarization  $P$ , particle size  $x$ , and temperature  $T$  is therefore given as [133]:

$$G(x, T, P) = G_0 + \frac{1}{2} \int \left( \alpha_0(T - T_C)P^2 + \frac{1}{2}\beta P^4 + \frac{1}{3}\gamma P^6 + \phi(\nabla P)^2 \right) dV + \frac{\phi}{2\delta} \int P^2 dS \quad (2.9)$$

where  $\alpha$ ,  $\beta$ ,  $\gamma$ ,  $\phi$  and  $\delta$  are all material parameters.  $G_0$  is the residual free energy of the disordered cubic phase at high temperature. Apart from  $\alpha$  which depends on temperature, the other phenomenological coefficients,  $\beta$  and  $\gamma$  are temperature independent and the last two terms measure the distortion energy of the polarization inhomogeneity and surface effect. For some oxide perovskites like  $\text{BaTiO}_3$ ,  $\text{PbTiO}_3$  etc., the phenomenological coefficients are already known [133, 137]. Due to symmetry, the odd powers of  $P$  are completely absent as observed in equation 2.9.

For convenience and simplification purpose, we considered the two prevalent stable phases (i.e tetragonal (ordered) and cubic (disordered) phases existing below and above the  $T_C$ , respectively) on one hand and neglected the contribution of surface effects such as grain boundaries, dislocations etc. on the other hand. By minimizing the Gibbs free energy at thermal equilibrium ( $\frac{dG}{dP} = 0$ ), the Euler-Lagrange equation assuming a spherical particle is obtained:

$$\phi \left( \frac{\partial^2}{\partial x^2} + \frac{2\partial}{x\partial x} \right) P + \alpha_0(T - T_C)P + \beta P^3 + \gamma P^5 = 0 \quad (2.10)$$

Applying the boundary condition,  $\frac{\partial P}{\partial x} + \frac{P}{\delta} = 0$  where  $\delta > 0$  at phase transition yields the

maximum polarization  $P = P_\infty$  and near the surface i.e.  $\delta < 0$  yields the minimum polarization  $P = 0$  [138]. Possible solutions of equation 2.10 exist though three of which are stable at

$$\begin{cases} P = \pm \sqrt{-\beta + \frac{\sqrt{\beta^2 - 4\alpha_0(T-T_C)\gamma}}{2\gamma}} & ; T < T_C \\ P = 0, \pm \sqrt{-\beta - \frac{\sqrt{\beta^2 - 4\alpha_0(T-T_C)\gamma}}{2\gamma}} & ; T_C < T < T' \\ P = 0 & ; T' < T \end{cases} \quad (2.11)$$

where  $T'$  denotes the temperature that is very close to the Curie temperature for which the material becomes structurally unstable. An expression for the size dependent Curie temperature can be derived by substituting the first two solutions of equation 2.11 in equation 2.9. This yields

$$\begin{cases} G(T) = G_0 & ; \text{for } T > T_C \\ G(T) = G_0 - \frac{(\beta^2 - 4\alpha_0(T-T_C)\gamma)^{\frac{3}{2}}}{24\gamma^2} - \frac{\alpha_0(T-T_C)\beta}{4\gamma} + \frac{\beta^3}{24\gamma^2} & ; \text{for } T < T' \end{cases} \quad (2.12)$$

The exact temperature for which the material transforms to cubic phase can be solved by equating both expressions leading to

$$-\frac{(\beta^2 - 4\alpha_0(T-T_C)\gamma)^{\frac{3}{2}}}{24\gamma^2} - \frac{\alpha_0(T-T_C)\beta}{4\gamma} + \frac{\beta^3}{24\gamma^2} = 0 \quad (2.13)$$

Equation 2.13 can further be simplified by dividing through with  $\frac{\beta^3}{24\gamma^2}$  and this gives  $\left| \left( 1 - \frac{4\alpha_0(T-T_C)\gamma}{\beta^2} \right)^{\frac{3}{2}} \right| - \frac{6\alpha_0(T-T_C)\gamma}{\beta^2} + 1$ . Assuming  $y = \frac{\alpha_0(T-T_C)\gamma}{\beta^2}$ , we get a function that is expressed in terms of  $y$ .

$$\left| (1 - 4y)^{\frac{3}{2}} \right| - 6y + 1 \quad (2.14)$$

Equation 2.14 has a solution at  $y = \frac{3}{16}$ ; implying that  $\frac{3}{16} = \frac{\alpha_0(T-T_C)\gamma}{\beta^2}$ , which yields additional term to the size dependent Curie temperature,  $T - T_C = \frac{3\beta^2}{16\alpha_0\gamma}$ . Therefore, a more complete size-dependent Curie temperature fitting function similar to the one found in Ishikawa et al. [139] and Jiang and Bursill [134] is given as

$$T_C(x) = T_C(\infty) \left[ 1 - \frac{B}{x - x_0} \right] + \frac{3\beta^2}{16\alpha_0\gamma} \quad (2.15)$$

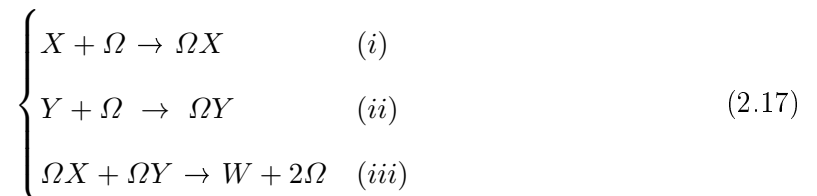
and will be elaborated in the Section 4.2.

## 2.8 Size effect on the catalytic kinetics of redox reaction

The turnover frequency (ToF) in heterogeneous photocatalysis quantifies the photocatalytic kinetics occurring at a specific surface active site per time. The downscale of the particle size therefore affects the number of surface active sites as the domains that contain the active sites become unstable, thus the ToF is influenced due to the structure sensitivity arising from changes in physicochemical properties of the photocatalyst [140]. Here, the reaction kinetics depend on the mass transport mechanism of photocatalytic solid–liquid interface based on the underlying operating conditions especially for the Langmuir-Hinshelwood (L-H) type. To study the particle size effect on the catalytic kinetics, a theoretical framework often called the thermodynamic model was proposed [141]. The approach has been applied to reaction between two adsorbed molecules (i.e. L-H mechanism) or reaction between a gas molecule and an adsorbed molecule (i.e. Eley-Rideal mechanism) [142]. According to thermodynamic approach, the chemical potential is used to describe such reaction kinetic as the particle size changes. It is well-known that the chemical potential is used to determine the change of free energy when the number of molecules of the catalytic material changes due to particle size. At thermodynamic equilibrium, the chemical potential can be treated as Gibbs free energy. Thus the Gibbs free energy of equation 2.9 excluding the gradient and surface effect terms is re-written as

$$G(x, T, P) = G(\infty) + \Delta G(x, T, P) \quad (2.16)$$

For example, if the thermal effect from solar illumination is negligible then the free energy entirely depends on particle size ( $x$ ) and spontaneous polarization ( $P$ ). We then consider a set of reactions (X - parent and Y - intermediate organic species), which is irreversible and it is expected that there is a competition between them [142]



where  $\Omega$  is the available surface active sites. The particle size-dependent degradation rate,  $k(x)$  for this kind of first-order L-H is determined from the competition of both processes as

[142]

$$k(x) = \frac{k_3 K_1 C_X K_2 C_Y \exp\left(\frac{-2\alpha\eta}{x}\right)}{\left(1 + (K_1 C_X + K_2 C_Y) \exp\left(\frac{-\eta}{x}\right)\right)^2} \quad (2.18)$$

where  $K_{1..3}$  are the adsorption equilibrium constants for the reactions in equation 2.17(i) - (iii),  $k_3$  is the Langmuir adsorption constant for the reaction in equation 2.17(iii),  $C_{X/Y}$  is the concentration of X/Y in the liquid phase,  $\alpha$  is Polanyi parameter. Comparison of the reaction kinetics for particles of different sizes is often done per unit weight of the catalyst and this involves relating the reaction kinetics with the active surface area for the material. Accordingly, the total surface area is given as  $3/x\rho$  [141], so that the reaction rate per unit weight of the surface area,  $k'(x)$  becomes

$$k'(x) = k(x) \cdot A_{surface} = \frac{k_3 K_1 C_X K_2 C_Y \exp\left(\frac{-2\alpha\eta}{x}\right)}{\left(1 + (K_1 C_X + K_2 C_Y) \exp\left(\frac{-\eta}{x}\right)\right)^2} \frac{3}{x\rho} = \frac{A' \exp\left(\frac{-2\alpha\eta}{x}\right)}{\left(1 + A'' \exp\left(\frac{-\eta}{x}\right)\right)^2} \frac{1}{x} \quad (2.19)$$

where  $A' = \frac{3k_3 K_1 C_X K_2 C_Y}{\rho}$ ,  $A'' = K_1 C_X + K_2 C_Y$ , and  $\rho$  is the density of catalyst ( $6020 \text{ kg/m}^3$  for BaTiO<sub>3</sub> [143]). Equation 2.18 and 2.19 are technically the same. Moreover,  $\eta = 2\sigma V_M / RT$  has the dimension of particle size and depends on the surface tension,  $\sigma$  of the particle, similar to equation 3 in Uchino et al. [144].  $V_M$ ,  $R$ , and  $T$  are the molar volume ( $\text{m}^3 \text{mol}^{-1}$ ), universal gas constant ( $8.314 \text{ JK}^{-1} \text{mol}^{-1}$ ) and temperature (K). While the prefactor in equation 2.19 accounts for loss of degradation rate for very small particles, the inverse dependence on  $x$  can be seen for large particles. Figure 2.10 displays a typical plot of equation 2.19 for different values of  $\eta$ . As the size decreases, the rate of reaction increases showing an increased mass transport or diffusion between the solid-liquid interface. The size effect on the reaction rate is observed by the presence of the peak between 2 - 4 nm, which becomes less pronounced at high values of  $\eta$ . The decrease in the rate of reaction for very small particles i.e.  $r < 2 \text{ nm}$  depicts the domain instability in the clustered particles with very limited number of active sites.

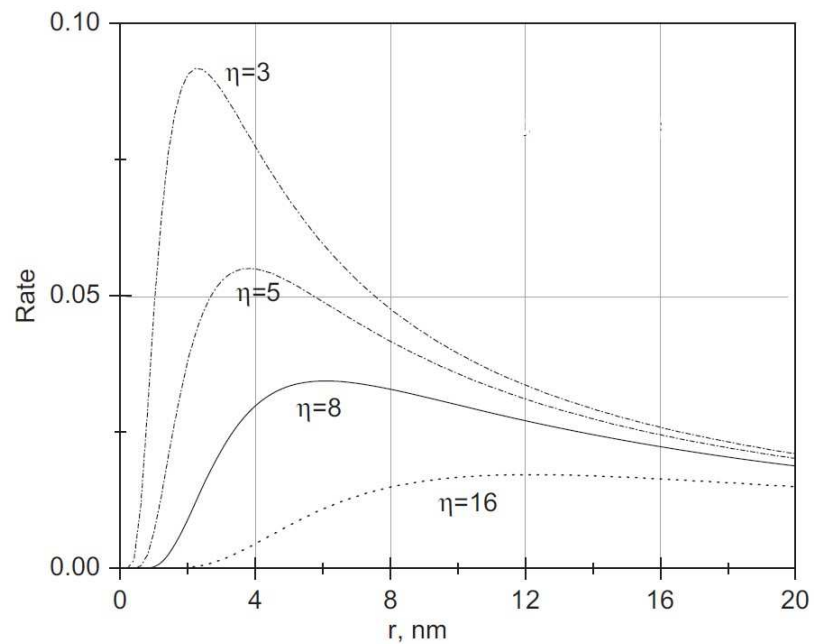


Figure 2.10: The size dependent reaction rate for different values of  $\eta$  according to equation 2.19. Figure is adapted from Murzin [142].



# Chapter 3

## Experimental techniques

### 3.1 Synthesis of BaTiO<sub>3</sub> nanoparticles: Microwave-assisted hydrothermal technique

Unlike the high temperature solid-state reactions that are based on solid-state diffusion, the hydrothermal method rather depends on the solution phase mass transport. The thermodynamic insight to a conventional hydrothermal technique shows that solutions of the cationic and anionic precursors are used to precipitate the oxide perovskite of interest in a single step at elevated temperature and pressure above 100 °C and ca. 0.1 MPa [145]. While the conventional hydrothermal method is advantageous, the extended processing times culminating to agglomeration and loss of chemical homogeneity pose a challenge [146]. To circumvent this, the microwave-assisted counterpart utilizes the *in-situ* microwave energy to produce autogenous pressure which ensures rapid heating of content of the closed system. In comparison to the conventional type, the microwave-assisted hydrothermal technique has the following advantages: (i) accelerated crystallization of product (ii) cost effectiveness (iii) reproducibility of target product (iv) energy efficient, and (v) economical [36]. In spite of the numerous advantages, there are still a few disadvantages such as poor control over reaction parameters and even time-dependent monitoring of the growth process is rather unfeasible [147]. A microwave is a non-ionizing electromagnetic radiation of frequency 2.45 GHz i.e. ca.12.23 cm with high penetration depth. The mechanism is basically an ionic conduction due to interaction of dielectric materials either in liquid, solid or both phases with the microwave radiation. This offers an advantage as it enhances the rate of nucleation with corresponding reduction in synthesis time

enabling phase selectivity [148] and control of crystal morphology [149]. A typical schematic of a standard microwave oven is displayed in figure 3.1(a) whereas the transverse section of the magnetron illustrating the production of energetic microwave radiation is depicted in figure 3.1(b) .

Notably, once connected to a power source electrons generated from the cathode are subjected to an electric force,  $F_e$ . These accelerated electrons are further confined to a cyclic path in the presence of an electromagnetic field due to Lorentz force,  $F = e(E + vB)$ ; where  $e$ ,  $v$ ,  $E$ , and  $B$  are electronic charge, velocity, electric field and the magnetic field.

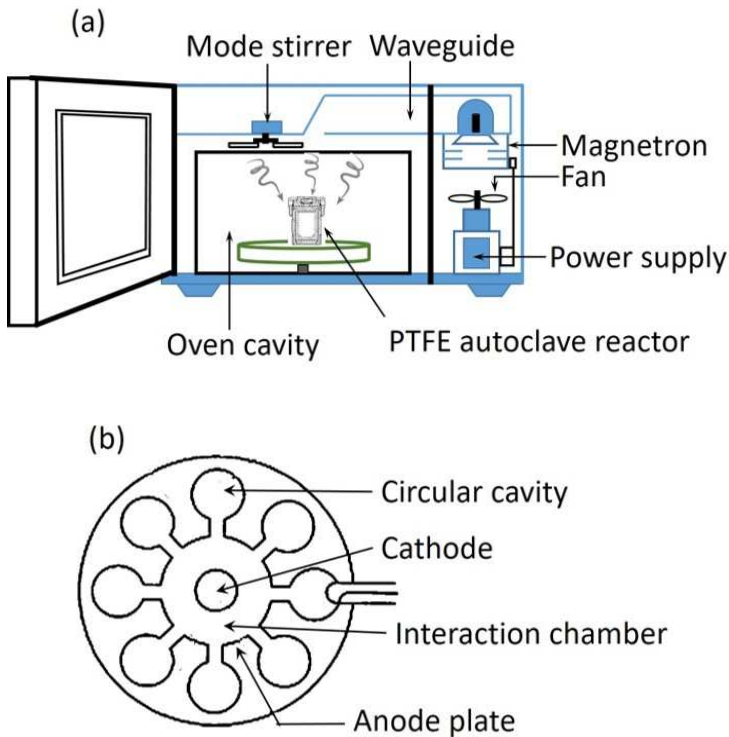


Figure 3.1: The schematic illustration of a (a) standard microwave oven operating at a frequency of 2.45 GHz, and (b) magnetron.

The joint exertion of both forces complicates the trajectory followed by these electrons and as such they get snapped into the circular cavity located inside the anode [150]. Since the cavity resonates at 2.45 GHz frequency, it leads to cascades of electrons with periodic oscillations. As a consequence, the energy generated is transmitted into the oven cavity through an inductor-like material coupled to the resonant cavity. The microwave heating of dielectrics in solvents such as water therefore stems from the reorientation of solvent's dipoles as their phase lags behind the electric field. It follows that the effective power density ( $\text{W/m}^3$ ) absorbed by the

dielectric material can be derived from the expression [151]:

$$P = \omega\epsilon_0\epsilon'(\tan\delta)E^2 \quad (3.1)$$

where  $\omega = 2\pi f$ ;  $\tan\delta = \frac{\epsilon''}{\epsilon'}$ ;  $\epsilon_0 = 8.854 \times 10^{-12} \text{ F/m}$ ,  $f$  is frequency (Hz),  $\epsilon'$  and  $\epsilon''$  correspond to real and imaginary part of dielectric permittivity in  $\epsilon = \epsilon' + i\epsilon''$ , and  $E$  is the electric field intensity (V/m). The energy for a unit volume of the dielectric content is then determined by multiplying equation 3.1 with the time interval of microwave irradiation,  $\Delta t$ . The transformation is further simplified to obtain the time rate of change of temperature (equation 3.3) in the cooking cavity, which has an inverse dependence on the specific heat capacity  $C$  and density  $\rho$  of the dielectric material [152]:

$$Q = \omega\epsilon_0\epsilon'(\tan\delta)E^2\Delta t = mc\Delta T \quad (3.2)$$

$$\frac{\Delta T}{\Delta t} = \frac{\omega\epsilon_0\epsilon'(\tan\delta)E^2}{C\rho} \quad (3.3)$$

## 3.2 Characterization techniques

### 3.2.1 X-ray diffraction

Generally, X-ray diffraction (XRD) is a useful analytical technique for the investigation of crystallographic structures and atomic spacing in materials. This arises from the fact that the wavelength of X-ray is typically of the same dimension as the inter-atomic spacing in crystals. While a Bruker D8 Advance diffractometer equipped with Cu-K $\alpha$  radiation was used for this study, a typical X-ray diffractometer consists of a cathode ray tube, filter (to produce a monochromatic beam), collimator, and detector as shown in figure 3.2(a). The collimated X-ray beam is therefore directed onto the sample whereas a goniometer is used to maintain the incident angle and rotate the sample in the beam path. The detector mounted at one end rotates at a  $2\theta$  angle in order to record the intensity of the diffracted ray, which appears as the Fourier transformation of the electron density. Since the interaction process with the sample produces a constructive interference that must satisfy Bragg's law, the difference in path length becomes an integral multiple of the X-ray wavelength as given by equation 3.4 (see figure 3.2) [153].

$$n\lambda = 2d_{hkl} \sin \theta \quad (3.4)$$

where  $n$ ,  $\lambda$ ,  $d_{hkl}$ , and  $\theta$  are an integer representing the order of reflection, X-ray wavelength, inter-atomic/planar spacing and diffraction angle, respectively.

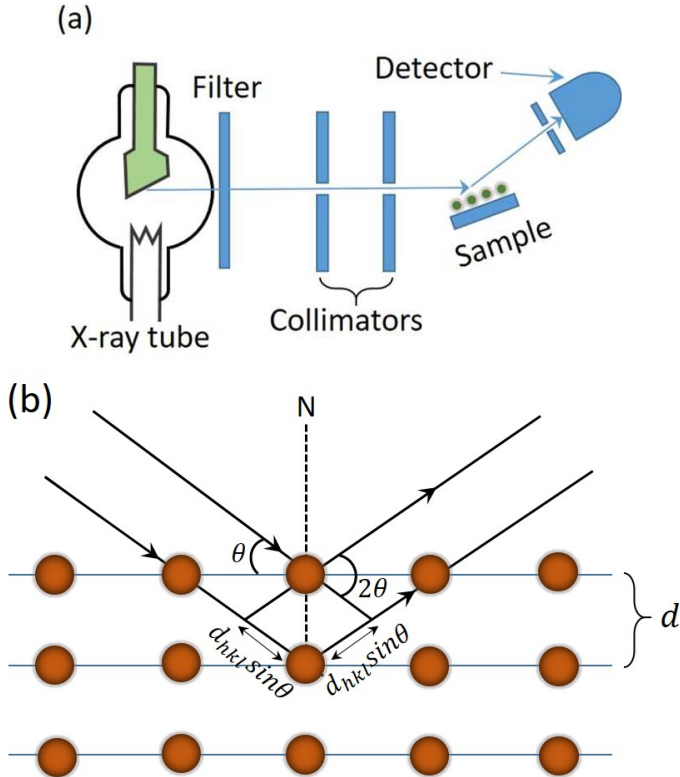


Figure 3.2: (a) The major components of X-ray diffractometer (b) Illustration of diffraction of monochromatic X-ray incident on atomic planes of a material.

### 3.2.2 Raman spectroscopy

Raman spectroscopy is a non-destructive optical spectroscopic tool which is based on the Raman effect. The Raman effect implies that a certain amount of vibrational energy is gained (for anti-stokes) or lost (for stokes) in comparison to the energy of the incident photon. For this reason, Raman spectroscopy is employed for both quantitative and qualitative analysis of materials [154]. In the quantitative analysis, the intensity of the scattered light is monitored in order to estimate the concentration of analyte in the material (since there is a proportional relationship between both) whereas in the qualitative analysis, the frequency of the scattered light is used to identify the material based on the produced spectrum [155, 156]. Prior to explaining the physics behind the Raman effect, let us first examine the major components of

this analytical tool. In a typical Raman setup, the major components consist of the following (see figure 3.3):

- ◊ A highly monochromatic excitation source,
- ◊ A sample irradiation and collection system,
- ◊ A spectrometer, and
- ◊ A detector typically charge-coupled device (CCD).

Technically, lasers are used as illumination source to enhance the intensity of the scattered light after interaction. This stems from the fact that lasers are monochromatic source. The material is excited with the laser light and the radiation emitted from the illuminated spot is then collected through a lens and transmitted to the spectrometer. Prior to transmitting to the spectrometer, a notch (band-stop) filter is used to filter out the dominant Rayleigh light while allowing the frequency of the Raman scattered light (Stokes) unattenuated. The intensity of the Raman scattered light (Stokes) varies inversely as the fourth power of wavelength i.e.  $I_S \propto I_0 (\omega_0 - \omega_R)^4 [(\frac{\partial\alpha}{\partial k})_{k=0}]^2 \implies I_S \propto \lambda^{-4}$  [157]. A grating is then used to disperse the Raman scattered light onto a detector preferably CCD [154, 158, 159].

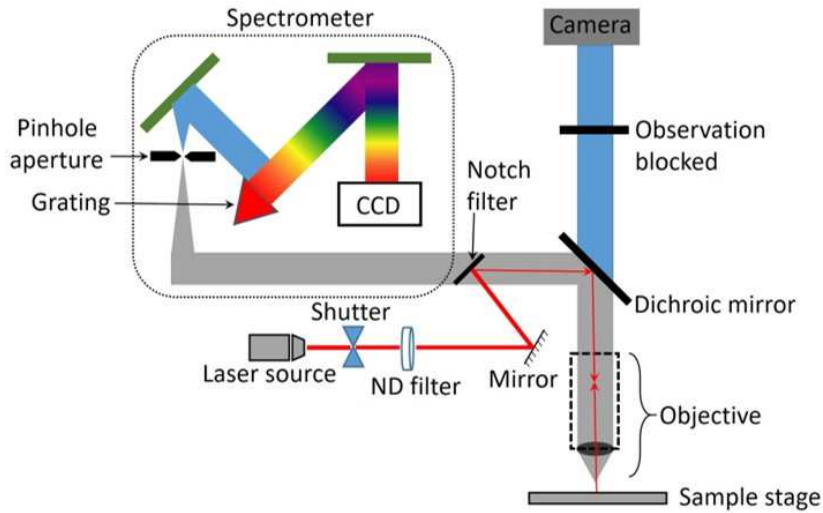


Figure 3.3: A typical Raman system indicating the major components.

The CCD has the capability of integrating the converted optical-to-charge signals impinging on it and finally transferring them to a readout device. In this study, all the Raman measurements were performed using a Horiba iHR320 equipped with a thermoelectrically cooled Horiba

Scientific Synapse Back-Illuminated Deep Depletion CCD detector. The excitation source is a 473 nm solid state blue Cobolt 04-01 laser (linearly polarized, TEM00).

### 3.2.2.1 Principles

Atoms of a material generally become polarized when illuminated with a light of substantial energy creating an induced electric dipole in the molecules. This electric dipole moment otherwise referred to as the electric polarization scales linearly with the electric field, ( $E = E_0 \cos(\omega_0 t)$ ) given by  $P = \alpha E$ , where  $\alpha$  is the polarizability, which defines the ease with which a charged particle respond to electric field. The polarizability on the other hand, shows dependence on the relative displacement,  $k = k_0 \cos(\omega_R t)$ , which the Taylor series expansion can be approximated as:

$$\alpha = \alpha_0 + \sum \left( \frac{\partial \alpha}{\partial k} \right)_{k=0} k + \frac{1}{2} \sum \left( \frac{\partial^2 \alpha}{\partial k^2} \right)_{k=0} k^2 + \dots \quad (3.5)$$

The electric polarization follows from the preceding expression of  $P = \alpha E$  as:

$$P = \left[ \alpha_0 + \sum \left( \frac{\partial \alpha}{\partial k} \right)_{k=0} k + \frac{1}{2} \sum \left( \frac{\partial^2 \alpha}{\partial k^2} \right)_{k=0} k^2 + \dots \right] \times E_0 \cos(\omega_0 t) \quad (3.6)$$

Considering that the third and other higher terms are anharmonic, they are often neglected and then equation 3.6 can be simplified by assuming that  $\cos A \times \cos B = \frac{1}{2} \{ \cos(A - B) + \cos(A + B)\}$ :

$$P = \left[ \alpha_0 E_0 \cos(\omega_0 t) + \frac{1}{2} \sum \left( \frac{\partial \alpha}{\partial k} \right)_{k=0} k_0 E_0 \cos(\omega_0 t - \omega_R t) + \frac{1}{2} \sum \left( \frac{\partial \alpha}{\partial k} \right)_{k=0} k_0 E_0 \cos(\omega_0 t + \omega_R t) \right] \quad (3.7)$$

From equation 3.7, the first, second and third term correspond to Rayleigh, Stokes and Anti-Stokes scattering, respectively while  $\omega_R$  denotes the frequency of scattered phonons. These scattering processes corresponding to the oscillation frequency of the excitation source, loss in energy (Stokes) and gain in energy (Anti-Stokes) are described in figure 3.4.

### 3.2.2.2 Modes of vibration

While phonon or lattice vibration is essential in determining the type of scattering i.e. Brillouin or Raman, the distinction depends on the occupation number and crystal symmetry selection rule. For this reason, there are two types of phonon modes namely:

- ◊ Acoustic phonons - This type of phonon modes typically carries small energy  $\sim \frac{k_B T}{n(\omega)}$  as  $k \rightarrow 0$ , and of course, zero energy when  $k = 0$ . The vibration of the neighboring atoms in this case are in phase (figure 3.5(a)). It can also be longitudinal or transverse if the displacement is in the direction or perpendicular to its propagation denoted as LA or TA, respectively.
- ◊ Optical phonons - This phononic modes carry substantial energy as  $k \rightarrow 0$  and the vibration of the neighboring atoms are out of phase (figure 3.5(b)). Again, with respect to the propagation, the displacement can be longitudinal or transverse if it is in the direction or perpendicular to the source denoted as LO or TO, respectively.

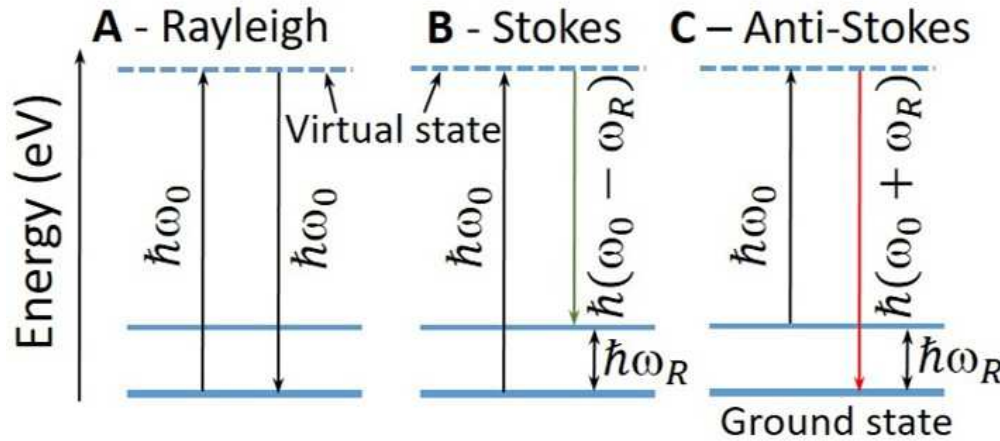


Figure 3.4: The different scattering processes (a) Rayleigh (b) Stokes, and (c) Anti-Stokes. The broken lines denote the virtual state.

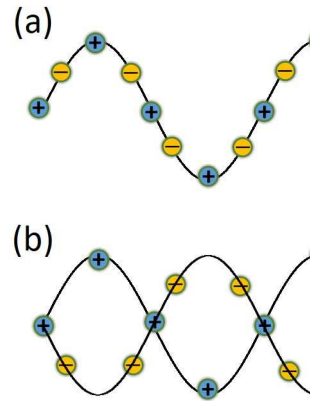


Figure 3.5: Distinction between (a) acoustic, and (b) optical phonon modes.

### 3.2.3 X-ray photoelectron spectroscopy

The X-ray photoelectron spectroscopy (XPS) is based on the photoelectric effect; and it is used to monitor the kinetic energies of the ejected Auger and photoelectrons. Basically, the X-ray targets like Al-K $\alpha$  (1486.6 eV) or Mg-K $\alpha$  (1253.6 eV) [160] are mainly used depending on the configuration of the instrument. As the process is entirely a surface phenomenon, the penetration depth is a few tens of nanometer (< 10 nm [161]) and the principle is based on the photoelectric effect where the binding energy, BE is quantitatively estimated from the equation below:

$$BE = h(\nu - \nu_0) - \frac{mv^2}{2} \Rightarrow h\nu - \phi - KE \quad (3.8)$$

where  $\phi = h\nu_0$ ,  $h\nu$  and  $KE$  are work function, photonic energy of the X-ray and kinetic energy, respectively and  $m$  is the Planck's constant ( $6.625 \times 10^{-34}$  Js). In principle, when soft X-ray photons are incident on a material, the core shell electrons are ejected while electrons from the higher energy level lose some energy to replace the vacuum. At the same time, the post-photoemission process may culminate to ejection of Auger electrons due to relaxation of the ions or instability of the resulting atom. The entire processes are illustrated in figure 3.6.

Generally, only electrons without energy loss can be counted by the electron analyzer in the detector and forms the XPS spectrum while those participating in inelastic loss process form the background of the XPS spectrum. In this study, XPS spectra were acquired with a VG Escalab 220i XL equipped with a monochromatic Al-K $\alpha$  source and operated at 15 kV/20 mA.

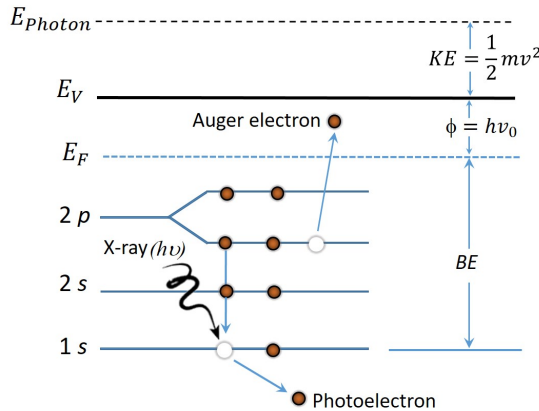


Figure 3.6: Emission processes leading to both Auger and photoelectrons in X-ray photoelectron spectroscopy.

### 3.2.4 Transmission electron microscopy

The transmission electron microscopy (TEM) is a combination of imaging and electron diffraction technique which uses an energetic electron beam to provide information such as structure, diffraction patterns, dislocations and grain boundaries etc. about the probe material. Unlike the optical microscope with wavelength in the range  $\lambda_{visible} \sim 400 - 800$  nm, the electron beam with wavelength,  $\lambda_{electron} \sim 0.004$  nm for  $V_a = 100$  kV is far less than the typical distance between two atomic planes, and can be modulated by varying the accelerating voltage. The high spatial resolution stemming from this short wavelength paves way for studying structural properties of a material on the atomic scale. A typical TEM consists of electron gun (a hot cathode that produce the streams of energetic electrons), illumination system (set of electromagnetic lenses), and imaging system (see figure 3.7).

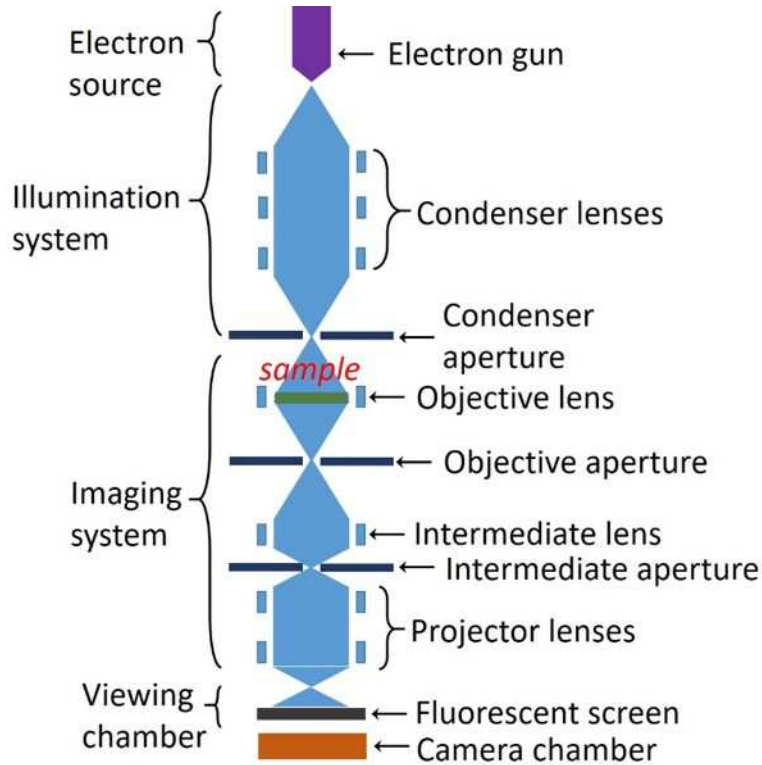


Figure 3.7: The major components of a typical transmission electron microscopy.

Emitted electrons in accordance with Richardson law [162] (i.e.  $J \propto T^2 \exp\left(\frac{-\phi}{k_B T}\right)$ , where  $J$ ,  $T$ ,  $\phi$ ,  $k_B$  are current density, absolute temperature, cathode material's work function and Boltzmann constant) from the hot cathode through the process of thermionic emission are directed to the sample via a set of lens arranged in the illumination system compartment.

Depending on the material's thickness and electron transparency, part of the beam get transmitted (i.e. scattered beam caused by an interaction of electrons with the material) and are focused on the objective lens. The scattered beam is finally deflected in the electromagnetic field to form the 2-D image which can be focused on the screen. One of the advantages of this technique is the generation of electron diffraction pattern which correlates the structural properties of the image to the irradiated selected area often referred to as selected area electron diffraction (SAED) [163]. In this study, a JOEL Model No.: JEM-2100F operating at 200 kV was used to obtain the bright-field images leading to study of particle size and shapes of the powdered samples.

### **3.2.5 Optical absorption (UV-Vis-NIR) spectroscopy**

The UV-Vis-NIR spectroscopy is an optical spectroscopic technique that offers an avenue of determining the optical properties of a material either in solid or liquid phase. When light interacts with a material, there is a possibility of these processes viz: absorption, transmission, reflection and even scattering. Depending on the intrinsic properties of the material, either of them can dominate. In principle, this tool is principally designed to monitor the exponential attenuation of intensity of light as it travels through the material. Therefore, a good approximation of the dominant process is given by Lambert-Beer law (i.e.  $\partial I \propto -I\partial x$ , where  $I$  and  $x$  are intensity of the light and thickness of the sample) [164]. Basically, as seen from figure 3.8, the standard spectroscopic tool comprises of a light source made up of deuterium and tungsten, monochromator, beam splitter, sample compartment, and a detector which collects the photo-signal [165].

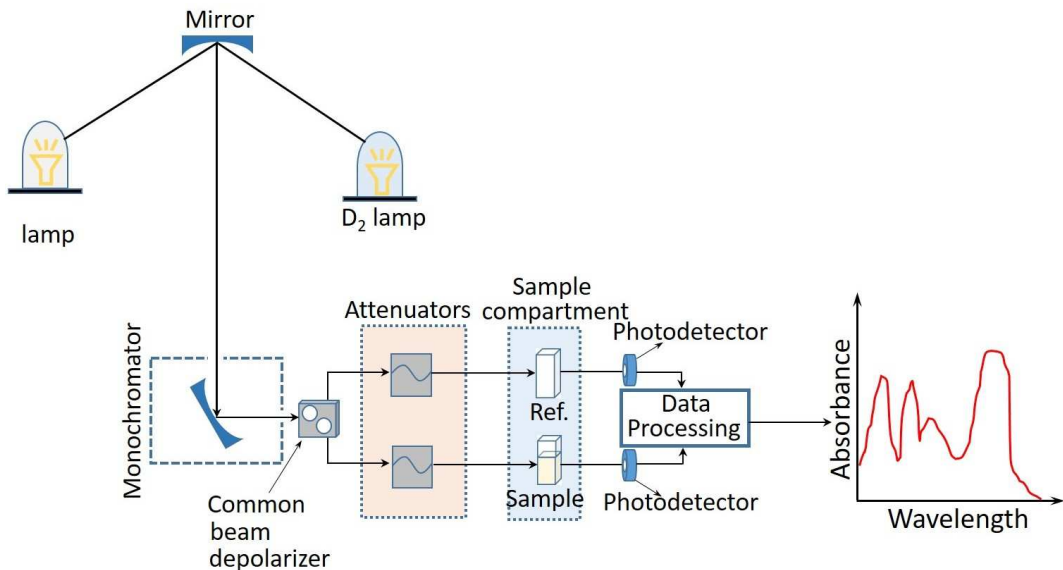


Figure 3.8: A schematic showing various components of a UV-Vis-NIR spectrometer.

For sample surfaces with high scattering, integrating sphere accessory can be incorporated to collect the diffused light. Herein, the absorbance measurements were carried out using a PerkinElmer, Lambda 750 and optical transitions of the crystalline materials are determined from the direct proportionality of absorption coefficient,  $(\alpha h\nu)^n$  and incident photon energy,  $h\nu$  of the form:  $(\alpha h\nu)^n \propto (h\nu - E_g)$ , where  $n$  is an index that depends on the optical transition of the material. For direct and indirect allowed optical transitions,  $n$  assumes a value of 2 and 1/2, respectively.



## Chapter 4

# Experimental results and discussion

In this chapter, the key results are presented section by section based on the main studies of the global project. While the journal publications yet speak for themselves, some of the extracts are re-presented to aide scientific discussion. Section 4.1 deals with the doping of pyroelectric barium titanate using transition metals (i.e. chromium, Cr and iron, Fe). The benefits and adverse effects of the mono- and co-doping on its physicochemical and photocatalytic properties are highlighted. The size effect on the photocatalytic activity of polar barium titanate particles is detailed in Section 4.2. The Landau-Ginzburg-Devonshire phenomenological model was deployed to study the structural behaviour near the phase transition especially for a system with long-range interaction that depends on size. In order to understand the mass transport mechanism at the catalyst-liquid interface and the effect of particle size, a systematic approach based on thermodynamic formalism was used. In particular, the macroscopic LGD phenomenological model was adopted to explain the size-driven phase transition observed by both XRD and Raman spectroscopy whereas the thermodynamic model, which is more suitable for particles of a few tens of atomic thickness ( $< 100$  nm) was used to explain the size-dependent heterogeneous photocatalytic kinetics. The latter takes into account additional surface energy resulting from change in chemical potential when particles become progressively small in size. Although, the L-H mechanism is always complex in terms of different processes like adsorption, desorption and/or even surface reactions taking place simultaneously, an attempt was made to draw a boundary between both models using theoretical calculations based on curve fitting, thus establishing a strong dependence of photocatalytic kinetics on structure properties.

## 4.1 Pyroelectric doped BaTiO<sub>3</sub> nanoparticles

### 4.1.1 Structural and textural properties

We begin our discussion of the fundamental physicochemical properties of these pyroelectric systems with the structure and surface morphology. The XRD patterns of the host, mono- and co-doped lattices are depicted in figure 4.1(a). There is a change in the functional properties of these systems due to a considerable amount of the dopants. All the patterns are polycrystalline; and the well-defined diffraction peaks are indexed to P4mm space group of the tetragonal phase with JCPDS card: 01-075-1606 [166]. A prevalent surface contamination of BaCO<sub>3</sub> was observed in all the patterns. The carbonate is a side reaction of barium hydroxide and probably dissolved atmospheric carbon dioxide in distilled water used in the preparation. This results to surface passivation of the crystals. In other words, the continuous growth of the lattice is impeded once the surface is passivated. Doping of inorganic AB<sub>3</sub> perovskites entails cationic substitution of either the A- or B-site. In the mono-doped systems i.e. (ii) & (iii), chromium-ion substitution may be available in different radii:  $r_{Cr^{2+}} = 0.80 \text{ \AA}$ ,  $r_{Cr^{3+}} = 0.62 \text{ \AA}$ ,  $r_{Cr^{4+}} = 0.55 \text{ \AA}$ ,  $r_{Cr^{5+}} = 0.49 \text{ \AA}$  and  $r_{Cr^{6+}} = 0.44 \text{ \AA}$  while iron ion has possibilities of  $r_{Fe^{2+}} = 0.78 \text{ \AA}$ , and  $r_{Fe^{3+}} = 0.65 \text{ \AA}$  (all the ionic radii mentioned are for the high-spin configuration) [103], it makes the B-site configuration of Cr<sup>3+</sup> and Fe<sup>3+</sup> respectively more favourable for Ti<sup>4+</sup> (0.61 Å) replacement.

Apart from the slight surface contamination which is common with the synthesis of this material, the tetragonal phase appears to be stable considering the level of concentration of dopant. In the co-doped systems i.e. (iv) & (v), the increase in the concentration of Fe ion resulted in a biphase of tetragonal and hexagonal (P63/mmc) symmetries shown by increasing intensity of the diffraction peaks at 41.4° and 53.8° [167]. The emergence of this heterophase is illustrated in figure 4.1(d) with accompanied increase in the unit cell volume as a consequence. The structural behaviour is unique with many 3d TMs such as Fe, Co etc [168]. While other impurities such as metallic Fe/Cr, Fe<sub>2</sub>O<sub>3</sub> and/or Cr<sub>2</sub>O<sub>3</sub> were not detected, the biphase existence is explained on the basis of charge compensation mechanism upon joint doping of the aliovalent metals. It is well-known that the charge compensation mechanism proceeds through the formation of oxygen vacancies  $V_O^{\bullet\bullet}$ , which in some cases reduce to singly ionized oxygen vacancies  $V_O^{\bullet}$  i.e.  $V_O^{\bullet\bullet} + e^- \longleftrightarrow V_O^{\bullet}$ . In any case, only a limited number of the defect produced from single aliovalent substitution is permitted for a corner-sharing structure

like the tetragonal phase in which the  $\text{TiO}_6$  is octahedrally coordinated with oxygen deficiency.

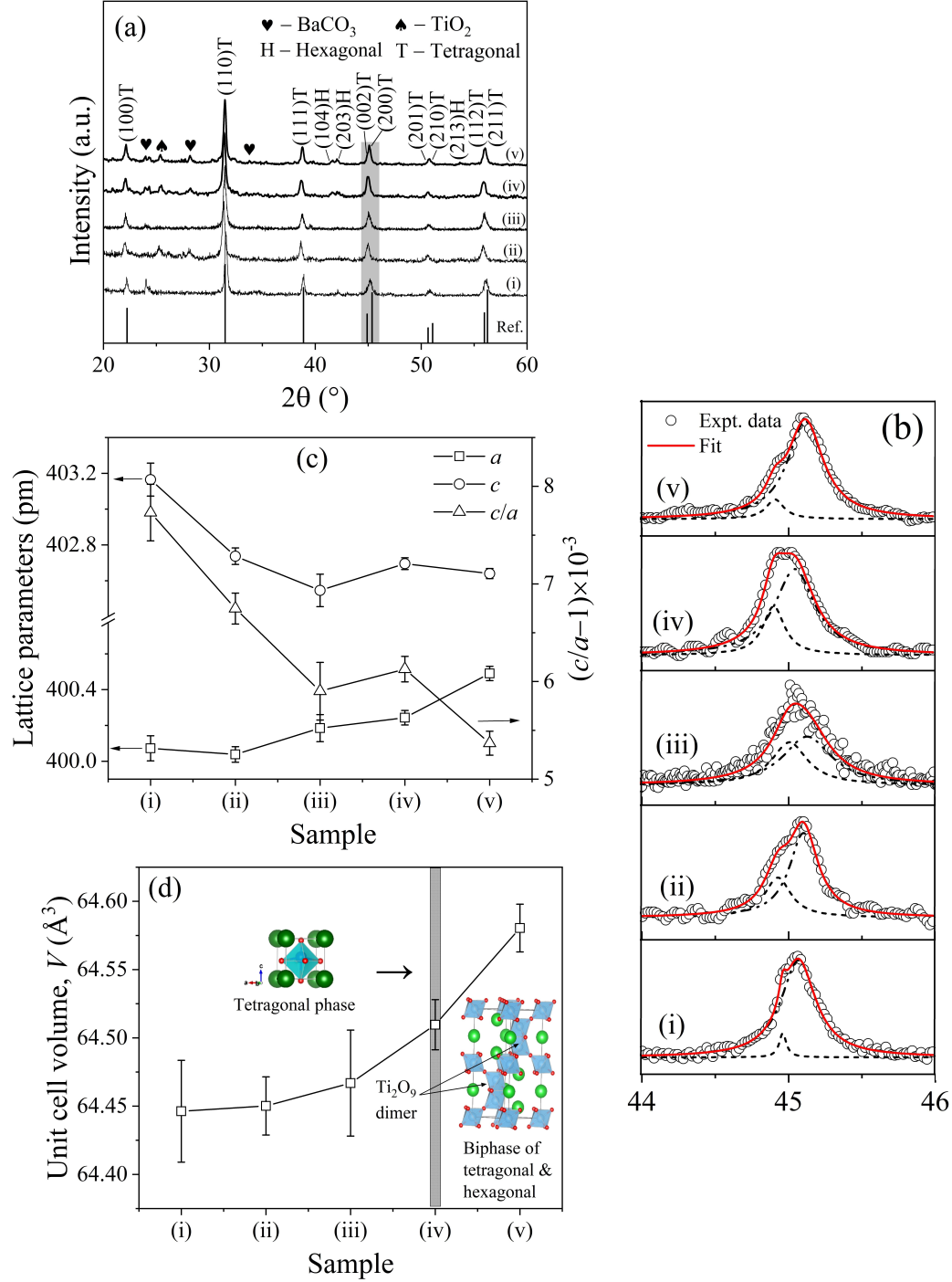


Figure 4.1: The (a) X-ray diffraction patterns of (i)  $\text{BaTiO}_3$ , (ii) 4 mol% Cr:BaTiO<sub>3</sub>, (iii) 2 mol% Fe:BaTiO, (iv) 4 mol% Fe 4 mol% Cr:BaTiO<sub>3</sub>, and (v) 8 mol% Fe 4 mol% Cr:BaTiO<sub>3</sub> pyroelectrics, (b) expanded view of (002) and (200) diffraction lines marked by the shaded portion in (a), (c) dopant dependent lattice parameters and unit cell distortion,  $(c/a - 1)$ , and (d) unit cell volume variation of the samples.

For a large number of the defects, there is a face-sharing structural rearrangement of  $\text{Ti}_2\text{O}_9$  dimer in addition to the corner-sharing to accommodate the oxygen vacancies. This gives rise to the hexagonal phase observed in the doubly TM-substituted structures.

A diffraction line profile analysis was performed to gain insight on the unit cell distortion of the nanocrystals. Thus, the region  $2\theta = 44 - 46^\circ$  was fitted with a Lorentzian line shape to estimate the Bragg angles of the two line components from which the lattice parameters  $a$  and  $c$  were determined. From the figure 4.1(b), one can observe the tetragonal peak splitting into (002) and (200) diffraction planes. The variation of lattice constants ( $a$  &  $c$ ) and deformation ( $c/a - 1$ ) of the unit cell for the samples are depicted in figure 4.1(c). As the lattice constants relax, the deformation diminishes dramatically for the doped samples with increased tendency of a structural transformation to pseudocubic. The square of spontaneous polarization is proportionally related to the deformation i.e.  $P^2 \propto (c/a - 1)$ . This implies that the deformation,  $(5.4 \pm 0.1) \times 10^{-3}$  observed for the co-doped sample with 8 mol% Fe content retains spontaneous polarization.

Further structural analysis is furnished by the Raman spectroscopy. At molecular level, the spectroscopic tool is sensitive to atomic vibrations and depends on photon-phonon interactions. The room temperature Raman spectra of the samples are shown in figure 4.2. The Raman peaks at ca.  $185 \text{ cm}^{-1}$ ,  $270 \text{ cm}^{-1}$ ,  $306 \text{ cm}^{-1}$ ,  $519 \text{ cm}^{-1}$  and  $716 \text{ cm}^{-1}$  corresponding to  $\text{A}_1(\text{TO})$ ,  $\text{A}_1(\text{TO}_2)$ ,  $\text{B}_1+\text{E}$  ( $\text{TO}_3+\text{LO}_2$ ),  $\text{A}_1(\text{TO}_3)$ , and  $\text{A}_1+\text{E}(\text{LO}_3+\text{LO}_4)$  modes are characteristics of tetragonal phase of barium titanate [166, 169, 170] generated mostly in a single phonon process. In phonon vibration of the  $\text{TiO}_6$ , the mode labeled  $\text{A}_1$  is due to bending vibration of O-Ti-O whereas  $\text{B}_1+\text{E}$  is due to a torsional vibration of Ti-O<sub>3</sub>. Other than the modes enlisted, the spectra features other phonon modes such as  $\text{E}_g$  at ca.  $144 \text{ cm}^{-1}$ ,  $\text{B}_{1g}$  at  $394 \text{ cm}^{-1}$ , and  $\text{E}_g$  at  $639 \text{ cm}^{-1}$  respectively whose attributes are those of anatase titanium dioxide [171]. This originates from a traceable amount of the residual  $\text{TiO}_2$  used as the starting material, the presence of which can be completely eliminated either by using a  $\text{Ti}^{4+}$  source with enhanced surface area in order to increase its reactivity with barium hydroxide or increasing the concentration of barium source. Moreover, an additional Raman mode,  $\text{E}_g$  due to the presence of chromium ion in 3+ oxidation state was evident at ca.  $354 \text{ cm}^{-1}$  [172]. The appearance of  $\text{B}_1+\text{E}(\text{TO})$  and  $\text{A}_1+\text{E}(\text{LO})$  modes are indication that the pyroelectric systems crystallize in tetragonal phase. However, the intensity of  $\text{B}_1+\text{E}(\text{TO})$  mode is strongly affected by the dopant concentration. The decrease in the Raman intensity shows that doping sup-

presses the tetragonality, thus corroborating the XRD result. These modes are indication of  $\text{TiO}_6$ ,  $\text{TiO}_6/\text{CrO}_6$  or  $\text{TiO}_6/\text{FeO}_6$  and  $\text{TiO}_6/\text{CrO}_6/\text{FeO}_6$  distortions and phonon propagation along the  $c$ -axis in the undoped, mono- and co-doped pyroelectrics respectively. While the dopant concentration appears to influence the spontaneous polarization as observed by the decreasing Raman intensity especially for the (v) - 8 mol% Fe 4 mol% Cr: $\text{BaTiO}_3$  sample, it is important to point out that there was no complete disappearance of spontaneous polarization even at this co-doping concentration. Further effect of the co-doping could be observed in the asymmetric Raman peak at ca.  $519 \text{ cm}^{-1}$  arising from O-Ti-O vibration.

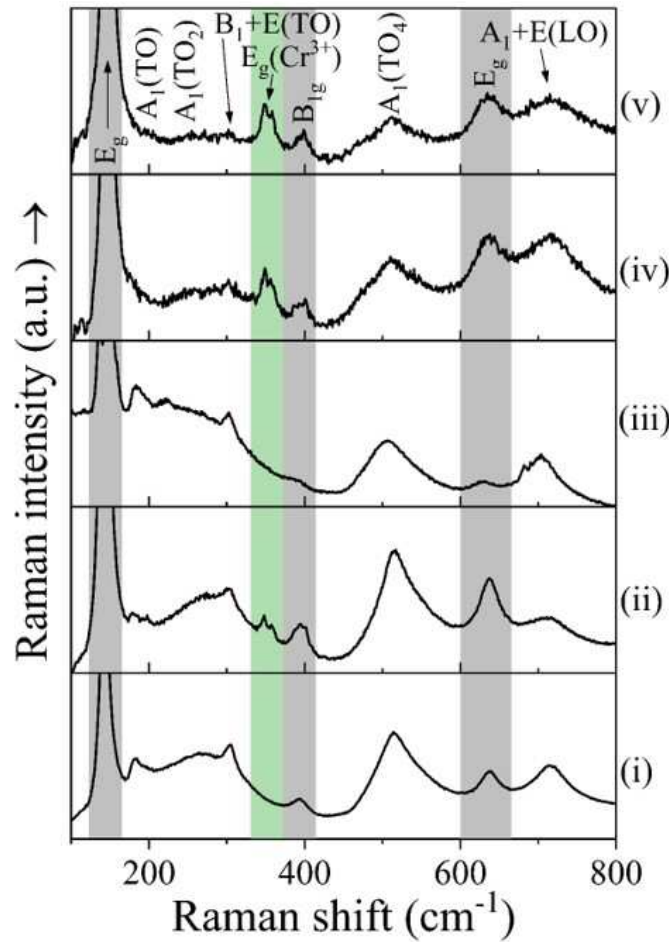


Figure 4.2: The Raman spectra of (i)  $\text{BaTiO}_3$ , (ii) 4 mol% Cr: $\text{BaTiO}_3$  (iii) 2 mol% Fe: $\text{BaTiO}_3$ , (iv) 4 mol% Fe 4 mol% Cr: $\text{BaTiO}_3$  & (v) 8 mol% Fe 4 mol% Cr: $\text{BaTiO}_3$  samples. The “gray” and “green” bars denote the Raman modes for  $\text{TiO}_2$  and Cr-O vibrations, respectively.

This leads to broadening of the Raman peak; implying a partial tetragonality of the material. In other words, the phase transition from tetragonal to cubic is not only structurally provoked by particle size and temperature but also doping concentration. In a broad perspective,

tive, doping with TMs of variable oxidation states has the tendency of crystallizing BaTiO<sub>3</sub> in the hexagonal phase [168, 173]. The hexagonal phase has Raman peaks at ca. 490 and 637 cm<sup>-1</sup> corresponding to the A<sub>1g</sub> phonon mode [174, 175]. However, the broadening of 516 cm<sup>-1</sup> peak makes the identification of 490 cm<sup>-1</sup> difficult. Also the evidence of 637 cm<sup>-1</sup> associated to titanium dioxide further complicates its identification as the Raman peak originating from titanium dioxide coincides with the Raman band of the hexagonal phase.

Taking into consideration the significance of particle size and morphological properties to catalysis, the TEM images of these samples were examined methodically. Thus, a Java image processing program, ImageJ was used to extract the particle size. Figure 4.3 and 4.4 correspond to the TEM images and particle size distribution, respectively of the samples. Irregular but spherically shaped nanograins were observed for the undoped sample. Despite the noticeable agglomeration, clusters of smaller nanocrystals were seen to populate the surface of the large grains. An average particle size of ca. 49 nm was determined for the undoped barium titanate. The chromium- and iron-doped show two distinct morphologies with the former comprising of a mixture of nanospheres and nanorods (average length and diameter of nanorods are ca. 123±7 and 62±4 nm). Besides the exposed crystal facets, the nanograins possess aspect ratio different from those of undoped and Fe-doped BaTiO<sub>3</sub>. The latter consists of mainly nanoshperes of different sizes. With almost similar particle shapes as the undoped sample, it is believed that the 2 mol% Fe content is favoured by deposition kinetics culminating to a crystallization mechanism involved in its growth. In the co-doped samples, these nanorods gradually transformed into nanocubes with the addition of Fe [see figure 4.3 - (iv)]. The pronounced suppression of the rod-like structures in (v), is an indication of strain manifesting in regions of inhomogeneously distributed defects [176].

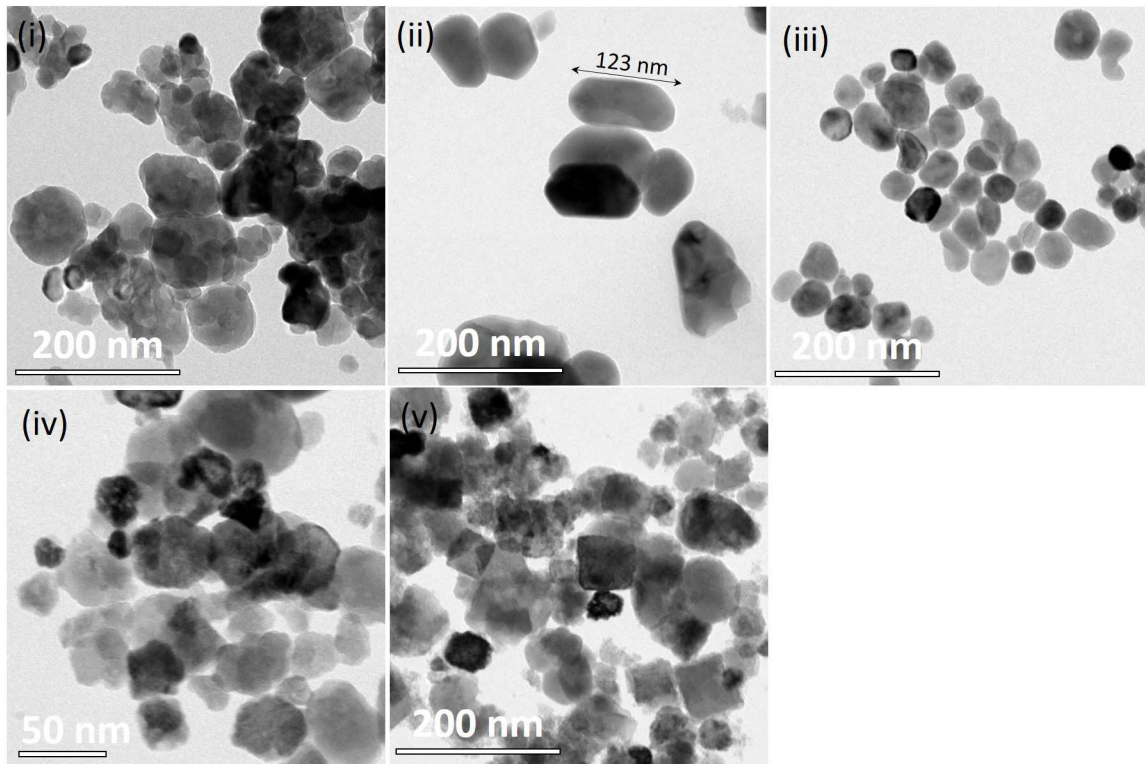


Figure 4.3: TEM images of (i)  $\text{BaTiO}_3$ , (ii) 4 mol% Cr: $\text{BaTiO}_3$  (iii) 2 mol% Fe: $\text{BaTiO}_3$ , (iv) 4 mol% Fe 4 mol% Cr: $\text{BaTiO}_3$  & (v) 8 mol% Fe 4 mol% Cr: $\text{BaTiO}_3$  samples.

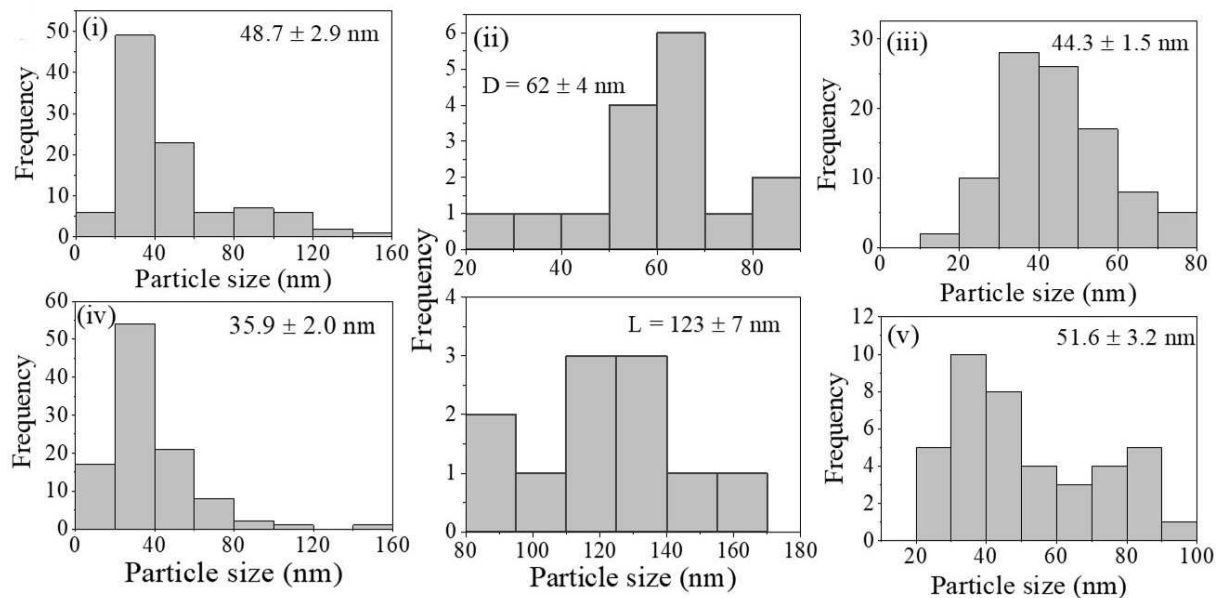


Figure 4.4: Particle size distribution of (i)  $\text{BaTiO}_3$ , (ii) 4 mol% Cr: $\text{BaTiO}_3$  (iii) 2 mol% Fe: $\text{BaTiO}_3$ , (iv) 4 mol% Fe 4 mol% Cr: $\text{BaTiO}_3$  & (v) 8 mol% Fe 4 mol% Cr: $\text{BaTiO}_3$  samples. L and D denote the length and diameter of nanorods as in the case of (ii).

### 4.1.2 Chemical composition

Furthermore, an energy dispersive X-ray (EDS) and X-ray photoelectron spectroscopy (XPS) was performed on the samples to identify the elemental composition and surface chemical states. It is known that the EDS is qualitative and has capability of providing semi-quantitative results; we therefore rely on the XPS for a good estimation of the samples' stoichiometry. The acquired EDS spectra are displayed in figure 4.5(a). Peaks related to the elements Ba, Ti, O, Cr, and Fe were observed. The presence of carbon (C) and copper (Cu) peaks are due to the carbon-coated Cu grids used in preparing samples for TEM imaging.

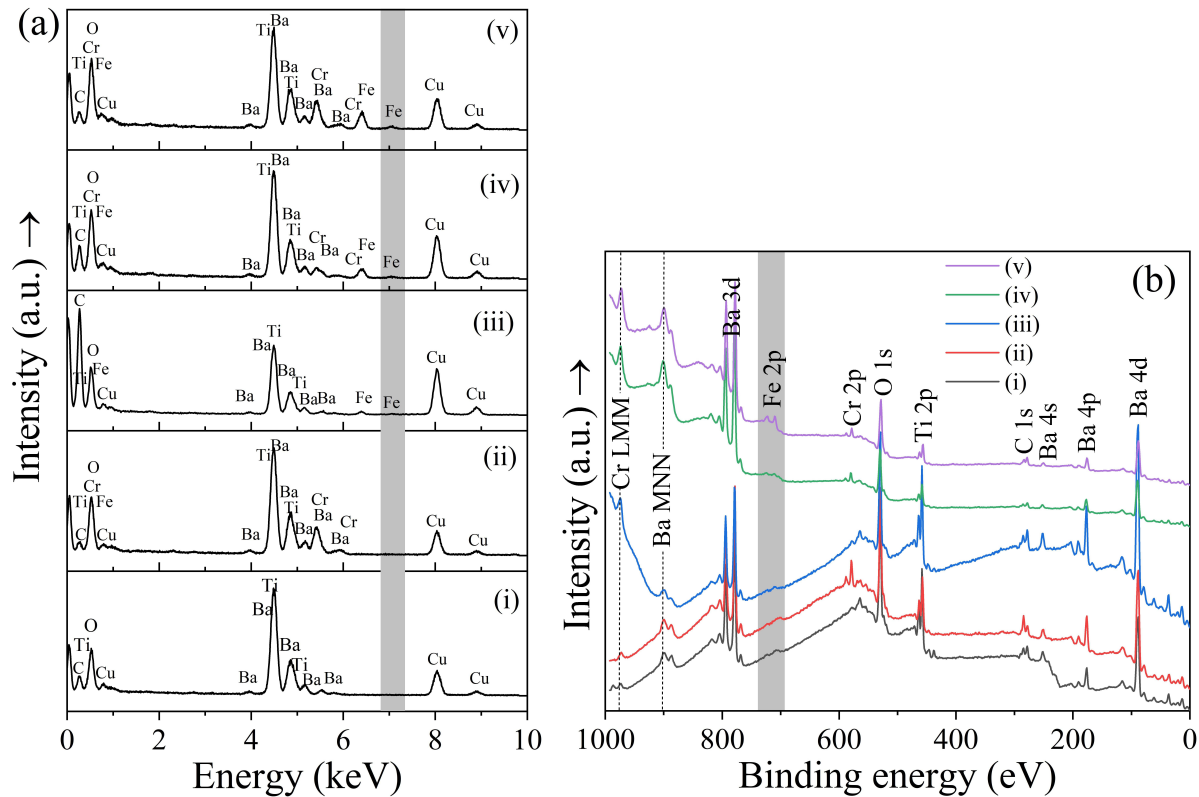


Figure 4.5: (a) Energy dispersive X-ray spectroscopy (EDS), and (b) XPS survey spectra of (i)  $\text{BaTiO}_3$ , (ii) 4 mol% Cr: $\text{BaTiO}_3$  (iii) 2 mol% Fe: $\text{BaTiO}_3$ , (iv) 4 mol% Fe 4 mol% Cr: $\text{BaTiO}_3$  & (v) 8 mol% Fe 4 mol% Cr: $\text{BaTiO}_3$  samples. Marked rectangles denote the peak intensity associated with Fe for samples containing iron.

The XPS survey-scan spectra (figure 4.5(b)) corroborate the results of EDS for all the samples. For quantification purpose, the high-resolution XPS spectra of individual element core level for all the samples are provided (figure 4.6). The lineshapes are deconvoluted using a combination of Gaussian and Lorentzian function in the ratio of 7:3 denoted as GL(30). The

most intense peak corresponding to Ba 3d core level was used to determine the oxidation state of barium. As shown in figure 4.6 between 760 eV - 800 eV, the fit components with peaks at  $778.79 \pm 0.3$  eV and  $780.49 \pm 0.2$  eV in all the samples are an indication that barium exists in oxidation state of +2. The first peak is associated to Ba atoms in the perovskite lattice whereas the second peak is related to other species bonded to Ba atom like hydroxide and/or carbonate [177]. This can be quantitatively estimated using the area from the GL(30) line fit as  $= A(Ba_{surf.}^{2+}) / (A(Ba_{lattice}^{2+}) + A(Ba_{surf.}^{2+}))$ .

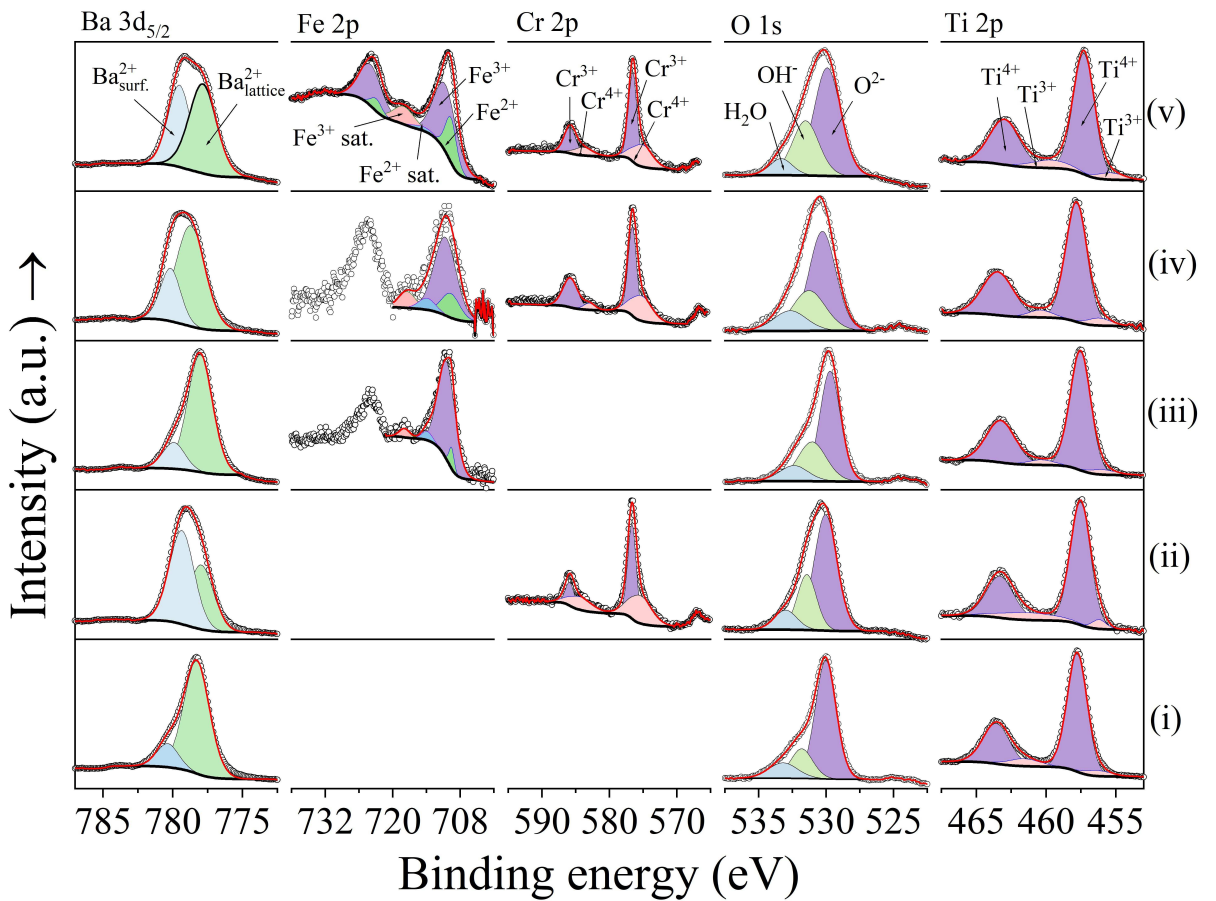


Figure 4.6: The XPS high resolution scan of Ba  $3d_{5/2}$ , Fe 2p, Cr 2p, O 1s, and Ti 2p (from left to right) for (i)  $\text{BaTiO}_3$ , (ii) 4 mol% Cr: $\text{BaTiO}_3$  (iii) 2 mol% Fe: $\text{BaTiO}_3$ , (iv) 4 mol% Fe 4 mol% Cr: $\text{BaTiO}_3$  & (v) 8 mol% Fe 4 mol% Cr: $\text{BaTiO}_3$  samples (in rows from bottom to top). Peaks labeled  $\text{H}_2\text{O}$ ,  $\text{OH}^-$  and  $\text{O}^{2-}$  denote surface adsorbed water, hydroxyl/defect oxygen, and oxygen bonded to lattice.

The values estimated are 0.15, 0.59, 0.16, 0.37, and 0.46. This confirms that the surface of the nanoparticles especially the Cr-doped  $\text{BaTiO}_3$  is passivated with non-perovskite species

namely barium carbonate. For Fe  $2p$  core levels (i.e. samples containing Fe), the Fe  $2+$  and Fe  $3+$  states are located at 709.53 eV and 710.41 eV (for Fe-doped), 709.59 eV and 710.63 eV (for 4 mol% Fe 4 mol% Cr:BaTiO<sub>3</sub>) and 709.64 eV (722.98 eV) and 710.68 eV (723.92 eV) (for 8 mol% Fe 4 mol% Cr:BaTiO<sub>3</sub>). The accompanied satellite peaks for these samples are 713.90 eV/717.89 eV, 713.92 eV/717.48 eV, and 714.64 eV/718.03 eV for the  $2+/3+$  states respectively [178, 179]. Moreover, a four-component fit was used to describe the lineshape of Cr  $2p$  core level. While the deconvolution shows that the Cr associated samples contain  $3+$  and  $4+$  states, the spin-orbit splitting for the Cr  $2p_{1/2}$  and Cr  $2p_{3/2}$  is  $9.23 \pm 0.07$  eV. The peaks located at  $576.54 \pm 0.34$  eV and  $585.82 \pm 0.07$  eV for the  $2p_{3/2}$  and  $2p_{1/2}$  are typical binding energies of Cr  $3+$  state whereas those located at  $575.16 \pm 0.33$  eV and  $583.85 \pm 0.55$  eV are characteristics of chromium in  $4+$  state [179]. The O 1s spectrum of the samples are shown in the fourth column of figure 4.6. The peak was deconvoluted into three components consisting of O<sup>2-</sup> (oxygen bonded to lattice), OH<sup>-</sup> (defective oxygen), and H<sub>2</sub>O (adsorbed moisture). All the samples have binding energy in the range  $529.71 \pm 0.57$  eV corresponding to the strong Ti-O bonds in the octahedron. The defective oxygen or hydroxyl occupying the O-site is assigned to  $531.82 \pm 0.54$  eV while surface adsorbed water molecules have characteristic binding energy at  $533.19 \pm 0.53$  eV. Finally, the core level of Ti  $2p$  lies in the range 450 - 470 eV and a multiple peak fit with four components was used to identify the chemical states of titanium in the sample. A spin-orbit splitting in the range  $5.71 \pm 0.33$  eV was observed, consistent with literature [180]. The fit result shows that both Ti  $3+$  and Ti  $4+$  states are present in Ti  $2p_{1/2}$  and Ti  $2p_{3/2}$ . The peaks located at 457.78 eV and 463.56 eV are typical binding energies of Ti  $4+$  state whereas those at 456.28 eV and 461.56 eV are binding energies of Ti  $3+$  state for the undoped sample [180, 181]. For the mono- and co-doped samples, however a slight decrease in the binding energies not higher than 0.49 eV were observed due to possible increase in Ti-O bond length. The quantitative analysis also confirmed that the amount of Ti  $3+$  state increased. This arises from charge compensation mechanism in the doped systems due to the use of aliovalent metals. Such substitution provokes the reduction of Ti  $4+$  to Ti  $3+$  usually through oxygen vacancies, thus increasing the amount of Ti  $3+$  state especially for the co-doped systems.

### 4.1.3 Optical absorption properties

Since one of the objectives of the study is to fabricate a visible-light sensitive catalyst, the optoelectronic properties were therefore investigated. The UV-Vis absorption spectra of the samples measured in the range 250 - 800 nm are shown in figure 4.7. The absorption edge of the undoped sample is located at ca. 390 nm, which corresponds to a bandgap of 3.18 eV. A good approximation of the energy bandgap was made using the relation,  $E_g = 1240/\lambda_{cut-off}$ ; where  $\lambda_{cut-off}$  is the absorption edge or cut-off wavelength already obtained by means of reasonable extrapolation on the wavelength axis.

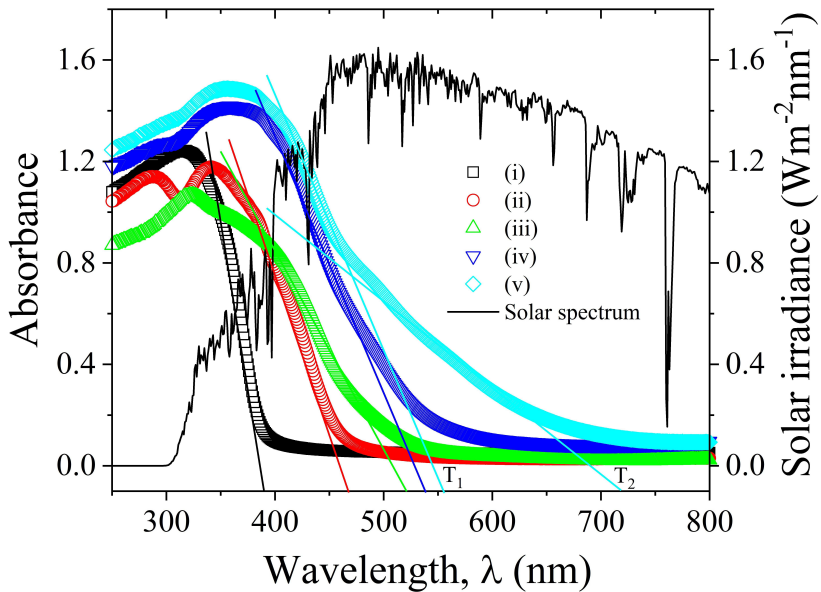


Figure 4.7: Optical absorption spectra of the as-synthesized undoped and doped photocatalysts.

As already established in Chapter 2, the optical transition mechanism in barium titanate originates from *p-d* hybridization between O 2*p* and Ti 3*d* orbitals. Judging by the estimated bandgap [105], we remark that this intrinsic property remains unchanged for the material. It was observed that the mono-doped systems show enhanced visible-light absorption due to additional absorption band which extends into the visible range, in comparison to the fundamental absorption of the undoped system. A systematic study [182] on this shows no significant red-shift of the absorption when the dopant concentration is increased beyond a certain threshold. In other words, increasing the content of chromium or iron beyond the threshold does not actually enhance the visible-light absorption properties further. This behaviour stems from

the material being potentially perceived as a degenerate semiconductor such that its carrier saturation effect appears as a consequence of interaction between dopants in excited state [183].

In a doped oxide structure like barium titanate, the concentration of oxygen vacancy increases and due to the defect band lies close to the CB, it allows easy electron exchange between the VB and CB. The additional absorption band arises therefore from the electronic charge transfer center of aliovalent atoms (Fe/Cr) or defect band ( $Fe'_{Ti}/Cr'_{Ti}$ ) and/or 3d electronic band of  $Ti^{4+}$  [24, 184]. Consequently, the multivalent nature of the TMs might induce an optical excitation of  $Cr^{3+/4+}$  or  $Fe^{2+/3+}$  exchange-coupled pair (and even both in the case of co-doped systems) resulting in more defect bands caused by high density of oxygen vacancies [185]. In this case, the light induced charge transfer process follows the reaction in Kröger-Vink notations:  $Cr^{3+} + (Ti^{4+} - V_O^\bullet) \rightarrow Cr^{4+} + (Ti^{3+} - V_O^\bullet)$  or  $Fe^{2+} + (Ti^{4+} - V_O^\bullet) \rightarrow Fe^{3+} + (Ti^{3+} - V_O^\bullet)$ ; where  $(Ti^{4+}/Ti^{3+} - V_O^\bullet)$  constitutes the defect [24]. The extra absorption further increases when the host system is co-doped with both metals. As can be seen from figure 4.7, the absorption spectrum of (v) appears to show two distinguishable transitions at  $T_1 = 2.23$  eV and  $T_2 = 1.7$  eV respectively. This may be attributed to the degeneracy of conduction band since the aliovalent co-substitution has capability of increasing the density of  $Ti^{3+}$  state as observed from XPS quantification. Hence, the concentration of these co-dopants influences this defect-induced absorption band. Overall, the effect is beneficial for visible-light activated photocatalytic application as this would potentially result to enhanced photoactivity.

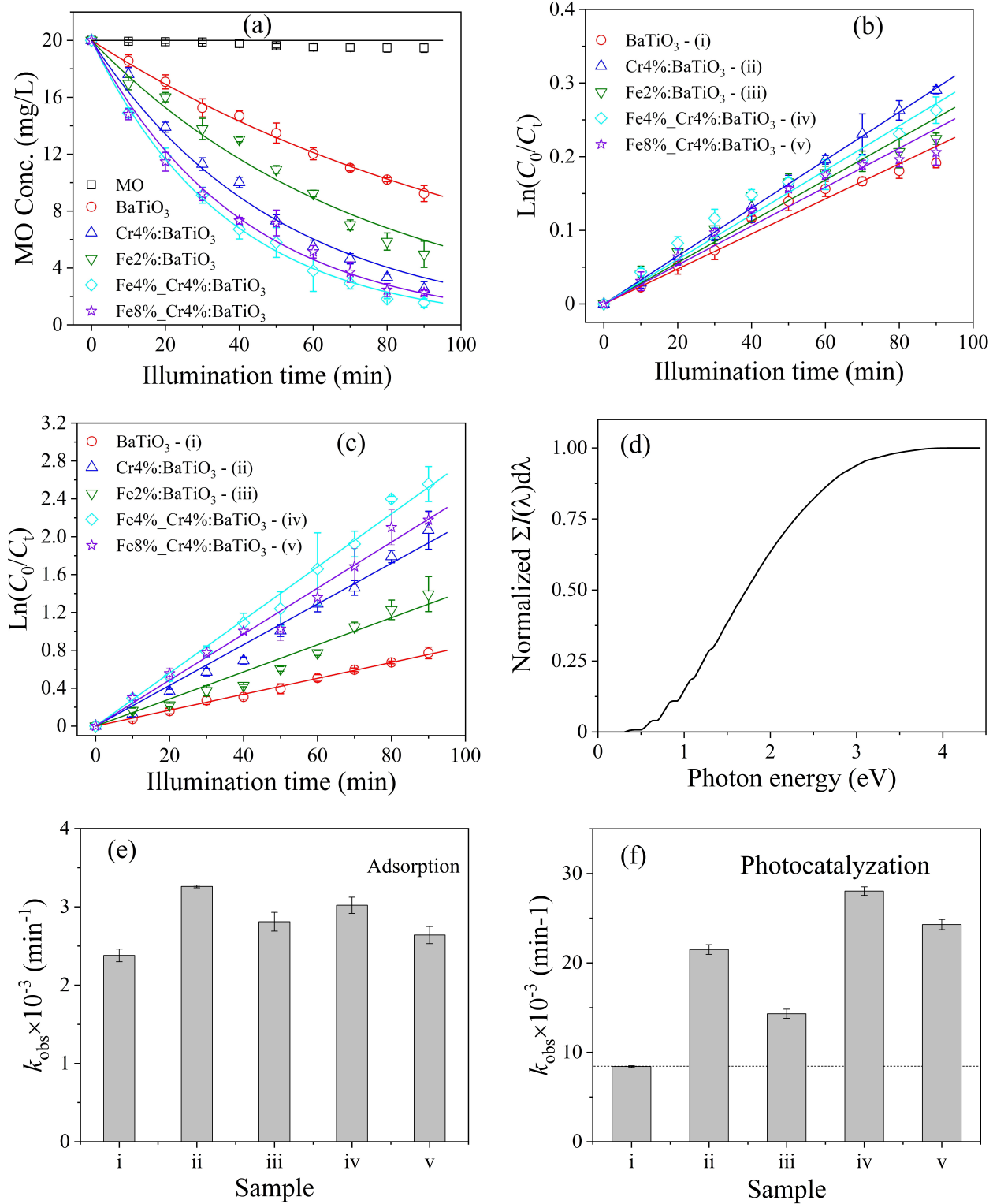
#### 4.1.4 Photocatalytic performance

The photocatalytic activity of the nanoparticles was evaluated by photodegradation of aqueous solution of methylene orange (20 mg/L) under simulated solar irradiation ( $I_{SS} = 100$  mW/cm<sup>2</sup>). Methylene orange, which its chromophore is due to the  $-N=N-$  functional group (i.e. diazenyl), is one of the most widely used synthetic dyes in textile and dyeing industry. It forms class of the toxic organic materials found in industrial wastewater. Therefore, the elimination of the toxic compound from contaminated water is necessary. The time-dependent absorption profile for degradation of this organic pollutant follows the well-known Beer-Lambert's law, thus a single exponential function was used to fit the experimental data. In addition, we discriminated the adsorption (which was evaluated as apparent reaction rate constant) and photocatalytic effects by measuring their activities in the absence and presence

of simulated solar light, respectively. The results indicate a change in the concentration of aqueous solution of methylene orange with irradiation time over the photocatalysts. While the aqueous organic pollutant suffers no meaningful photobleaching upon illumination as shown in figure 4.8(a), the effect of photochemical catalyzation due to the presence of the photocatalyst is evident. Under illumination, the photocatalytic effect becomes conspicuous as a result of photogenerated charge carriers manifesting in cascades of radicals which further degrades the species adsorbed on the photocatalyst surface. In both scenarios, the kinetic processes are irreversible and simply obey the first-order kinetics as proposed by Langmuir-Hinshelwood [28].

The apparent reaction rate constants,  $k$  obtained from the plot of  $\ln(C_0/C_t)$  vs. time,  $t$  for the samples in the dark (figure 4.8b) and upon illumination (figure 4.8(c)) are depicted in figure 4.8(e) and (f), respectively. At adsorption-desorption equilibrium, the adsorption capacity of Cr-doped BaTiO<sub>3</sub> was better compared to the other samples. This may be due to high surface area in which nanorods often possess better adsorption capacity compared to nanospheres. With respect to light-induced catalyzation, it was observed that all the doped samples exhibit a better photocatalytic activity in comparison to the undoped sample. Generally, the photodegradation rate constant is known to have a power law dependence on light intensity ( $n$ ), quantum efficiency over the wavelength range the photocatalyst absorbs ( $\emptyset$ ) and number of photon absorbed by photocatalyst ( $I_a$ ) expressed as  $k \propto (\emptyset I_a)^n$ ; and  $0.5 < n < 1$  for high and low intensities, respectively [186, 187]. Therefore, for the doped samples the term ( $\emptyset I_a$ ) is enhanced and as such enhances the photodegradation rate constant. The extent of the light absorption can be quantitatively deduced from the plot of photon energy against normalized solar irradiance integrated over all the wavelengths of the solar spectrum as shown in figure 4.8(d).

The Cr-doped BaTiO<sub>3</sub> nanoparticle was observed to have a better photocatalytic activity compared to the undoped BaTiO<sub>3</sub> counterpart. This is mainly due to enhanced light absorption. From figure 4.8(d), Cr-doped BaTiO<sub>3</sub> absorbs nearly 12.2% of the solar spectrum in contrast to the 3.9% absorbed by BaTiO<sub>3</sub> nanoparticle. This improvement in addition to the innate crystal field contributes to high photocatalytic activity observed in the Cr-doped BaTiO<sub>3</sub> sample. Moreover, the substantial surface area would promote adsorption of oxygen-containing species which aide in the degradation of intermediate products, and this translates to an enhanced photocatalytic reaction [188, 189].



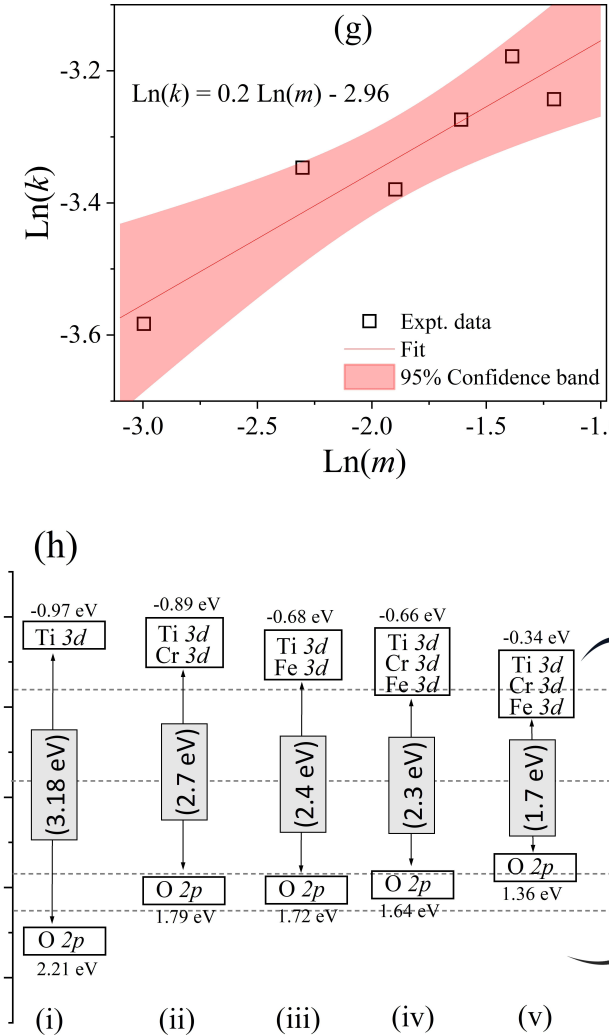


Figure 4.8: The time-dependent (a) photodegradation of MO over as-synthesized pyroelectric samples, (b) kinetics for adsorption (c) kinetics for photodegradation, (d) the plot of photon energy against normalized spectral irradiance integrated over all the wavelengths of the solar spectrum. Bar charts show reaction rate constants obtained for the (e) adsorption, and (f) photochemical catalyzation, respectively. The solid lines depict exponential (a) and linear (b and c) fits to data. (g) The variation of reaction rate constant with catalyst mass in order to determine the catalyst loading for 4 mol% Fe 4 mol% Cr:BaTiO<sub>3</sub> nanoparticle. (h) The schematic band structures of the samples.

We would like to mention at this point that our chromium doped sample outperformed those of Srilakshmi et al. [36] which yields  $\sim 63.4\%$  when recalculated to 90 min, although it was used for reduction of nitrobenzene to aniline. To further exploit the advantage of light harvest, we co-doped BaTiO<sub>3</sub> lattice with iron and chromium. The molar composi-

tion ratios of iron and chromium are 1:1 and 2:1 for 4 mol% Fe 4 mol% Cr:BaTiO<sub>3</sub> and 8 mol% Fe 4 mol% Cr:BaTiO<sub>3</sub> nanoparticles, respectively. It was observed that the use of the two transition metal dopants further enhances the performance due to extended photo-absorption. For instance, the 4 mol% Fe 4 mol% Cr:BaTiO<sub>3</sub> and 8 mol% Fe 4 mol% Cr:BaTiO<sub>3</sub> nanoparticles absorb about  $\sim 24.5\%$  and  $51.1\%$ , respectively of the solar spectrum. However, the adverse effect of the co-doping kicks in immediately the Fe content was raised above 4 mol%. This implies that despite the extending advantage of light absorption, the material's bulk property which is supposed to provide efficient charge carrier separation leading to improved surface reactivity becomes compromised. It is worth noting that in this kind of chemical kinetics, the overall rate-determining step is how efficient the charge transport process from the bulk where the charge carriers are generated to the surface where the redox reaction takes place. Therefore, the extra Fe content might have possibly reduced the number of surface active sites, culminating to recombination centers which eventually limits the global charge-consuming catalysis [27]. With a degradation rate constant of ca.  $(28.0 \pm 0.5) \times 10^{-3} \text{ min}^{-1}$ , the 4 mol% Fe 4 mol% Cr:BaTiO<sub>3</sub> nanoparticle is 3.3 and 1.3 times more efficient compared to the pristine and Cr-doped BaTiO<sub>3</sub> counterpart, respectively. Despite the high photocatalytic performance, however the use of chromium is unjustified as it is considered a heavy metal and toxic especially in the hexavalent state. To circumvent this, we further doped the host lattice with iron (Fe) only as it is non-problematic in any valence state. The light absorption capacity was  $\sim 21\%$ , implying that doping with iron extends the absorption band further into the visible region compared to doping with chromium. Interestingly, from the kinetic traces of the photodegradation, we determined a degradation rate constant of  $(14.3 \pm 0.5) \times 10^{-3} \text{ min}^{-1}$ , which is 1.7 times better than the undoped BaTiO<sub>3</sub> nanoparticle. Although the light utilization is beneficial to photocatalysis, it suffices to state unarguably that its intricate coexistence with the bulk property, bulk photovoltaic effect furnished by the crystal's broken-inversion symmetry provides the synergy required for charge carrier separation and transport.

Under identical experimental conditions, the photocatalyst loading experiment was also carried out and presented here as a variation of  $\ln(k)$  with  $\ln(m)$  (see figure 4.8(g)). A linear relationship,  $\ln(k) = 0.2\ln(m) - 2.96$  is found to exist between  $\ln(k)$  and  $\ln(m)$ . Beyond photocatalyst loading of 0.15 g/L the reaction rate constant is observed to saturate, implying an optimum dosage at this concentration. It is believed that the hydroxylation of TiO<sub>2</sub>-terminated surface resulting from high concentration of oxygen retards the adsorption

of methylene orange at the active sites [190]. This potentially may give rise to a terminal reaction suggesting why the reaction rate constant saturates.

To deepen our understanding on the photocatalytic process, a band structure for each of the perovskite samples was constructed by deducing the associated band potentials (figure 4.8(h)). Hence, the conduction ( $V_{CB}$ ) and valence ( $V_{VB}$ ) band potentials are calculated based on equation 2.4.  $E_g$  is the apparent energy bandgap of the doped samples determined via UV-Vis-NIR spectroscopy. The electronegativity of individual samples was determined using a geometric mean electronegativity of the individual elements composing the sample whereas the molar ratio was obtained from percentage atomic quantification carried out by XPS fitting of the elemental core levels associated with the sample. Notably, the non-perovskite oxygen was not taken into account when determining the molar ratio. A detailed calculation to estimate these parameters can be found in Section A.2 of Appendix A. Although the calculation is empirical as it takes only the electronegativity into consideration, one can see that the conduction band potential for all the samples is more negative in comparison to the redox potential of  $V^0(O_2/O_2^{*-}) = -0.16$  eV (see figure 4.8(h)). The implication is that there will be heterogeneous reduction of dissolved oxygen by the photo-excited electrons which occupy the conduction band. With subsequent formation of superoxide,  $O_2^{*-}$  radicals which the end reaction is  $OH^\cdot$  following a direct protonation of the former, catalyzation of the adsorbed species of pollutant can proceed. However, the valence band potentials obtained are less positive compared to the redox potential of  $H_2O/OH^\cdot$ . The consequence is that the direct oxidation of  $OH^\cdot$  from  $h^++OH^-$  may be unlikely as it is at a lower potential energy. Intriguingly, the calculated valence band potentials are more positive than the  $H_2O_2/OH^\cdot$  redox couple whose potential energy is  $V^0(H_2O_2/OH^\cdot) = 0.89$  eV [191], suggesting that  $OH^\cdot$  radicals can also be formed from the decomposition of hydrogen peroxide. In other words, indirect oxidation through this approach is potentially capable of enhancing the degradation process [42].

#### 4.1.5 Summary of pyroelectric undoped and doped $BaTiO_3$ systems

We have successfully synthesized photo-pyroelectric barium titanate systems through a dedicated microwave-assisted hydrothermal approach. The synthetic route is reproducible and above all, scalable. The doped systems exhibit extended absorption bands, which is beneficial

to photocatalysis in terms of visible-light harvest. The photocatalytic performance evaluated through time-dependent absorption studies of methylene orange demonstrates a substantially enhanced photocatalytic performance in comparison to the undoped system. From this study, we showed that in terms of photo-absorption, doping with chromium is good although doping with iron offered better spectral photoresponse. While the highest photocatalytic performance was obtained with the optimum doping level of equiproportional composition of chromium and iron. The photocatalytic performance was explained in terms of extra light harvest and utilization, effect of Fe content, and tetragonality which is an indirect assessment of the bulk property responsible for the charge carrier separation.

## 4.2 Size effects on the photocatalytic kinetics of polar BaTiO<sub>3</sub> particles: Thermodynamic and LGD phenomenological approaches

### 4.2.1 Textural properties

TEM was used to examine the textural properties of the particles and the representative TEM images are shown in figure 4.9(a) – (g).

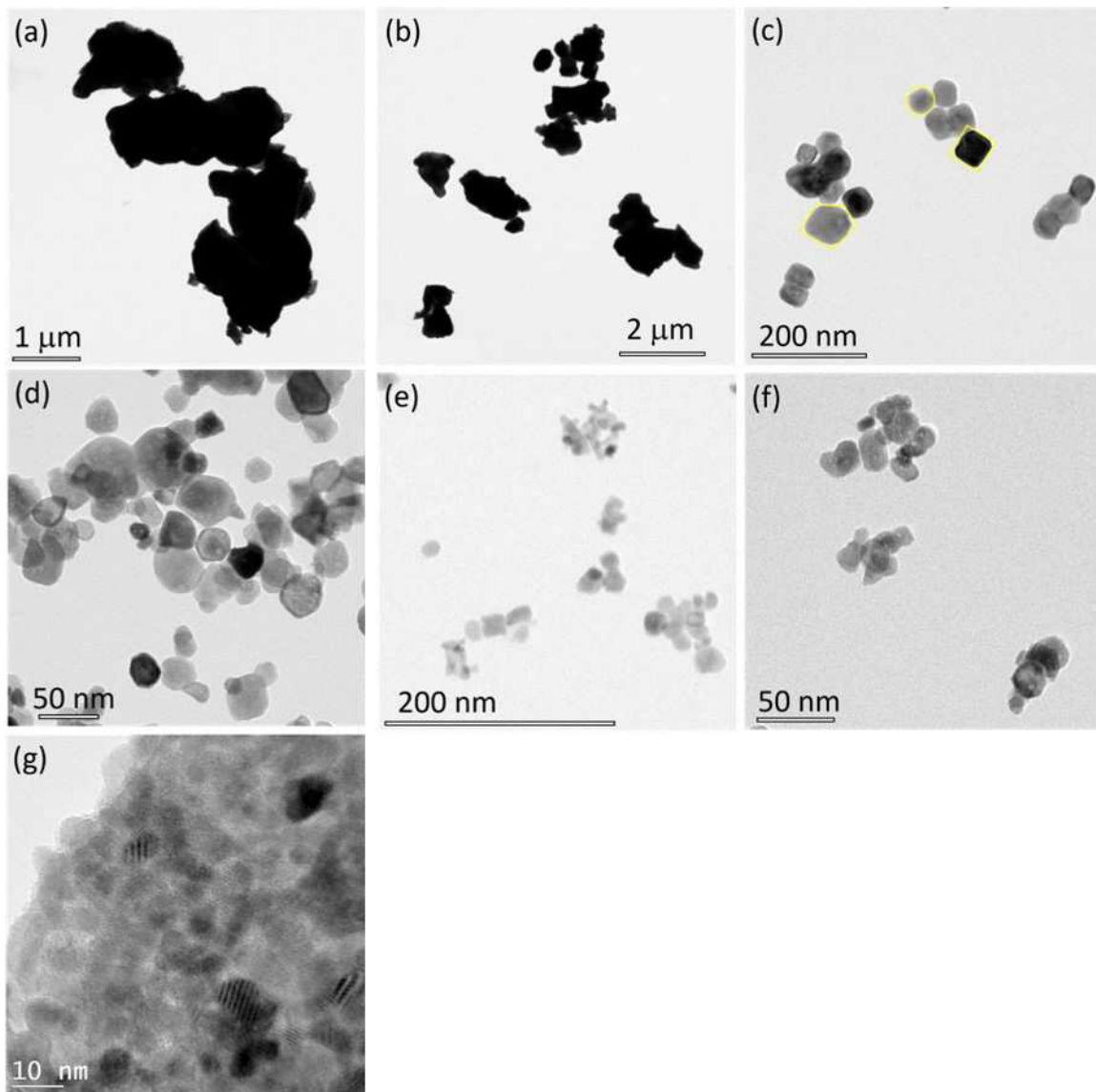


Figure 4.9: TEM images of (a) 3  $\mu\text{m}$ , (b) 2  $\mu\text{m}$ , (c) 100 nm, (d) 50 nm, (e) 26 nm, (f) 19 nm, and (g) 9 nm barium titanate particles.

The average particle sizes as considered here are typical diameters of the nearly spherical particles observed in the images. The size distributions of the particles are displayed in figure 4.10(a) – (g) and are observed to be wide with standard deviations not more than  $\sim 19\%$  of the average size.

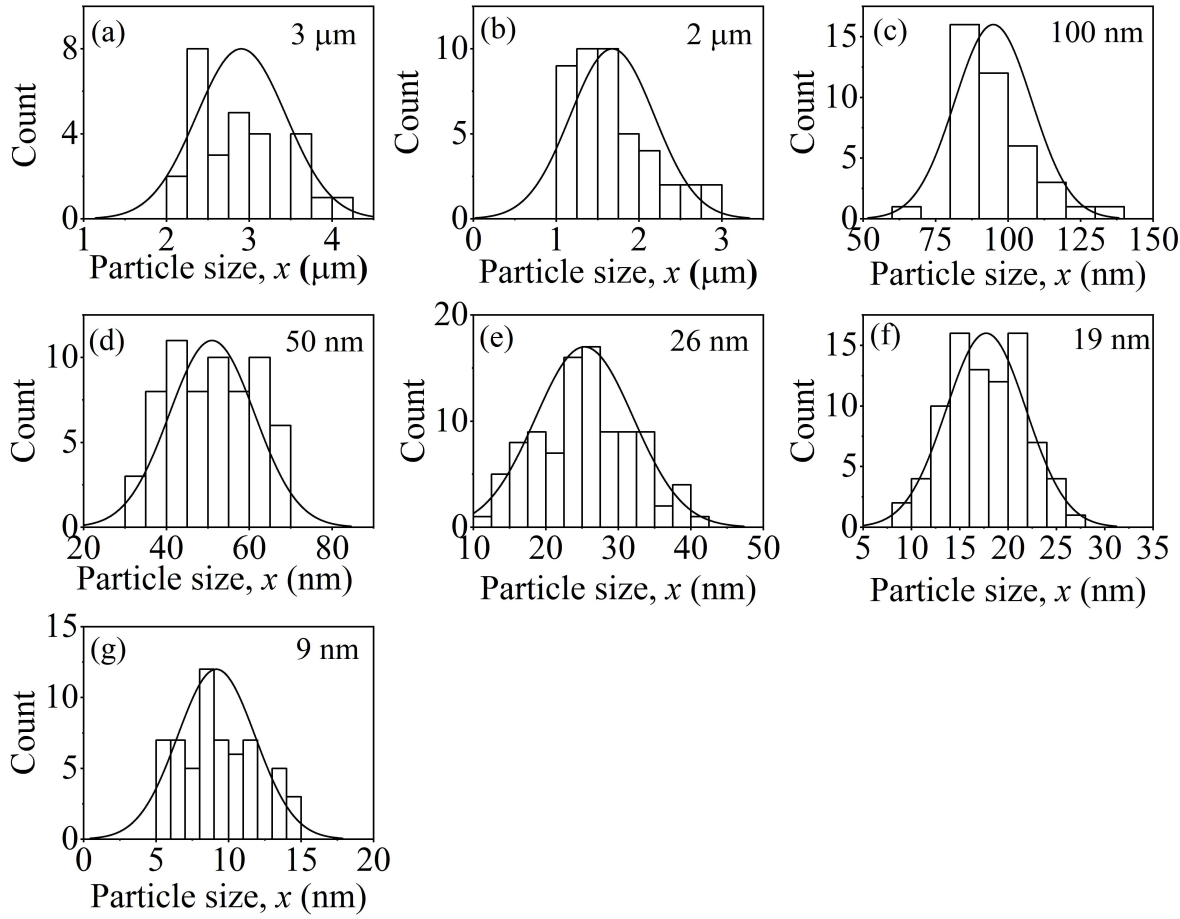


Figure 4.10: The particle size distribution of (a) 3  $\mu\text{m}$ , (b) 2  $\mu\text{m}$ , (c) 100 nm, (d) 50 nm, (e) 26 nm, (f) 19 nm, and (g) 9 nm barium titanate particles.

The lateral resolution of the images are also different due to size constraint as large particles are known to be less transparent to electron beam. The morphology of the 2  $\mu\text{m}$  and 3  $\mu\text{m}$  particles are mainly non-spherical and agglomerates. For the nanostructure of 100 nm powder, it is composed of quadrilaterals and spherical geometries with size distribution in the range of  $96 \pm 10$  nm. Similar nanostructures that are slightly dispersed were observed in the images of 19 to 50 nm particles. However, the morphology of 9 nm powder was different and consists of clusters that are highly aggregated. This makes it fairly difficult in analyzing the size distribution due to indistinct boundaries of clustered particles.

#### 4.2.2 Microstructural properties (Size effect on tetragonality, $c/a$ ratio and Curie temperature, $T_C$ )

X-ray diffraction technique was employed to analyze the structural properties of these particles. Figure 4.11(a) shows the diffraction patterns of the varying sizes of BaTiO<sub>3</sub> particles measured in the range  $20 \leq 2\theta \leq 70^\circ$ . Apart from the 9 nm sized BaTiO<sub>3</sub> which crystallized in cubic phase, the other samples crystallized in the tetragonal phase at room temperature. The patterns were matched with the reference cubic and tetragonal phase corresponding to the JCPDS card #: 01-075-0213 and 01-089-1428, respectively [132, 170]. Comparing with the XRD of Section 4.1.1 where peaks related to TiO<sub>2</sub> were evident, no diffraction peak corresponding to residual TiO<sub>2</sub> was observed indicating a complete reaction of the starting precursors. This shows that the TiO<sub>2</sub> obtained using Ti-alkoxide has high surface area. Diffraction peak corresponding to the surface contamination of CO<sub>3</sub><sup>2-</sup> ion coexists with both phases of barium titanate for the particle sizes  $x < 100$  nm. Being susceptible to atmospheric CO<sub>2</sub>, this byproduct results from chemisorption since it is thermodynamically stable in aqueous solution of high pH in comparison to the desired titanate product [192, 193]. Although the single-step-reaction synthetic route has been credited for its reliability in producing high-purity and ultrafine particles of BaTiO<sub>3</sub>, the secondary phase appears to be a common contamination and it is inevitable to some extent [192].

Contrary to reports on the absence of the contamination, it could be the concentration was below the detection limit of XRD considered to be 5% [194]. However, in powdered samples such as this, and in particular those of particle sizes,  $x < 100$  nm where the carbonate peak is undeniable suggest that a considerable amount is present. While barium titanate could be considered as an alternating stack of BaO and TiO<sub>2</sub> with the former exhibiting low photocatalytic activity [195], the implication is that the thermally stable carbonate layer passivates the barium titanate structure thereby lowering the contribution of the BaO-terminated surface to photodegradation.

Furthermore, the phase can also be distinguished on the qualitative account of diffraction line profile analysis at  $2\theta = 45^\circ$  (figure 4.11(b)). The micron-sized particles show a clear peak splitting into (002) and (200) indicating the tetragonal phase as mentioned before whereas the line profile broadening due to small crystals composed of the 19 - 100 nm particles makes this phase difficult to be identified. In any case, a two-Lorentzian component was used to

fit the profiles of 19 - 100 nm particles while a single Lorentzian function was used for 9 nm powder. The latter shows a good fit with correlation coefficient of  $R^2 \sim 0.94$ , confirming the dominance of the cubic phase in the powder. The lattice parameters,  $a$  and  $c$  were then determined through cell refinements and the results including the ratio i.e.  $c/a$  are presented in figure 4.11(c) and (d). The estimated error in  $c/a$  ratio (also termed tetragonality) denoted as  $\Delta c/a$  conforms to those determined through equation 4.1

$$\Delta \left( \frac{c}{a} \right) = d \left( \frac{\sin\theta_2}{\sin\theta_1} \right) \approx \frac{\cos\theta_1}{2\sin\theta_1} d(\Delta 2\theta) \approx 1.2 \times d(\Delta 2\theta) \quad (4.1)$$

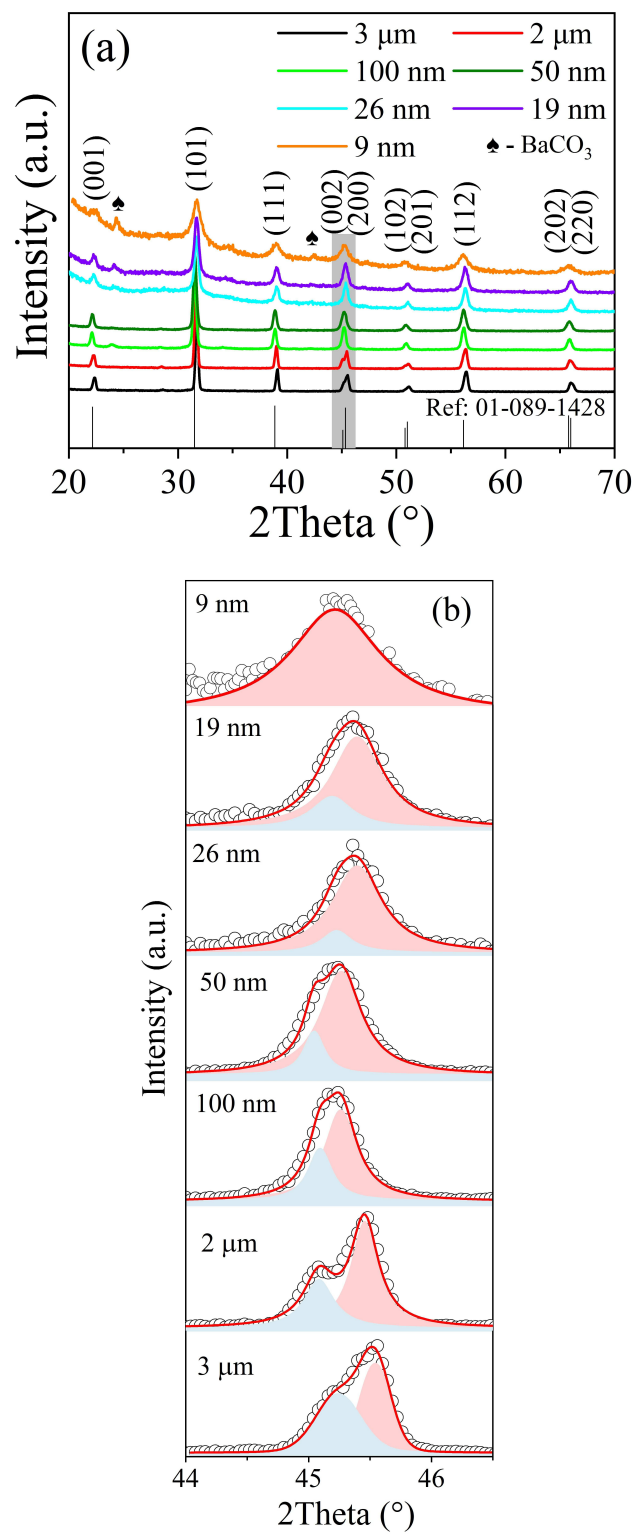
where the diffraction peaks corresponding to (002) and (200) planes are  $\theta_1$  and  $\theta_2$ , and  $\Delta 2\theta$  is  $2(\theta_2 - \theta_1)$  [137]. It was observed the  $c$ -axis decreases whereas  $a$ -axis increases as the particle size decreases. Wittels and Sherrill [196] has shown that the  $a$ -axis can increase up to 4.0825 Å, however such expansion was not observed for these particles. The 9 nm powder may be pseudocubic as the unit cell distortion,  $c/a - 1 \simeq 0.00011$  is considerably small. A sharp decline in tetragonality was noticed between 19 - 100 nm, which suddenly approaches unity when it is below a finite size. This is termed the critical size depicting the superparaelectric limit when the net dipole moment approaches zero [197]. By defining the relationship between tetragonality  $c/a$  ratio and particle size  $x$  as given in the empirical relation [139]

$$\left( \frac{c}{a} \right)_x = \left( \frac{c}{a} \right)_\infty \left[ 1 - \frac{A}{x - x_0} \right] \quad (4.2)$$

where  $\left( \frac{c}{a} \right)_x$  is the tetragonality for a ultrafine particles of varying sizes,  $\left( \frac{c}{a} \right)_\infty$  is the tetragonality for the bulk powder,  $x_0$  is the critical size, and  $A$  is a fitting parameter which the dimension is similar to particle size but has no specific physical meaning, a critical size of  $\sim 8.5 \pm 3$  nm was obtained and this compares well with what has been reported in the literature [198, 199].

A deeper analysis of the structural properties is provided by Raman spectroscopy. It is well-known that the behaviour of polar materials near the phase transition can be described by the dynamics of its phonon vibrations [198]. Therefore, as the particle size is reduced, a size-driven phase transition occurs and equivalent to it, a dramatic reduction in Curie temperature, otherwise the temperature-driven phase transition. Therefore, the temperature dependence of Raman spectroscopy makes it possible to determine the transition/Curie temperature,  $T_C$  of

these particles.



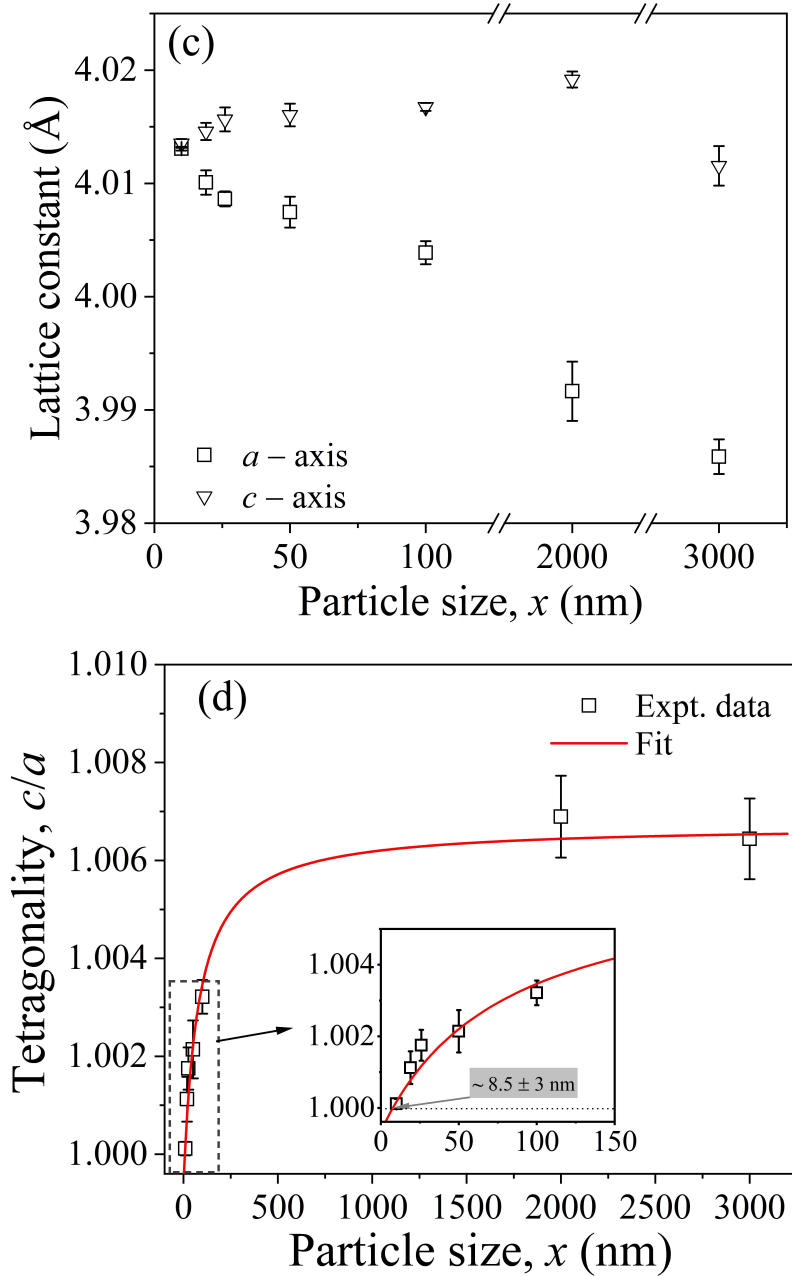


Figure 4.11: (a) The XRD pattern of the different sizes of barium titanate particles; (b) The expended view of line profile at  $45^\circ$ . The red solid line is the fit to experimental data; The size-dependent (c) lattice parameters,  $a$ -axis and  $c$ -axis, and (d) tetragonality,  $c/a$  ratio. Inset of (d) is the expanded view of  $c/a$  ratio in the range, 0 - 150 nm.

The Raman spectra acquired for the different sizes of  $\text{BaTiO}_3$  particles as a function of temperature are shown in figure B.1 of Appendix B while those acquired at room temperature are shown in figure 4.12. The spectra show some features that are different from those presented in figure 4.2 of Section 4.1.1. The Raman peaks were compared with the reference spectra

of tetragonal phase  $\text{BaTiO}_3$  [166, 169, 200] followed by the assignment of the phonon modes. It was observed that the phonon modes,  $E_g$  at ca.  $144 \text{ cm}^{-1}$ ,  $B_{1g}$  at ca.  $394 \text{ cm}^{-1}$ , and  $E_g$  at ca.  $639 \text{ cm}^{-1}$  whose features are those of anatase titanium dioxide [171] were absent. Interestingly, this indicates that there was a complete reaction of the titanium dioxide prepared using titanium alkoxide. The presence of the Raman mode around  $1063 \text{ cm}^{-1}$  confirms that  $\text{BaCO}_3$  was present in a detectable amount [166]. Its intensity was pronounced especially for the nanoscale  $\text{BaTiO}_3$  particles and appears to increase with decreasing particle size.

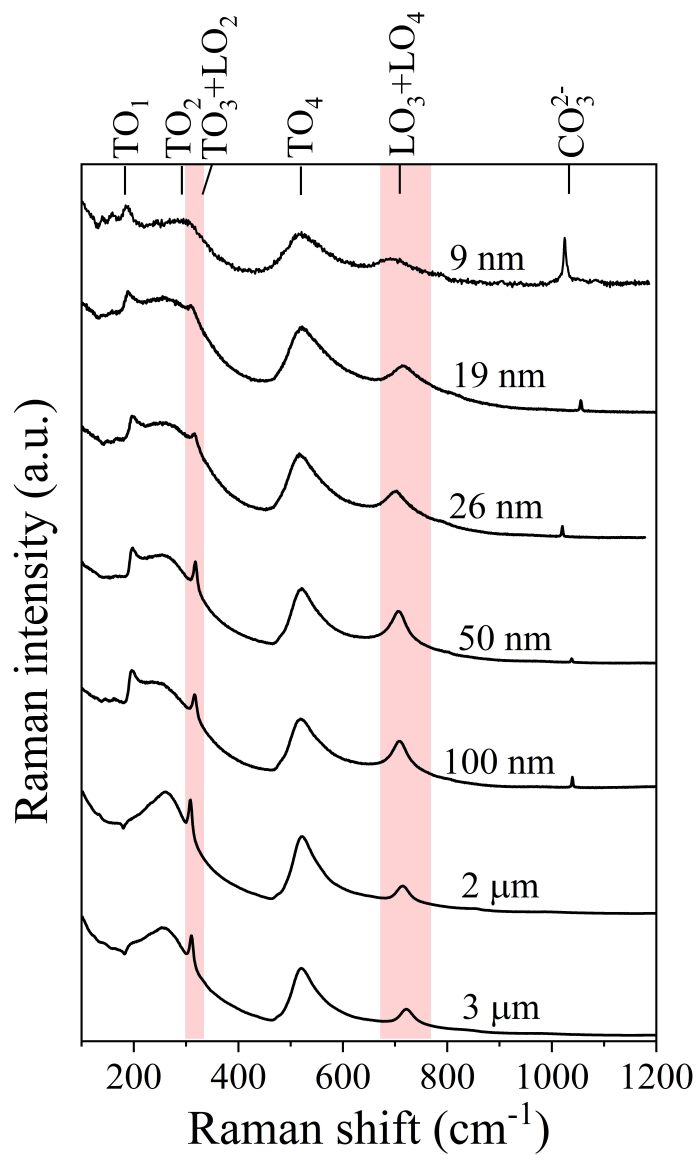


Figure 4.12: The Raman spectra of the different sizes of  $\text{BaTiO}_3$  particles acquired at room temperature.

For instance, the Raman intensity of BaCO<sub>3</sub> in the 9 nm powder is nearly 3 times that of the 19 nm powder. This secondary phase can either be formed in the bulk, in which case the growth kinetics will be somewhat similar to the formation of BaTiO<sub>3</sub> and the height of the Raman intensity will be the same regardless of particle size of the particles or on the surface, in which case the reduction in particle size favours the increase in thickness of BaCO<sub>3</sub> layer, and thus an increased Raman intensity.

As previously mentioned in Section 4.1.1, the first-order Raman signature of the cubic phase is prohibited by symmetry; therefore the Raman response of the 9 nm powder is an indication of a residual tetragonal distortion i.e. not entirely cubic. This is in contrast to the XRD studies indicating a high sensitivity for tetragonalnity using Raman spectroscopy compared to XRD. In a broad sense, the lines at ca. 180 cm<sup>-1</sup>, 270 cm<sup>-1</sup>, 306 cm<sup>-1</sup>, 519 cm<sup>-1</sup> and 716 cm<sup>-1</sup> correspond to TO<sub>1</sub> mode of A<sub>1</sub> symmetry, TO<sub>2</sub> modes of A<sub>1</sub> symmetry, (TO<sub>3</sub>+LO<sub>2</sub>) mode of B<sub>1</sub>+E symmetry, TO<sub>3</sub> mode of A<sub>1</sub> symmetry and (LO<sub>3</sub>+LO<sub>4</sub>) mode of A<sub>1</sub>+E mode, respectively. While the line at ca. 180 cm<sup>-1</sup> appears as a peak for the nanoscale particles, it can be seen as a dip for the bulk (2 μm and 3 μm) particles. This is a consequence of anharmonic coupling and decoupling induced by softening of transverse optic phonons of the A<sub>1</sub> symmetry, which is absent in the bulk samples [201]. The asymmetric peaks at 270 cm<sup>-1</sup>, and 519 cm<sup>-1</sup> are second order (two-phonon) feature and become more broadened as the particle sizes decrease. Also, the B<sub>1</sub>+E mode is more affected as the intensity nearly smeared out for the 19 nm powder. The B<sub>1</sub>+E and A<sub>1</sub>+E symmetries are optic modes associated with ferroelectricity and as such their intensities are monitored in order to predict the  $T_C$ . Figure 4.13(a) shows the plot of normalized Raman intensity vs. temperature of the particles for which a model based on power law was used to fit the experimental data. From the fit, the  $T_C$  is taken as the intersection of the fit line with the temperature axis. The Curie temperature determined for the 2 μm and 3 μm particles is about 128±6 °C and 129±3 °C, which is close to the value (130 °C [133, 202]) reported for a bulk crystal. As expected, the  $T_C$  decrease with the particle size (figure 4.13(b)).

To predict the critical particle size of these particles, we use equation 2.15, where  $T_C(x)$  is the Curie temperature of ultrafine particles of varying sizes and  $T_C(\infty)$  is the Curie temperature for the bulk powder. The constant  $B$  is a fitting parameter. From the fit, a critical particle size of 11.5±2 nm was obtained at room temperature, 25 °C and this is in excellent agreement with the report of Zhao et al [203]. This is the physical size which electric dipoles

in the powder may be sustained. The finite size seems plausible as it corroborates the results of XRD and Raman showing a  $c/a$  ratio near unity and condensation of  $(\text{TO}_3 + \text{LO}_2)$  to  $\text{TO}_2$  phonon mode, respectively for the smallest particle size. Since structural instability sets in immediately at this size, a further increase in the temperature forces the transition into the high symmetry cubic phase.

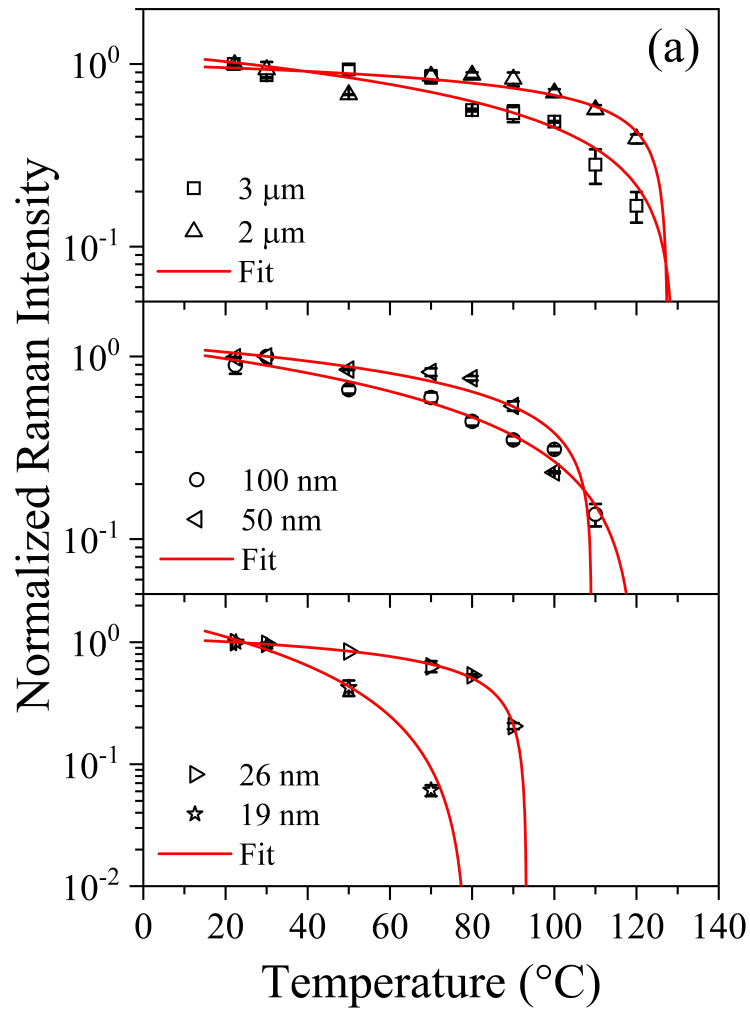


Figure 4.13: (a) The temperature dependence of normalized Raman intensity of  $\text{B}_1 + \text{E}$  symmetry.

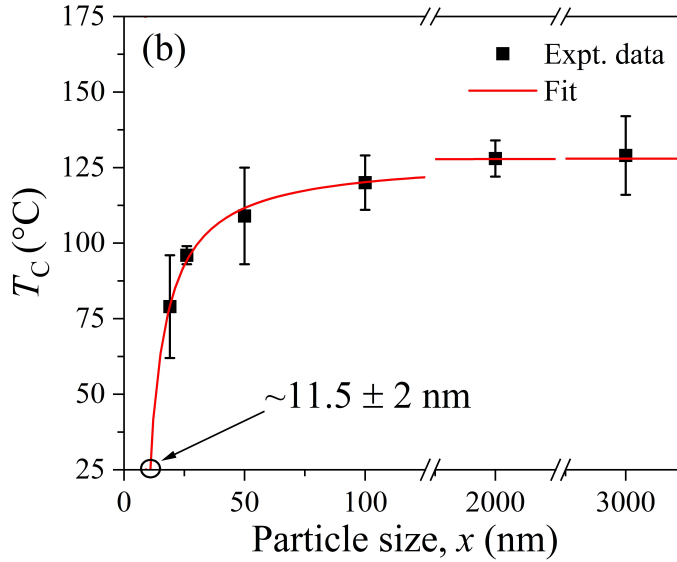


Figure 4.13: (b) The variation of estimated  $T_C$  versus particle size.

#### 4.2.3 Optical absorption properties (size effect on energy bandgap, $E_g$ )

In addition, the optical absorption study was investigated and presented here as energy bandgap (figure 4.14(a) - (d)). Notably, barium titanate exhibits both direct and indirect transition, and the optical excitation is typically a charge carrier transfer between the O 2p and Ti 3d states resulting from the behaviour of Ba-O and Ti-O bonds [204]. From the plots in the case of indirect band transition, the energy bandgap was extrapolated at  $\alpha^{1/2} = 0$  within an error margin of 10 meV. The micron-sized particles have energy bandgap of about  $\sim 3.3$  eV, which is comparable to what has been reported in literature [205]. Again, a noticeable increase in the absorption edge was observed as the particle sizes decrease indicating the effect of quantum confinement. In order to fit the size-dependent trend in experimental data of figure 4.15, an expression proposed by Kayanuma [206] is used

$$E_g(x) = E_g(\infty) + \frac{(\hbar\pi)^2}{2\mu x^2} - \frac{1.786e^2}{(4\pi\epsilon_0\epsilon_r)x} \quad (4.3)$$

where  $E_g(x)$  is the energy bandgap of particles of different sizes,  $E_g(\infty)$  is the energy bandgap of bulk powder,  $\hbar$ , is the reduced Planck's constant,  $\mu$  is reduced mass (effective mass of electron and hole),  $\epsilon_0$  is the permittivity of free space,  $\epsilon_r$  is the dielectric permittivity of material ( $\epsilon_r = 5000$  for BaTiO<sub>3</sub> [116]) and  $x$  is the particle size.

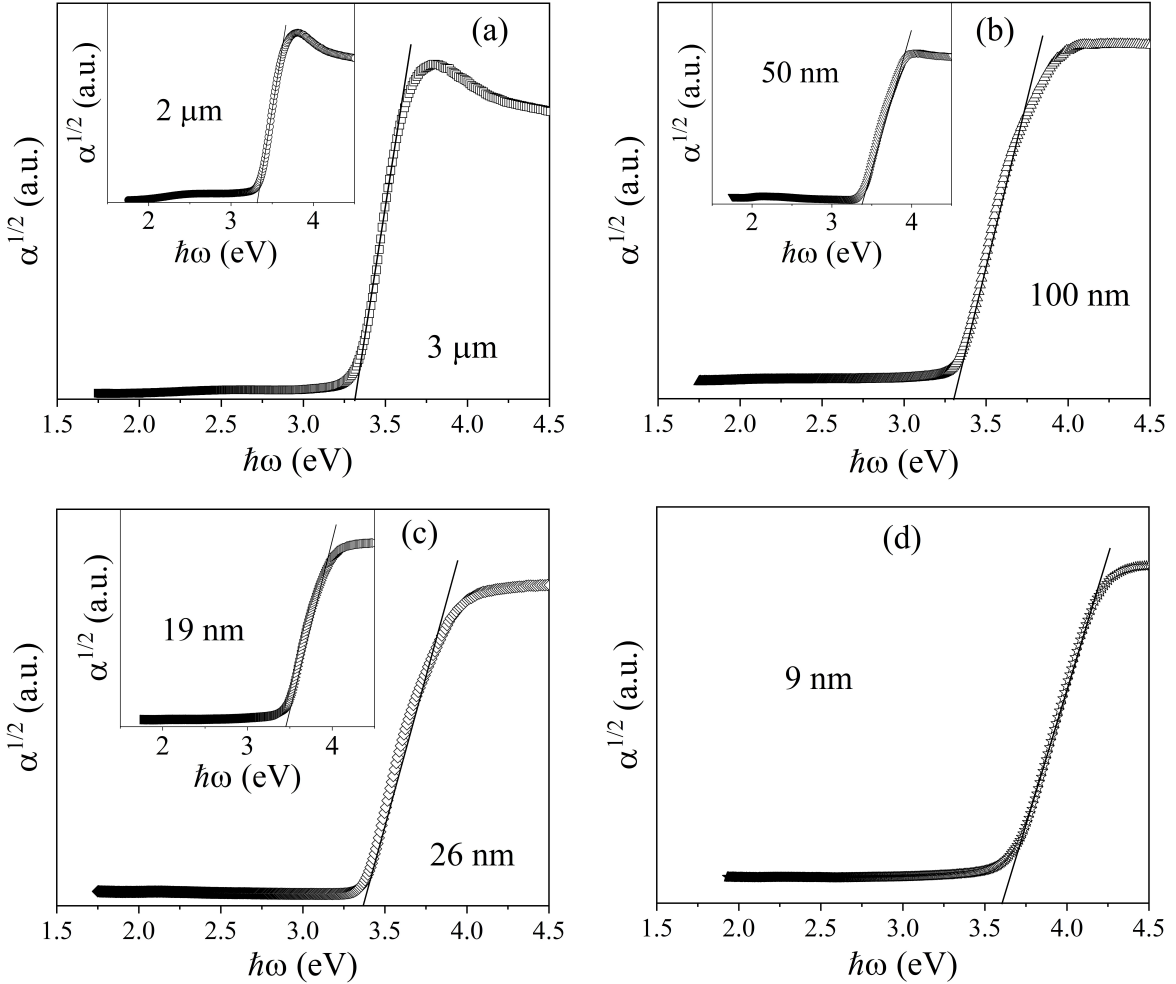


Figure 4.14: (a) - (c) with insets and (d) are the energy bandgap determined via UV-vis-NIR spectroscopy.

Equation 4.3 can be simplified to equation 4.4, which is purely expressed in terms of the particle size,  $x$  and reduced mass,  $\mu$  by inserting the respective parameters. This yields

$$E_g(x) = E_g(\infty) + \frac{1.372 \times 10^{30}}{\mu x^2} - \frac{0.001}{x} \quad (4.4)$$

For emphasis, the standard units of  $\mu$  and  $x$  as used in the above equation are kg and nm, respectively. Moreover, the energy bandgap of these particles depends largely on  $1/x$  than  $1/x^2$  implying that for small particle sizes there is a notable quantum confinement. Thus, equation 4.4 was used to fit the experimental data.

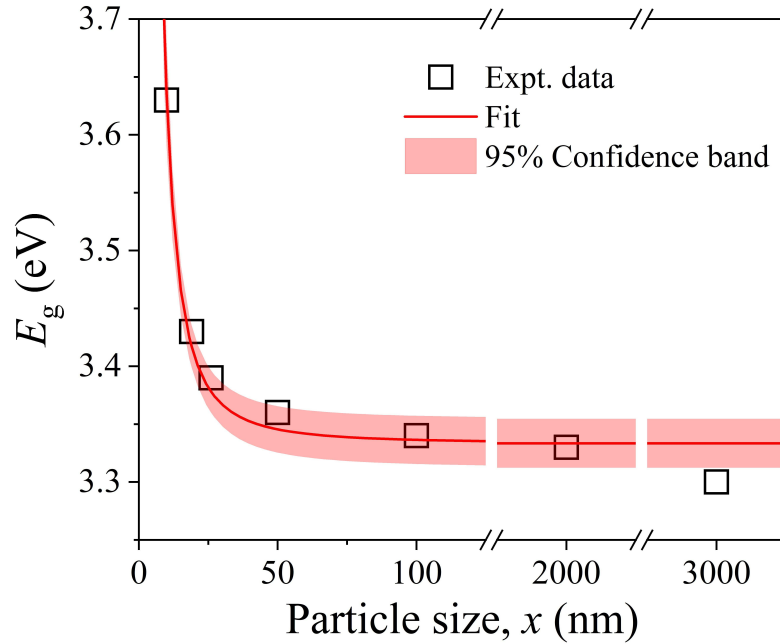


Figure 4.15: The variation of the energy bandgap with the average particle size. The solid line is the fit using equation 4.3.

The fit results with a correlation coefficient of 0.97 gave  $E_g(\infty) = 3.33 \pm 0.01$  eV and  $\mu = (4.53 \pm 0.31) \times 10^{-32}$  kg. The reduced mass which is  $\sim 10\%$  mass of a rest electron may indicate the excitons diffuse quickly in the particles. For instance, if the photochemical catalyzation is meant to proceed at room temperature, then the binding energy of exciton should be lower than the thermal energy  $\sim 26$  meV in order to facilitate the separation [28]. It is also important to note that this energy compared to the bandgap energy of barium titanate is almost 127 times higher, thus making thermal activation of barium titanate unlikely. Being that the Coulombic force of attraction expressed as  $q_1 q_2 / 4\pi\epsilon_0\epsilon_r r^2$  where  $q_1$  and  $q_2$  are electron and hole and  $r$  is the distance apart, shows inverse dependence on relative permittivity  $\epsilon_r$  of the material, it implies that the binding of an exciton will be low and as a consequence dissociates easily. For oxide perovskites like barium titanate, the dielectric permittivity is high and as such demonstrates its importance in charge carrier dissociation or separation mainly along the polar axis. The implication of the obtained reduced mass which is  $\sim 10\%$  mass of a rest electron is that there is a good mobility of separated charge carriers since mobility is inversely related to the reduced effective mass. Besides, for a good mobility in photochemical reactions the requirement is that the reduced effective mas should be less than 50% mass of

a rest electron [26]. At this point, we remark that the slight increase in the energy bandgap offers the advantage of access to initially inaccessible redox couples. However, this brings the disadvantage of limited absorption roughly 1% i.e. less absorption for a given redox pair.

#### 4.2.4 Size effect on the reaction kinetics

To evaluate the photocatalytic performance of varying sizes of these particles, recalcitrant azo dye, methylene orange (MO) was used as the model organic pollutant. As a side note, the systematic study using Raman spectroscopy to monitor the time-dependent photoactivity of MO *in-situ* is further provided in Appendix B. From the time-dependent absorption studies of MO, the photocatalytic performance of the particles was evaluated in terms of the apparent reaction rate constant. The reaction kinetics which was irreversible is determined from the plot of  $\ln(C_0/C_t)$  vs. illumination time,  $t$  as it follows a pseudo first-order L-H mechanism. The same step was taken to assess the kinetics of the adsorption process. Figure 4.16(a) and (b) show the plot of  $\ln(C_0/C_t)$  vs. time,  $t$  for both processes. The extracted reaction rate constants of figure 4.16(a) are shown in figure 4.16(c). From figure 4.16(c), the adsorption kinetics were observed to increase as the particle size decreased. One expects such trend since surface area, a geometry property increases inversely with decrease in particle size. In other words, the fragmentation of large particles results in high surface area. This is hypothetically true since the number of active sites is enhanced by exposing more surface area although at the expense of surface recombination which takes over at very small particle sizes. In figure 4.16(b), the kinetics show two distinct regimes i.e. 0 – 30 min for a fast process and 30 – 60 min for a slightly slow process. The fast process is attributed to L-H mechanism of the first-order kind whereas the deviation from the linear portion (i.e. the slow process) can be explained by a competition between the rate of degradation and desorption of dye. The latter appears to be a consequence of depleted dissolved oxygen for which the kinetic traces flatten. In other words,  $(C_t/C_0)$  would not approach zero at prolonged irradiation time. Thus for a good description of the photocatalytic process involving a first-order kinetics, the first regime i.e. 0 – 30 min was used. The activity is comparatively low for the bulk samples and increases as the particle size is decreased, reaching a maximum when the size is 19 nm. The low activity for the bulk particles is suspected to be a consequence of volume recombination process common

with large crystallized particles [207]. For the nanosized particles,  $19 \text{ nm} \leq x \leq 100 \text{ nm}$  the photoactivity increases reasonably due to enhanced contribution of charge carrier separation and transport mechanism (bulk photovoltaic effect) which is stronger particularly for materials with dimension in that range [122]. At nanoscale, the size of the particle is comparative to the mean free path of excited carriers and therefore all the excited charge carriers contribute to the charge-consuming catalysis. Below this size, the activity drops immediately. The behaviour may be associated to the lost of bulk photovoltaic effect expected for particles below a critical size for transition to a centrosymmetric structure.

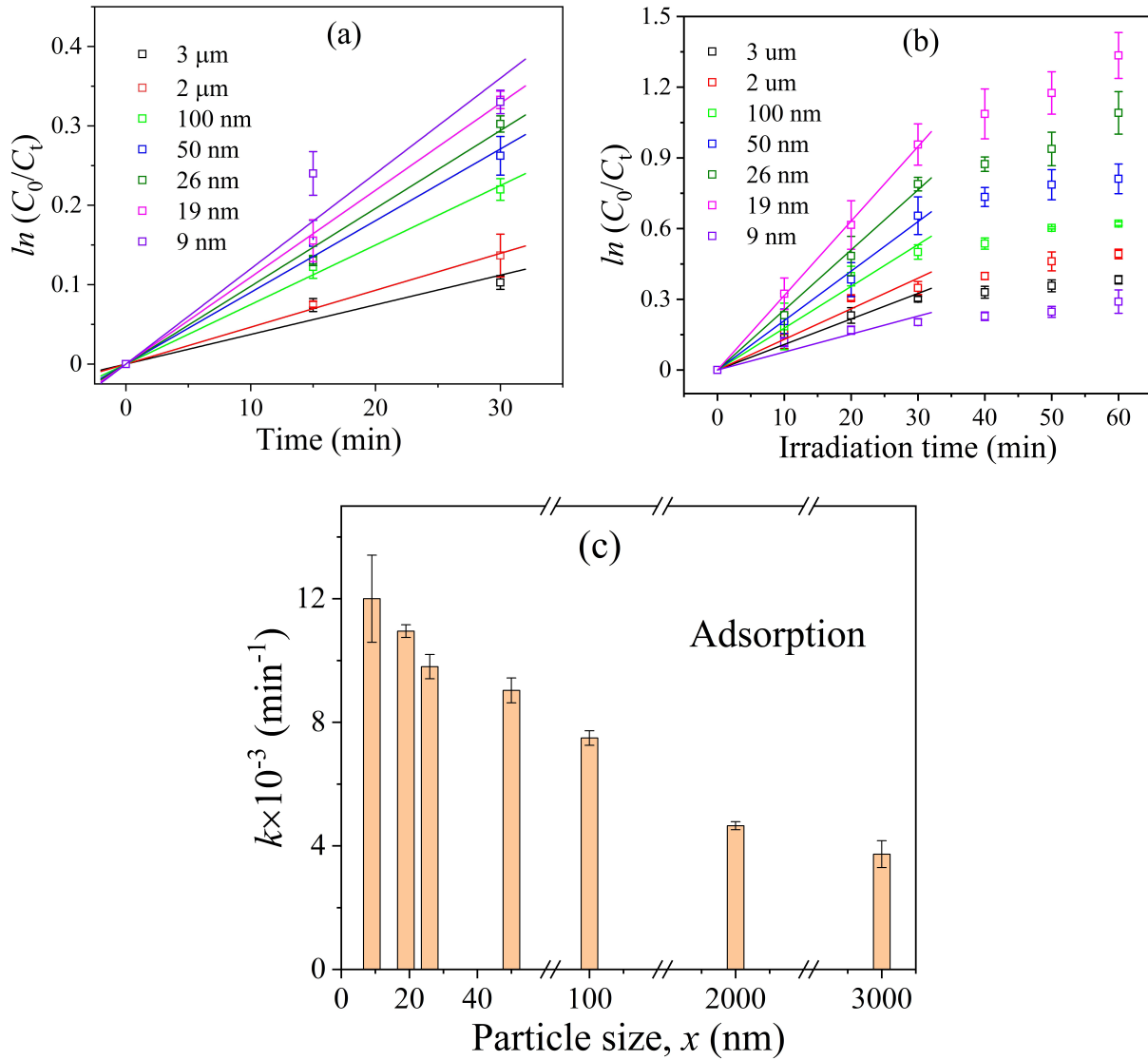


Figure 4.16: The adsorption (a), and degradation (b) kinetics of the particles. Solid lines are linear fits to data between 0 - 30 min corresponding to the L-H mechanism. (c) The bar chart showing the variation of reaction rate constant with particle size extracted from (a).

In very small particles, surface recombination appears to surpass the effect of volume recombination as the electron-hole pairs photogenerated are within the vicinity of suspected surface defects imposed by size [96].

Moreover, the effect of particle size on the kinetics of photocatalytic reaction was explored by examining the rate of degradation of MO and half-life of the photodegradation. In the first case, the rate of photodegradation was observed to increase when the particle size decreased. From the plot (figure 4.17(a)), the rate of photodegradation shows a linear dependence on  $\ln(x)$  i.e.  $k = -0.0041\ln(x) + 0.042$ .

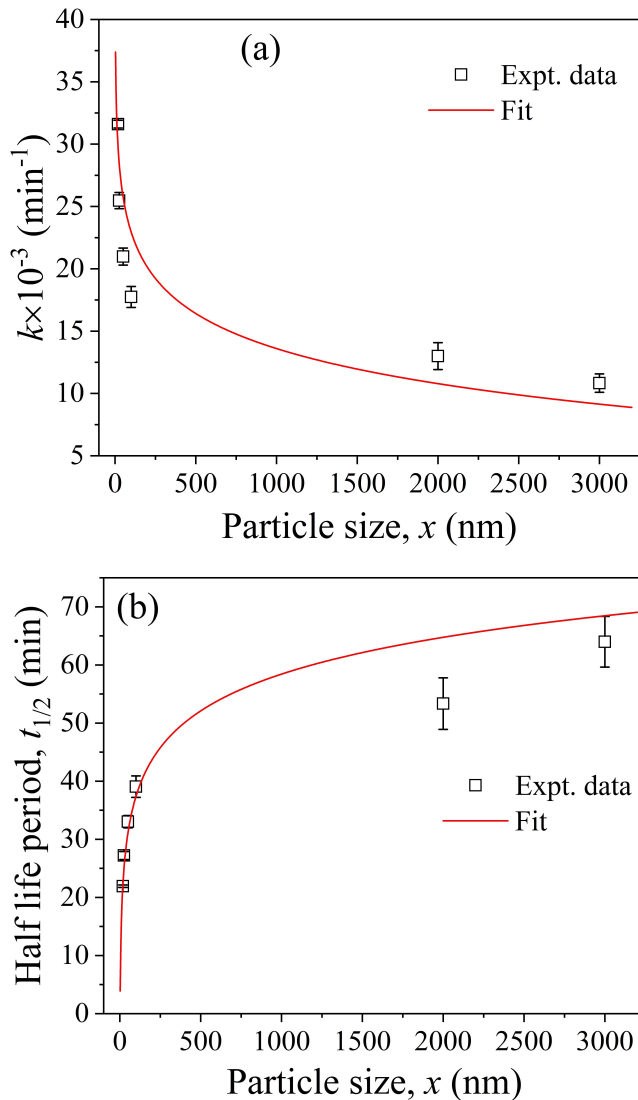


Figure 4.17: (a) The variation of first-order reaction constant for degradation of MO with particle sizes. (b) The half degradation time variation with particle size.

As for the half-life,  $t_{1/2}$ , it is expected that since the degradation kinetics is purely first-order, the reaction rate constant follows the linear fit of the experimental data between 0 – 30 min as obtained initially i.e.  $\ln(C_0/C_t) = kt_{1/2}$ . Therefore, for  $C_0/C_t = 2$ , the half-life of the photodegradation can be determined precisely. The variation of  $t_{1/2}$  as a function of particle size is also shown in figure 4.17(b). It shows that the half-life decreases when the particle size decrease with a logarithmic dependence. The half-life relates with particle size mathematically as  $t_{1/2} = 9.1\ln(x) - 4.7$ . The results obtained from this are summarized in table 4.1.

Table 4.1: The photodegradation rate constant and half-life period for the different sizes of barium titanate.

Particle size (nm)	$k \times 10^{-3}$ (min <sup>-1</sup> )	$t_{1/2}$ (min) Experimental	$t_{1/2}$ (min) Calculated from $t_{1/2} = 9.1\ln(x) - 4.7$
3000	$10.8 \pm 0.7$	$64 \pm 4$	68
2000	$13.0 \pm 1.0$	$53 \pm 4$	65
100	$17.7 \pm 0.8$	$39 \pm 2$	37
50	$21.0 \pm 0.7$	$33 \pm 1$	31
26	$25.5 \pm 0.7$	$27 \pm 1$	25
19	$31.6 \pm 0.3$	$22 \pm 0.2$	22
9	$8.6 \pm 0.8$	$80 \pm 8$	-

To investigate the intrinsic size effect on  $k$ , the empirical function similar to equation 2.15 and thermodynamic model based on equation 2.19 are deployed. Hence, the empirical function for the size-driven rate of reaction could be written as

$$k(x) = k(\infty) \left[ 1 - \frac{C}{x - x_0} \right] \quad (4.5)$$

where  $k(x)$  and  $k(\infty)$  are the rate of reaction for different particle sizes and rate of reaction for the bulk powder, respectively, and  $C$  is a fitting parameter whose sign is arbitrary. The fits to the data are shown in figure 4.18(a) and (b) for both models. From figure 4.18(a), a correlation coefficient of 0.92 is obtained. The disparity is slightly higher when the particles are larger than 100 nm. When the particle sizes are smaller than 100 nm, the predictive power of the model appears to be reliable. This confirms that thermodynamic formalism is mostly suitable for continuous phase of particles [141, 142]. The photocatalytic oxidation is maximum when the particles of barium titanate are in the range 15 - 25 nm prior to diminution.

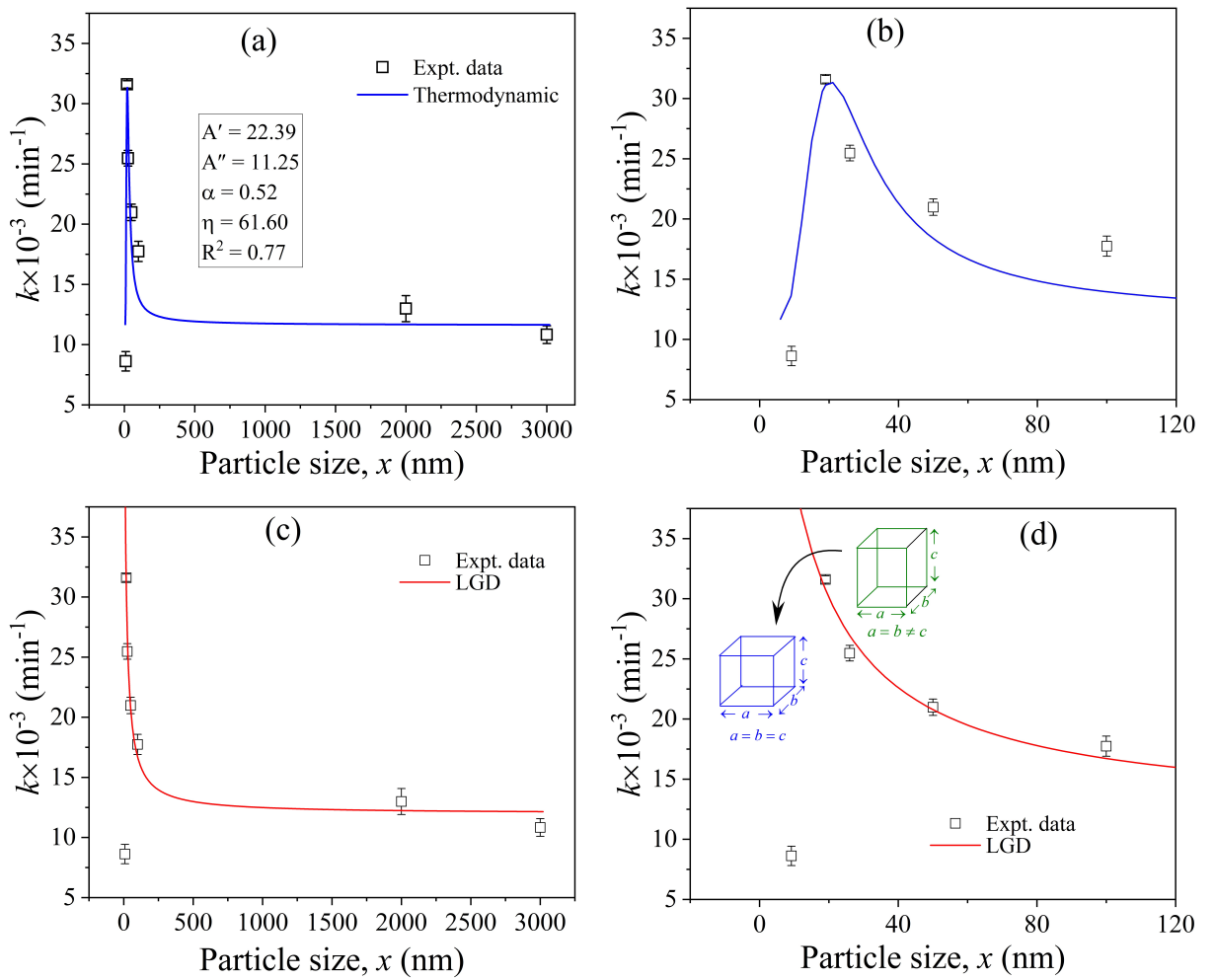


Figure 4.18: The plot of  $k$  as a function of particle size,  $x$ . Solid lines are numerical fit according to (a) equation 2.19 and (c) equation 4.5. The expanded view for particle sizes between 0 - 120 nm are shown in (b) and (d), respectively. The unit cells in green and blue depict the tetragonal-to-cubic phase transition due to decrease in particle size.

Given that the particles in this size distribution have evidence of tetragonality judging by the

results of XRD and Raman spectroscopy, it is believed that the photodegradation kinetics are driven by other processes especially for small particles. Processes such as nanoclustering and surface reconstruction are known to occur for very small particles due to high surface energy [208] resulting from nanoscale instability of the tetragonal phase. The tetragonal phase is favoured by long-range Coloumbic force, which is greatly affected as the size is reduced due to shortened Ti-O bond length in the octahedra. In such a case, the short-range repulsion dominates and the cubic phase of the structure stabilizes. Since a minimum particle size of BaTiO<sub>3</sub> is required to achieve stability of domain containing the active sites, there will be competition between the surface and bulk energy of the nanoparticles [208, 209]. In the event the balance between the long-range Coloumbic force and short-range repulsion is not reached in favour of the former, the latter dominates and the bulk property is lost as result of quick transition to the high-symmetry phase.

Again from figure 4.18(b), we obtained a correlation coefficient of 0.99 indicating a good description of the experimental data. The fit result generates  $k(\infty) = (12.0 \pm 1.0) \times 10^{-3} \text{ min}^{-1}$  and  $x_0 = 8.3 \pm 2.0 \text{ nm}$ , where  $x_0$  is in good agreement with the previous analyses. The critical particle size here demonstrates the physical size for which the net dipole moment still exists in the crystal. Thus we show that non-centrosymmetry, a material property which depends on particle size influences the kinetics of photocatalytic activity of BaTiO<sub>3</sub>. Moreover, the Polanyi parameter  $\alpha$ , and  $\eta$  obtained from equation 2.19 are 0.52 and 61.60, respectively. While the value of Polanyi parameter is consistent with the theoretical value (0.5) [210], the value of  $\eta$  was used to deduce the surface energy of the particles at room temperature. Based on the critical particle size obtained from LGD model, the surface energy,  $\sigma$  yields  $8.2 \pm 2 \text{ J/m}^2$ . This is attributed to a thin surface layer generated by the permanent dipoles [211]. Comparing with the result of Uchino et al. [144] in which the value of  $\sigma$  was estimated to be  $50 \text{ J/m}^2$  for a critical size of 100 nm, we note a substantial decrease in the surface energy nearly four-fold.

#### 4.2.5 Summary of size effects on the photocatalytic activity of polar BaTiO<sub>3</sub> particles

In summary, a microwave-assisted hydrothermal technique was deployed to synthesize barium titanate particles that were compared to larger commercial particles. This particular preparation route enables one to obtain particles of high purity and less agglomeration with high tetragonality unlike the conventional hydrothermal route which crystallizes in less tetrag-

onality and occasionally high symmetry cubic phase. The X-ray diffraction in combination with Raman spectroscopy were used to study the 9 nm - 3  $\mu\text{m}$  particles. We developed a comprehensive understanding of the structural properties by examining quantities like the unit cell distortion ( $c/a - 1$ ) and Curie temperature. Fragmentation of these particles results to enhanced surface area although at the expense of energy bandgap and bulk photovoltaic effect. The size dependent energy bandgap as a consequence of quantum confinement effect therefore was elaborated in terms of quantum confinement model. The time-dependent kinetic traces exhibited two regimes (i.e. fast and slow process), which is best described by a two-phase exponential function. While the best photocatalytic performance was obtained with the 19 nm powder prior to diminution, both thermodynamic and LGD phenomenological formalism were proposed to interpret the experimental results with respect to the mass transport at the photocatalyst-liquid interface and crystal structure, respectively. Based on the particle size distribution considered, the Landau-type phenomenological formalism was suitable for the explanation of size-driven phase transition into the centrosymmetric phase with a critical particle size in the range  $10 \pm 4$  nm. In conclusion, we not only determined the optimum particle size of barium titanate nanoparticles for photocatalysis but also pushed its critical size to even small value.



# Chapter 5

## Conclusion and perspectives

### 5.1 Conclusion

Tetragonal BaTiO<sub>3</sub>, an important member of the BaO-TiO<sub>2</sub> system is shown to be beneficial for photocatalytic applications owing to the presence of bulk photovoltaic effect which is an addition mechanism for charge carrier separation. Its chemical stability in aqueous solution alongside non-toxicity makes it even more suitable in addressing global water challenges. From a commercial viewpoint, the use of microwave-assisted hydrothermal technique was seen to be an efficient technology for the synthesis of these nanoparticles with better and/or controlled physicochemical and enhanced photocatalytic properties should scalability be considered. As established from the study, the photocatalytic activity of the undoped structure was limited since only a small percentage of solar spectrum is absorbed. Through gap-state engineering, the intricate coexistence of light absorption with other functional properties e.g. ferroelectricity was intimately coupled. In particular, this was achieved through metal doping at the B-site; the cationic ratio was controlled and a visible-light sensitive material (photo-pyroelectric) fabricated. From the chromium-iron co-doped systems particularly when the iron content is beyond a certain threshold, we remark that the aftereffect of the extended photoabsorption is a substantial loss in spontaneous polarization which could have assisted in polarization-induced charge carrier separation, so while one of the objectives was to fabricate photo-pyroelectrics with rich visible-light response, a trade-off is always advised. Therefore, all the mono-doped systems exhibited a better photocatalytic activity owing to the synergistic effect of enhanced light absorption and bulk photovoltaic effect. The detrimental effect is discernible when the content of iron in the co-doped system was increased to 8 mol%.

As a consequence, the absorption edge was extended up to 729 nm which is advantageous and implies that red light can be collected at the expense of the bulk property. This was shown by the decreasing  $c/a$  ratio  $\simeq 1.0054(1)$  for 8 mol% Fe in the co-doped sample. Specifically, the aliovalent substitution was shown to be effective in extending the light absorption by creating additional absorption bands, thus enhancing the photocatalytic activity. The distribution of  $Ti^{4+}$ ,  $Fe^{3+}$  and  $Cr^{3+}$  ions over the B-site perovskite in the co-substituted systems manifested in high volume of point defects mainly oxygen vacancy,  $V_O^{..}$ . This high volume of oxygen vacancies provoked the hexagonal phase which eventually might become the stable and dominant phase should the content of iron dopant increased beyond 8 mol%. We thus showed that an optimum transition metal co-doping with appreciable spontaneous polarization was at 4:4 mol% accounting for nearly three-fold increase in degradation rate constant in contrast to that of the undoped  $BaTiO_3$  sample. Finally, we however state that the combinatorial advantage in using chromium does not justify its potential risk as a heavy metal especially for use in water decontamination, but iron can effectively replace chromium nonetheless.

In an effort to offer more surface area resulting to increased number of active sites, investigation on particle size effect was thereafter conducted using pristine  $BaTiO_3$  pyroelectrics. For photocatalytic applications, the band structure was understood to be adjusted leading to extra generation of free radicals through the particle size control. It implies the target redox couple are well aligned in the energy gap thermodynamically. The increased energy gap (up to  $\Delta E_g \sim 0.33$  eV) between the conduction band minimum and the valence band maximum was interpreted as a direct consequence of quantum confinement effect. However, the principal assertion that increased surface area guarantees increased photoactivity may only be implicit and does not apply when particle sizes are  $< 10$  atoms thick as different adsorption mechanism occur. We demonstrated the efficacy of Landau-Ginzburg-Devonshire (LGD) phenomenological model in analyzing the particle size effect on photocatalytic kinetics of barium titanate particles at least up to the critical size. For the thermodynamic model, there is also a physical size required to stabilize the domain that contains the catalytic active sites. Moreover, the structural instability caused by particle size effect as evidenced by both XRD and Raman spectroscopy was an indication that there is a certain physical size for which electric dipoles are sustained in pyroelectric material. This was further justified by the consistency in results obtained from experimental analyses. In particular, the study provided an insight against the fundamental notion that surface area (a geometry factor) is a principal factor towards

enhanced catalytic oxidation. That is, simply increasing the surface area of a catalytic material does not necessarily imply enhanced catalytic performance as the surface area is more connected to number of surface active sites. In any case, there is an optimum particle size in the range  $10\pm4$  nm where the material property exhibits the best photocatalytic kinetics.

## 5.2 Perspectives

Water decontamination using photo-pyroelectric BaTiO<sub>3</sub> nanoparticles was investigated and documented results were indeed promising. Despite the significant progress already made starting from synthesis to application, some aspects of the study would actually require further investigations. For instance, we have ascertained that microwave-assisted hydrothermal method is a viable synthetic strategy to obtain pyroelectric BaTiO<sub>3</sub>. Therefore, well controlled morphologies such as nanocubes, nanowires etc. should be synthesized and their structure–morphology–photocatalytic performance relationship evaluated since the adsorption properties (judging from the morphology of chromium-doped barium titanate) has shown dependence on the aspect ratio. Again, to maintain appreciable photo-response in the pyroelectric BaTiO<sub>3</sub>, co-substitution of iron (Fe) and may be manganese (Mn) could be potentially rewarding. This is because manganese has an acceptable concentration of 0.12 mg/L in drinking water [212], which is safer compared to chromium. Manganese in 3+ state has an ionic radius of 0.645 Å (high spin) and can aliovalently substitute Ti<sup>4+</sup> in the B-site with slight microstructural strain. Moreover, manganese has shown to have practically high degree of solubility in solid solutions without hampering the strength of spontaneous polarization in such distorted material [213]. Therefore, its combination with Fe might even be more promising in providing a synergistic effect of intense visible-light absorption and polarization-induced charge carrier separation. Intriguingly, Matsuo et al. [214] have established that TMs like manganese with partially filled 3d orbital have the capability of producing high volume of carriers via a two-photon absorption process.

In the second study, we demonstrated how particle size affects the BPVE. Furthermore, the validity of the theoretical models were explained and thus the difficulty in predicting the kinetics at very smaller particle sizes. We therefore suggest that barium titanate particles smaller than 9 nm should be synthesized using our recipe i.e. oleic acid as the surface-modifying additive and the photocatalytic performance evaluated. This will facilitate the understanding

of the adsorption mechanism for the small particles < 19 nm and help distinguish processes like nanoclustering, surface reconstruction etc. Once this is achieved, it will enable one to know if a chemically inert support material like graphitic carbon is required to suspend these small pyroelectric nanoparticles. This is to eliminate the tendency of forming agglomerates and the effect of size of the immobilized photocatalyst with such narrow size distribution can be investigated. Since our goal is to maintain high throughput in terms of photocatalytic activity by tailoring the crystal structure of barium titanate with its light absorption, more studies should focus on pushing the critical particle size further to even smaller values. Beyond the crystal structure–photocatalytic activity relationship, a theoretical modeling would assist in elucidating the interplay of active sites and surface electric charges thereby enhancing the heterogeneous photocatalytic activity.

## Part 2

### Appendices:

### Experimental details



# Appendix A

---

## A.1 Experimental details (Section 4.1)

### A.1.1 Materials

Barium hydroxide octahydrate (98%), anatase titanium oxide (99.7%), hydrogen peroxide (30% wt.), chromium nitrate nonahydrate (98%) and iron nitrate nonahydrate (98%) purchased from Sigma-Aldrich Chemicals were used for the material synthesis. For all the studies on photocatalytic activity, methylene orange, MO ([4-[[4-dimethylaminophenyl]-azo] benzene sulfonic acid sodium salt, C<sub>14</sub>H<sub>14</sub>N<sub>3</sub>NaO<sub>3</sub>S) also from Sigma-Aldrich Chemicals was used as the model organic pollutant. All the chemicals were used without further purification. Meanwhile, other species referred to as unintentional doping account for the  $\leq 2\%$  considering the percentage of purity of the precursors.

### A.1.2 Microwave-assisted hydrothermal synthesis of doped pyroelectric BaTiO<sub>3</sub> nanoparticles

In order to circumvent the heating at elevated temperature for longer duration, agglomeration and even loss of chemical homogeneity posed by the conventional hydrothermal technique, the microwave-assisted hydrothermal with advantages such as fast crystallization, cost efficiency, clean technology, highly economical and energy efficient was adopted for the synthesis of these photocatalysts. The internal pressure and temperature of a typical reactor depend on the volume fill factor of the reactor, power level and exposure time of the microwave radiation. For this reason, the volume fill factor was fixed at 0.52 relative to the reactor volume with 23 mL capacity. 50 mmol of titanium dioxide powder was dispersed in 10 mL of distilled water under magnetic stirring at room temperature. 75 mmol of barium hydroxide was then added

followed by 5.2 mmol of chromium nitrate and 2.6 mmol of iron nitrate. The chromium ion was maintained at the same molar concentration (4 mol%) under optimized conditions while varying that of iron ion (i.e. 0, 4 and 8 mol%). After 20 min of constant magnetic stirring, 2 mL of hydrogen peroxide was then added as a mineralizer. It was further stirred for 10 min in order to obtain a homogeneously dispersed solution. The final mixture which was transferred to a Teflon (PTFE) container housed by a microwave-transparent polymer autoclave (from Parr Instrument) was then placed inside a Panasonic Inverter Microwave Oven (2.45 GHz) operating at 120 W for 10 min. The inverter microwave oven has an advantage of controlling the duty cycle of heating such that the power in it remains constant even when the power level changes. The reactor was allowed to cool down for 2 h after the initial microwave exposure, and the process was repeated for another two cycles using the same heating conditions. Having cooled to ambient conditions after the third cycle, the final product was washed with distilled water several times, filtered, and dried in the oven at 80 °C for 15 h. Similarly, undoped samples were prepared without the addition of the TMs.

### A.1.3 Characterization of samples

The structural phase identification was done by X-ray diffraction (XRD) using a Bruker D8 Advance diffractometer operating with Cu-K $\alpha$  radiation ( $\lambda = 1.5406 \text{ \AA}$ ) at room temperature. A JEOL (JEM-2100F) transmission electron microscope (TEM) operating at 200 kV was used to characterize the morphological properties of the samples. Thus the pyroelectric samples were dispersed in 2 mL of ethanol and ultrasonicated for 20 min before a carbon-coated Cu grid was dip-coated. The Raman spectra were acquired using a Horiba iHR320 spectrometer incorporated with a 473 nm DPSS laser. The scattered light was detected by a thermoelectrically cooled CCD (Synapse BIDD QE). Optical absorption studies were done using UV–Vis–NIR spectroscopy (PerkinElmer, Lambda 750). For this purpose, a quartz substrate was used as reference while samples were then prepared by dip-coating of pre-treated quartz substrates in sample-dispersed solution, followed by drying at 80 °C in an oven. The atomic quantification was estimated by X-ray photoelectron spectroscopy (XPS) using a VG Escalab 220i XL system. A 1486.6 eV Al-K $\alpha$  source operating at 15 kV and 20 mA was used while the calibration was done using the ubiquitous C 1s peak positioned at  $284.8 \pm 0.05$  eV.

#### A.1.4 Photocatalytic activity measurement

The photocatalytic performance of the catalysts was thereafter carried out with the setup illustrated in figure A.1 using a standard calibrated solar simulator (150 W xenon lamp, Model - #SS50AAA, PET Photoemission Tech., Inc.). In typical measurements, 50 mg each of the sample was dispersed in 50 mL of 20 mg/L aqueous solution of the model organic pollutant (methylene orange, MO). An adsorption–desorption equilibrium to saturate the surface of the photocatalyst is achieved by magnetic stirring of the mixture in the dark for 30 min. Similar to Carp et al. [28] the time dependent degradation of MO follows a first order L-H kinetics described by the equation A.1

$$\frac{d[C_{MO}]}{dt} = k (C_0 - [C_{MO}]) \quad (\text{A.1})$$

where  $[C_{MO}]$  is the concentration of MO,  $C_0$  is the initial concentration of MO, and  $k$  is the degradation rate constant. The residual concentration of MO as a function of time was calculated from Eq. (1) of Amaechi et al. [176].

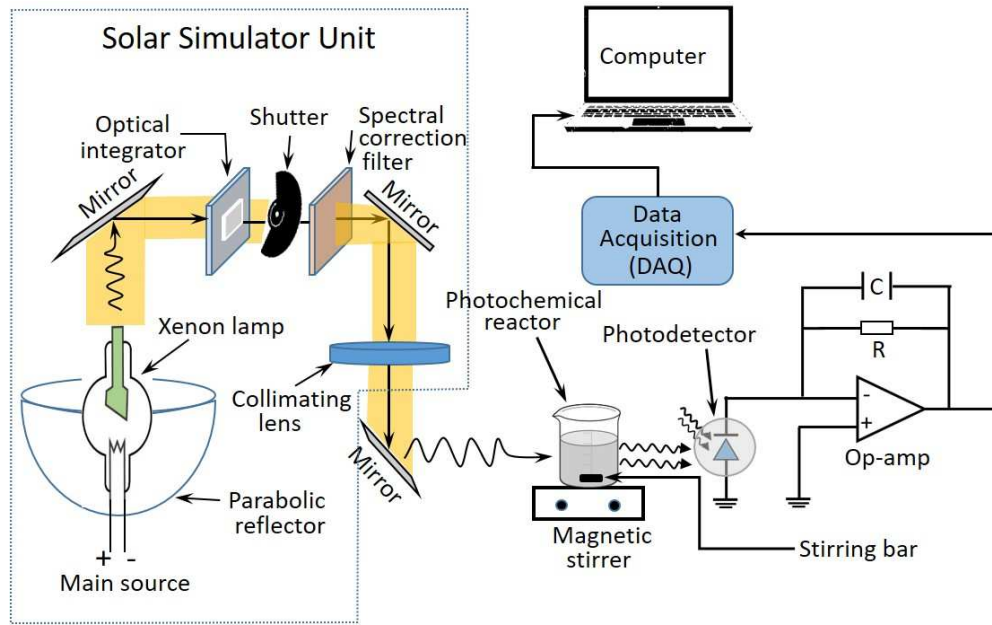


Figure A.1: The setup for measurement of photocatalytic activity.

## A.2 Band structure determination using XPS quantification

First, the electronegativity,  $\chi$  was determined using the geometric mean electronegativities of the samples' individual elements. A BaTiO<sub>3</sub> sample was used as an example:

$$\chi = (2.40^1 \times 3.45^{0.70} \times 7.54^{2.68})^{1/(1+0.70+2.68)} = 5.12 \text{ eV} \quad (\text{A.2})$$

The conduction ( $V_{CB}$ ) and valence band ( $V_{VB}$ ) potentials follow based on equation 2.3:

$$V_{CB} = 5.12 - 4.50 - (0.5 \times 3.18) = -0.97 \text{ eV} \quad (\text{A.3})$$

$$V_{VB} = -0.97 + 3.18 = 2.21 \text{ eV} \quad (\text{A.4})$$

The values obtained from the detailed calculation are summarized in table A.1.

Table A.1: The values of electronegativity, and molar ratio of the samples. Literature values of electronegativity of elements were extracted from the work of Pearson [215].

Element	$\chi$ (eV)	Sample molar ratio						Sample's $\chi$ , $V_{CB}$ & $V_{VB}$ (eV)
		(i)	(ii)	(iii)	(iv)	(v)		
Ba	2.40	1.00	1.00	1.00	1.00	1.00	(i)	5.12, -0.97, & 2.21
Ti	3.45	0.70	0.67	0.77	0.65	0.56	(ii)	4.95, -0.89, & 1.79
O	7.54	2.68	2.54	2.64	2.58	2.60	(iii)	5.02, -0.68, & 1.72
Cr	3.72	-	0.36	-	0.27	0.25	(iv)	4.99, -0.66 & 1.64
Fe	4.06	-	-	0.23	0.08	0.19	(v)	5.01, -0.34, & 1.36

# Appendix B

---

## B.1 Experimental details ( Section 4.2)

### B.1.1 Materials

Analytical grades of barium hydroxide octahydrate (98%), titanium butoxide (97%), hydrogen peroxide (30% wt.), ethanol (99%), polyethylene glycol, (PEG, mol. wt. = 8000, 97%), potassium hydroxide (85%) and barium titanate particles of average particle size of 100 nm, 2  $\mu\text{m}$  and 3  $\mu\text{m}$  were purchased from Sigma Aldrich Chemicals. Oleic acid (90%) was obtained from Alfa Aesar Chemicals. For all the precursors, the percentage of unintentional doping is  $\leq 15\%$ .

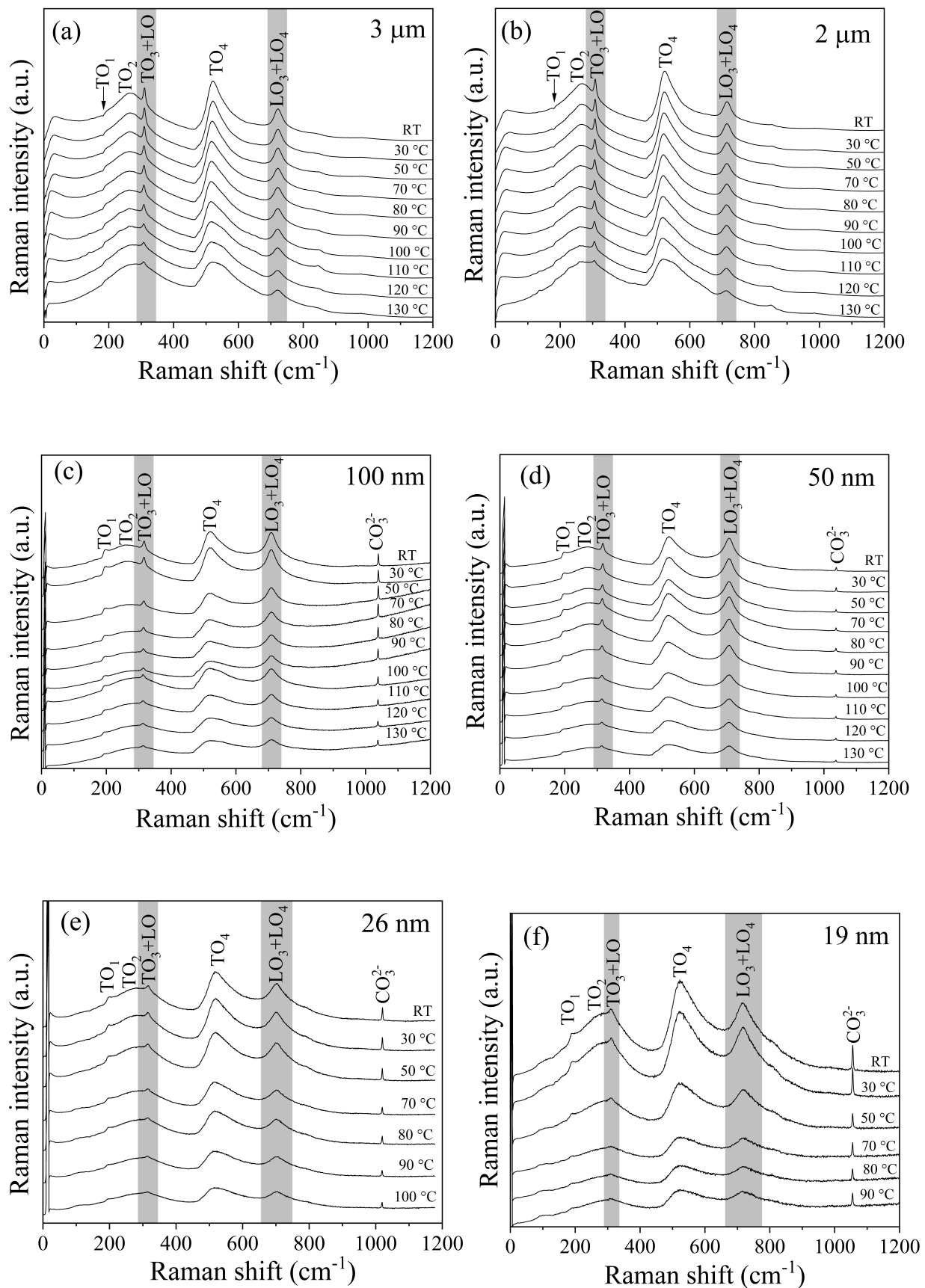
### B.1.2 Microwave-assisted hydrothermal synthesis of pyroelectric BaTiO<sub>3</sub> particles

A titanium ion source was prepared by mixing 50 mmol of titanium butoxide in 5 mL of ethanol. After 10 min of constant magnetic stirring of the solution, 75 mmol of barium hydroxide octahydrate dissolved in 5 mL of preheated distilled water ( $> 90^\circ\text{C}$ ) was then added to the mixture in the presence of 2 mL hydrogen peroxide. PEG-8000 was later added in order to control the size. The final solution was further stirred for additional 10 min before transferring to a 23 mL capacity Teflon. The Teflon was encapsulated in a microwave-transparent polymer autoclave from Parr Instrument and then placed in a Panasonic Inverter Microwave Oven (2.45 GHz) operated at 360 W for 4 min. Having cooled down to room temperature, the resultant product was then washed in preheated distilled water several times prior to drying in the oven operating at 80 °C for 15 h. A similar approach was adopted for the synthesis of  $\sim 9$  nm BaTiO<sub>3</sub> powder except that oleic acid was used instead as the

surface-modifying additive. Briefly, the titanium ion source was prepared followed by addition of 1.5 mL oleic acid in droplets to avoid instant coagulation or precipitation of the titanium ions. The pH of the mixture was adjusted to 13 using 5 M solution of potassium hydroxide after 10 min of rigorous magnetic stirring. Finally, the barium ion source was then added as described earlier. Similar procedure was take to seal the autoclave whereafter we maintained the same microwave heating conditions.

### B.1.3 Characterization of samples

X-ray diffraction (XRD) was used to investigate the crystal structure using a Bruker D8 Advance diffractometer operating with Cu-K $\alpha$  radiation,  $\lambda = 1.5406 \text{ \AA}$ . The scan range and step size are 20 - 70° and 0.02°, respectively. Moreover, all the diffractograms were collected at room temperature. The as-received and synthesized BaTiO<sub>3</sub> particles were characterized using transmission electron microscopy (JOEL Model: JEM-2100F). A Horiba iHR320 spectrometer equipped with a thermoelectrically cooled Horiba Scientific Synapse Back-Illuminated Deep Depletion CCD detector was used to acquire the Raman spectra. A 473 nm DPSS laser was used as the excitation source and a relatively low power was maintained throughout the measurement to minimize thermal effect. For the temperature-dependent Raman spectra, a Linkam THMS600 was used as a heating source. For the purpose of direct comparison of spectra acquired at various temperatures, all the raw Raman data were corrected using a Bose-Einstein thermal factor,  $n(\omega) = \left( e^{-\left( \frac{\hbar\omega}{k_B T} \right)} - 1 \right)^{-1}$  such that  $I_R(\omega) = I(\omega)/[n(\omega) + 1]$  and are presented in figure B.1. In the equation,  $I(\omega)$ ,  $\hbar$ ,  $\omega$ ,  $k_B$ , and  $T$  represent the observed Raman intensity, reduced Planck's constant, Raman frequency, Boltzmann constant ( $1.38 \times 10^{-23} \text{ J/K}$ ) and temperature respectively [216].



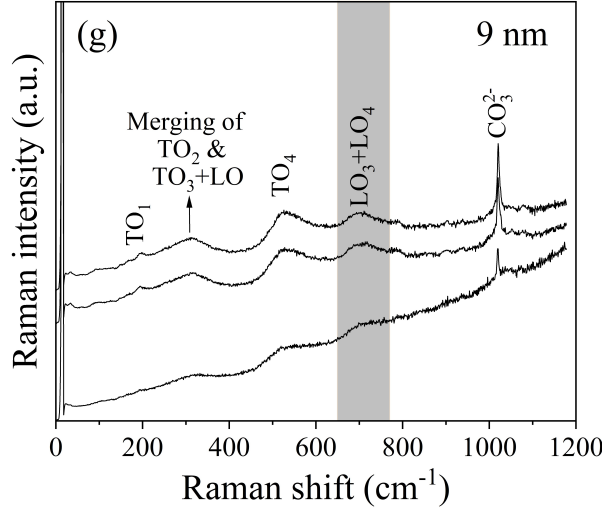


Figure B.1: Temperature evolution of Raman spectra for (a)  $3 \mu\text{m}$ , (b)  $2 \mu\text{m}$ , (c)  $100 \text{ nm}$ , (d)  $50 \text{ nm}$ , (e)  $26 \text{ nm}$ , (f)  $19 \text{ nm}$ , and (g)  $9 \text{ nm}$  particles.

#### B.1.4 Time evolution of MO photodegradation by *in-situ* Raman spectroscopy

Furthermore, the photodegradation of MO as a function of illumination time over the 50 nm BaTiO<sub>3</sub> powder was monitored *in-situ* by Raman spectroscopy. The procedure allows the chemical decomposition of MO over the photocatalyst to be tracked. First, we show the molecular vibration of the organic pollutant (MO) at room temperature prior to addition of barium titanate nanoparticle. The phonon vibrations are matched with those of standard spectrum from the literature [217]. Figure B.2 depicts the Raman spectrum of methylene orange with the most intense peaks  $\sim 1395/1424 \text{ cm}^{-1}$  corresponding to the -N=N- functional group.

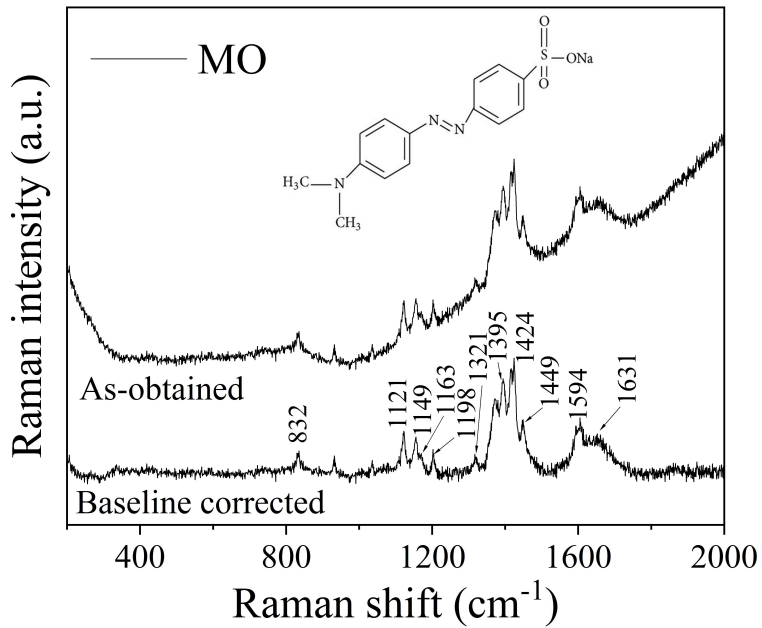


Figure B.2: The Raman spectrum of methylene orange (MO).

As pointed out earlier, this group is responsible for the characteristic colour observed in methylene orange and azo dyes in general. Other Raman modes at 1121/1198 cm<sup>-1</sup> are due to phonon vibration of nitrogen-bonded to phenyl ring (Ph-N). Also, the presence of carbon-carbon (C-C) atomic vibration is denoted by the Raman modes at 1321/1449/1594 cm<sup>-1</sup> while those of carbon-hydrogen (C-H) appear at 1149 cm<sup>-1</sup>. The contribution of water is also observed by the bending vibration at 1631 cm<sup>-1</sup> [218]. The gradual reduction in Raman intensities of these modes over time (figure B.3(a)) clearly shows the distinctive pathway to breaking chemical bonds of the complex organic structure. After 60 min of solar light illumination, water is observed to be one of the dominated remnant structures evident by the nearly symmetric peak between 1600 - 1700 cm<sup>-1</sup>. While no obvious peaks belonging to either TiO<sub>2</sub> or BaO representing partial oxidation of BaTiO<sub>3</sub> could be found, the peaks at 306, 519 and 718 cm<sup>-1</sup> are typical Raman modes of tetragonal phase of the barium titanate photocatalyst. Thus, by fitting a single Lorentzian component to the Raman lineshape between 1500 - 1800 cm<sup>-1</sup> after 60 min of illumination, the result of the fit (figure B.3(b)) shows a maximum at  $1634 \pm 2$  cm<sup>-1</sup> confirming the presence of water.

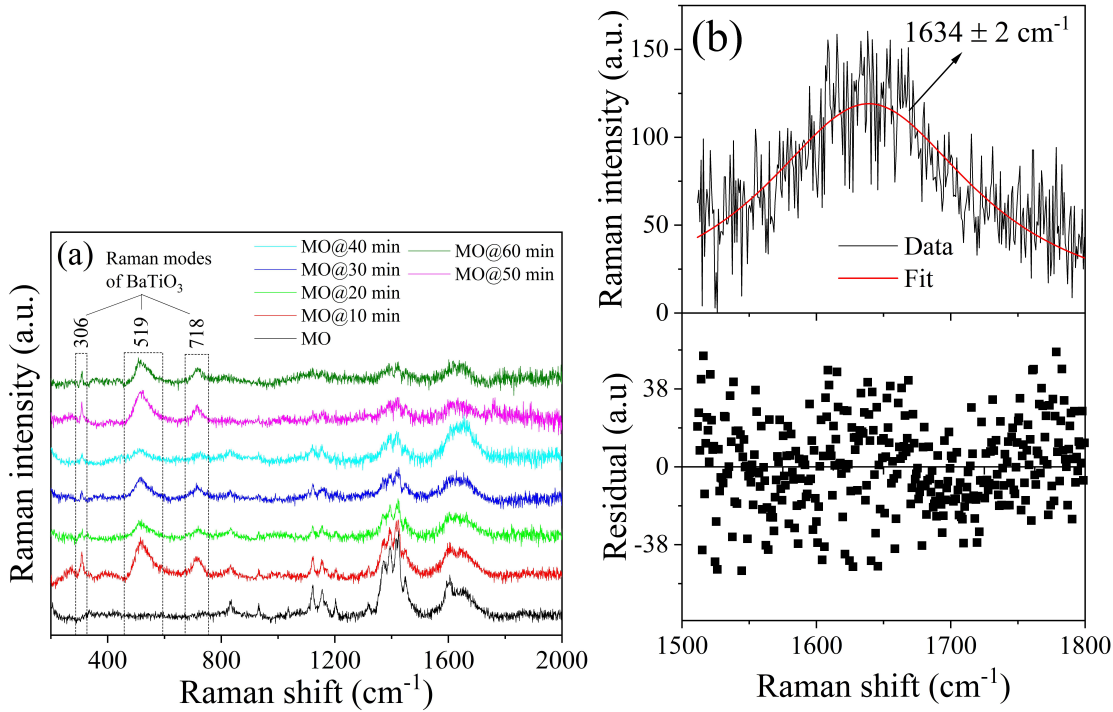


Figure B.3: (a) Time evolution of photodegradation of MO over 50 nm BaTiO<sub>3</sub> powder by *in-situ* Raman spectroscopy. (b) Lorentzian fit of Raman band of water.

The suggested degradation pathway of MO using the pyroelectric barium titanate nanoparticles is shown in figure B.4. As the CB and VB of the system are well aligned in comparison to the target redox couples of the organic pollutant, the OH<sup>•</sup> and O<sub>2</sub><sup>•-</sup> radicals are generated correspondingly when illuminated. This results in cleaving of molecular bonds of the complex structure. The rupture begins with the chromophoric -N=N- bond yielding (i) dimethylaniline, and (ii) sodium benzenesulfonate. While the process of adsorption is expected to be competitive between the parent and intermediate structure, the latter further transforms into (iii) aniline, and (iv) benzenesulfonic acid in the presence of the highly oxidizing radicals. The chemical structures are further ripped apart to produce hydroxyaniline and 4-hydroxybenzenesulfonic acid as depicted by (v) and (vi) respectively. These structures are then hydroxylated into trihydroxybenzene and *p*-benzoquinone (see figure B.4(vii) and (viii)), making it possible for the aromatic rings to be cleaved. Once the aromatic compounds are scissored to molecules without benzene rings (i.e. aliphatic compounds and/or carboxylic acid), it can be easily oxidized into non-toxic compounds such as H<sub>2</sub>O and CO<sub>2</sub> ideally [219–221].

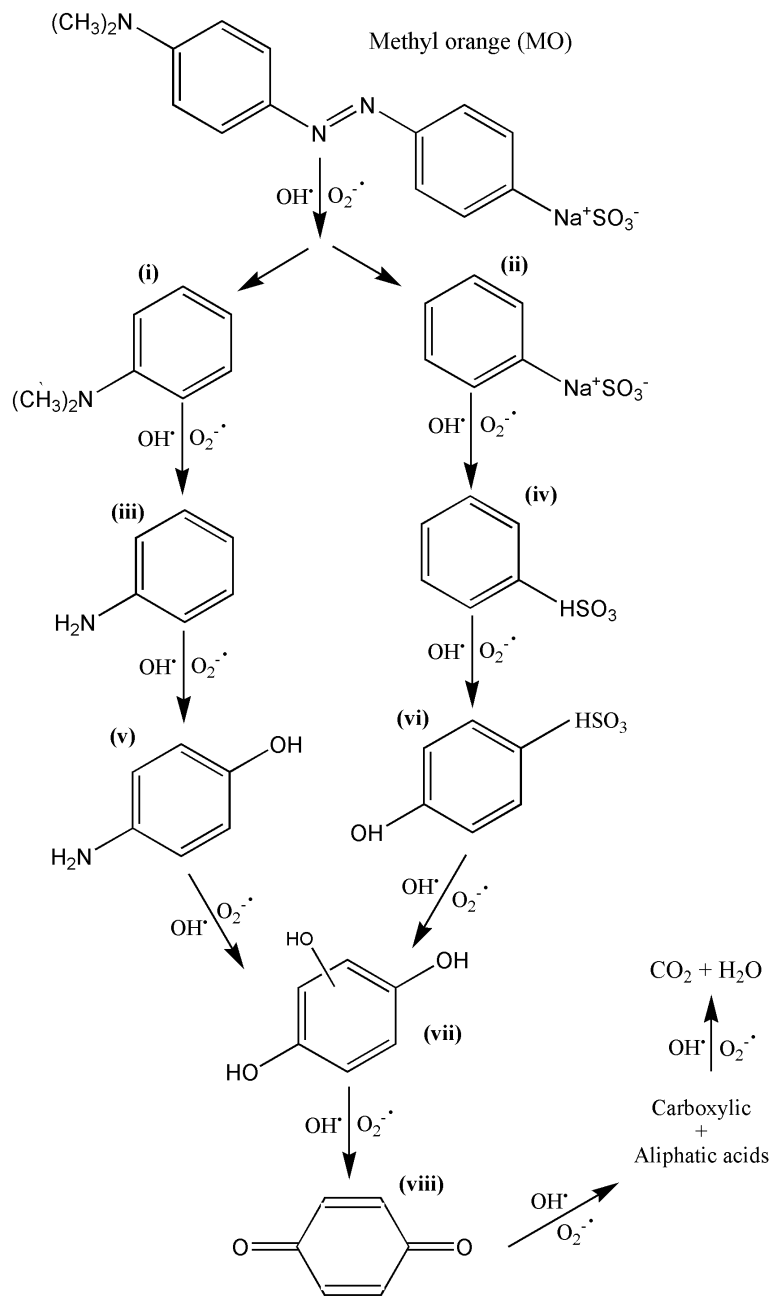


Figure B.4: Proposed photocatalytic degradation pathway of MO over pyroelectric BaTiO<sub>3</sub> nanoparticles.



# References

---

- [1] M. S. Mauter, I. Zucker, F. Perreault, J. R. Werber, J.-H. Kim, and M. Elimelech. “The role of nanotechnology in tackling global water challenges”. In: *Nat. Sustain.* 1.4 (2018), p. 166.
- [2] B. Shi, G. Li, D. Wang, C. Feng, and H. Tang. “Removal of direct dyes by coagulation: The performance of preformed polymeric aluminum species”. In: *J. Hazardous Mater.* 143.1-2 (2007), pp. 567–574.
- [3] V. K. Gupta, R. Jain, and S. Varshney. “Electrochemical removal of the hazardous dye Reactofix Red 3 BFN from industrial effluents”. In: *J. Colloid Interface Sci.* 312.2 (2007), pp. 292–296.
- [4] S.-T. Ong, P.-S. Keng, W.-N. Lee, S.-T. Ha, and Y.-T. Hung. “Dye waste treatment”. In: *Water* 3.1 (2011), pp. 157–176.
- [5] InfoMine. *Commodity and metal prices*. (Accessed September 3, 2020). URL: <https://go.nature.com/2Zy1HeJ>.
- [6] J. C. Stevens. “Finding alternatives to critical materials in photovoltaics and catalysis-Part II: Industrial perspective”. In: *Abstract of Papers of the American Chemical Society*. Vol. 244. Amer Chemical Soc 1155 16TH ST, NW, Washington, DC 20036 USA. 2012, pp. 13–19.
- [7] R. M. Bullock, J. G. Chen, L. Gagliardi, P. J. Chirik, O. K. Farha, C. H. Hendon, C. W. Jones, J. A. Keith, J. Klosin, S. D. Minteer, et al. “Using natureâs blueprint to expand catalysis with Earth-abundant metals”. In: *Science* 369.6505 (2020).
- [8] A. Fujishima and K. Honda. “Electrochemical photolysis of water at a semiconductor electrode”. In: *Nature* 238.5358 (1972), pp. 37–38.

- [9] S. N. Frank and A. J. Bard. "Heterogeneous photocatalytic oxidation of cyanide ion in aqueous solutions at titanium dioxide powder". In: *J. Am. Chem. Soc.* 99.1 (1977), pp. 303–304.
- [10] S. G. Huling and B. E. Pivetz. *In-situ chemical oxidation*. Tech. rep. Environmental Protection Agency Washington DC Office Of Water, 2006.
- [11] Y. Deng and R. Zhao. "Advanced oxidation processes (AOPs) in wastewater treatment". In: *Current Pollution Rep.* 1.3 (2015), pp. 167–176.
- [12] X. Fan, X. Chen, S. Zhu, Z. Li, T. Yu, J. Ye, and Z. Zou. "The structural, physical and photocatalytic properties of the mesoporous Cr-doped TiO<sub>2</sub>". In: *J. Mol. Catal. A: Chem.* 284.1-2 (2008), pp. 155–160.
- [13] T. Ochiai and A. Fujishima. "Photoelectrochemical properties of TiO<sub>2</sub> photocatalyst and its applications for environmental purification". In: *J. Photochem. photobiol. C: Photochem. Rev.* 13.4 (2012), pp. 247–262.
- [14] M. R. Hoffmann, S. T. Martin, W. Choi, and D. W. Bahnemann. "Environmental applications of semiconductor photocatalysis". In: *Chem. Rev.* 95.1 (1995), pp. 69–96.
- [15] Y. Wang, J. Yu, W. Xiao, and Q. Li. "Microwave-assisted hydrothermal synthesis of graphene based Au–TiO<sub>2</sub> photocatalysts for efficient visible-light hydrogen production". In: *J. Mater. Chem. A* 2.11 (2014), pp. 3847–3855.
- [16] I. Arabatzis, T. Stergiopoulos, D. Andreeva, S. Kitova, S. Neophytides, and P. Falaras. "Characterization and photocatalytic activity of Au/TiO<sub>2</sub> thin films for azo-dye degradation". In: *J. Catal.* 220.1 (2003), pp. 127–135.
- [17] H.-Y. Chuang and D.-H. Chen. "Fabrication and photocatalytic activities in visible and UV light regions of Ag@TiO<sub>2</sub> and NiAg@TiO<sub>2</sub> nanoparticles". In: *Nanotechnol.* 20.10 (2009), p. 105704.
- [18] I. Amaechi, R. Katoch, G. Kolhatkar, S. Sun, and A. Ruediger. "Particle size effect on the photocatalytic kinetics of barium titanate powders". In: *Catal. Sci. & Technol.* 10.18 (2020), pp. 6274–6284.
- [19] E. L. Cates. *Photocatalytic water treatment: so where are we going with this?* 2017.
- [20] V. V. Welborn, L. R. Pestana, and T. Head-Gordon. "Computational optimization of electric fields for better catalysis design". In: *Nature Catal.* 1.9 (2018), pp. 649–655.

- [21] H. Fan, H. Li, B. Liu, Y. Lu, T. Xie, and D. Wang. “Photoinduced charge transfer properties and photocatalytic activity in  $\text{Bi}_2\text{O}_3/\text{BaTiO}_3$  composite photocatalyst”. In: *ACS Appl. Mater. Interfaces* 4.9 (2012), pp. 4853–4857.
- [22] D. Ricci, G. Bano, G. Pacchioni, and F. Illas. “Electronic structure of a neutral oxygen vacancy in  $\text{SrTiO}_3$ ”. In: *Phys. Rev. B* 68.22 (2003), p. 224105.
- [23] A. Mazur, O. Schirmer, and S. Mendricks. “Optical absorption and light-induced charge transport of  $\text{Fe}^{2+}$  in  $\text{BaTiO}_3$ ”. In: *Appl. Phys. Lett.* 70.18 (1997), pp. 2395–2397.
- [24] A. Mazur, U. Van Stevendaal, K. Buse, M. Weber, O. Schirmer, H. Hesse, and E. Krätzig. “Light-induced charge transport processes in photorefractive barium titanate crystals doped with iron”. In: *Appl. Phys. B* 65.4-5 (1997), pp. 481–487.
- [25] O. Schirmer, A. Mazur, C. Veber, and A. Ruediger. “Photoinduced charge transport in  $\text{BaTiO}_3$  and congruent  $\text{Ba}_{1-x}\text{Ca}_x\text{TiO}_3$  doped with transition metal and alkali ions”. In: *Advances in photorefractive materials, effects and devices*. Optical Society of America. 1999, p. MC26.
- [26] T. Le Bahers, M. Reîrat, and P. Sautet. “Semiconductors used in photovoltaic and photocatalytic devices: assessing fundamental properties from DFT”. In: *J. Phys. Chem. C* 118.12 (2014), pp. 5997–6008.
- [27] J. Schneider, M. Matsuoka, M. Takeuchi, J. Zhang, Y. Horiuchi, M. Anpo, and D. W. Bahnemann. “Understanding  $\text{TiO}_2$  photocatalysis: mechanisms and materials”. In: *Chem. Rev.* 114.19 (2014), pp. 9919–9986.
- [28] O. Carp, C. L. Huisman, and A. Reller. “Photoinduced reactivity of titanium dioxide”. In: *Prog. Solid State Chem.* 32.1-2 (2004), pp. 33–177.
- [29] X. Tang and K.-a. Hu. “The formation of ilmenite  $\text{FeTiO}_3$  powders by a novel liquid mix and  $\text{H}_2/\text{H}_2\text{O}$  reduction process”. In: *J. Mater. Sci.* 41.23 (2006), pp. 8025–8028.
- [30] J. Lu, Y. Jiang, Y. Zhang, J. Huang, and Z. Xu. “Preparation of gas sensing  $\text{CoTiO}_3$  nanocrystallites using EDTA as the chelating agent in a sol-gel process”. In: *Ceram. Inter.* 41.3 (2015), pp. 3714–3721.
- [31] Y.-J. Lin, Y.-H. Chang, G.-J. Chen, Y.-S. Chang, and Y.-C. Chang. “Effects of Ag-doped  $\text{NiTiO}_3$  on photoreduction of methylene blue under UV and visible light irradiation”. In: *J. Alloy Compds.* 479.1-2 (2009), pp. 785–790.

- [32] F. Nandjou and S. Haussener. “Kinetic competition between water-splitting and photocorrosion reactions in photoelectrochemical devices”. In: *ChemSusChem* 12.9 (2019), pp. 1984–1994.
- [33] P. Kanhere and Z. Chen. “A review on visible light active perovskite-based photocatalysts”. In: *Molecules* 19.12 (2014), pp. 19995–20022.
- [34] J. Kong, T. Yang, Z. Rui, and H. Ji. “Perovskite-based photocatalysts for organic contaminants removal: Current status and future perspectives”. In: *Catal. Today* 327 (2019), pp. 47–63.
- [35] M. L. Moreira, V. M. Longo, W. Avansi Jr, M. M. Ferrer, J. Andres, V. R. Mastelaro, J. A. Varela, and E. Longo. “Quantum mechanics insight into the microwave nucleation of SrTiO<sub>3</sub> nanospheres”. In: *J. Phys. Chem. C* 116.46 (2012), pp. 24792–24808.
- [36] C. Srilakshmi, R. Saraf, V. Prashanth, G. M. Rao, and C. Shivakumara. “Structure and catalytic activity of Cr-doped BaTiO<sub>3</sub> nanocatalysts synthesized by conventional oxalate and microwave assisted hydrothermal methods”. In: *Inorg. Chem.* 55.10 (2016), pp. 4795–4805.
- [37] W. Doerffler and K. Hauffe. “Heterogeneous photocatalysis II. The mechanism of the carbon monoxide oxidation at dark and illuminated zinc oxide surfaces”. In: *J. Catal.* 3.2 (1964), pp. 171–178.
- [38] J.-M. Herrmann, C. Duchamp, M. Karkmaz, B. T. Hoai, H. Lachheb, E. Puzenat, and C. Guillard. “Environmental green chemistry as defined by photocatalysis”. In: *J. Hazardous Mater.* 146.3 (2007), pp. 624–629.
- [39] L. Ge, C. Han, and J. Liu. “Novel visible light-induced g-C<sub>3</sub>N<sub>4</sub>/Bi<sub>2</sub>WO<sub>6</sub> composite photocatalysts for efficient degradation of methyl orange”. In: *Appl. Catal. B: Environ.* 108 (2011), pp. 100–107.
- [40] D. S. Bhatkhande, V. G. Pangarkar, and A. A. C. M. Beenackers. “Photocatalytic degradation for environmental applications—a review”. In: *J. Chem. Technol. & Biotechnol.: International Res. Proc., Environ. & Clean Technol.* 77.1 (2002), pp. 102–116.
- [41] U. A. Joshi, S. Yoon, S. Baik, and J. S. Lee. “Surfactant-free hydrothermal synthesis of highly tetragonal barium titanate nanowires: a structural investigation”. In: *J. Phys. Chem. B* 110.25 (2006), pp. 12249–12256.

- [42] B. C. Hodges, E. L. Cates, and J.-H. Kim. "Challenges and prospects of advanced oxidation water treatment processes using catalytic nanomaterials". In: *Nature Nanotechnol.* 13.8 (2018), pp. 642–650.
- [43] A. Ajmal, I. Majeed, R. N. Malik, H. Idriss, and M. A. Nadeem. "Principles and mechanisms of photocatalytic dye degradation on TiO<sub>2</sub> based photocatalysts: a comparative overview". In: *RSC Adv.* 4.70 (2014), pp. 37003–37026.
- [44] S. Chakrabarti and B. K. Dutta. "Photocatalytic degradation of model textile dyes in wastewater using ZnO as semiconductor catalyst". In: *J. Hazardous Mater.* 112.3 (2004), pp. 269–278.
- [45] M. Sleiman, D. Vildozo, C. Ferronato, and J.-M. Chovelon. "Photocatalytic degradation of azo dye Metanil Yellow: optimization and kinetic modeling using a chemometric approach". In: *Appl. Catal. B: Environ.* 77.1-2 (2007), pp. 1–11.
- [46] J. Sun, X. Wang, J. Sun, R. Sun, S. Sun, and L. Qiao. "Photocatalytic degradation and kinetics of Orange G using nano-sized Sn (IV)/TiO<sub>2</sub>/AC photocatalyst". In: *J. Mol. Catal. A: Chem.* 260.1-2 (2006), pp. 241–246.
- [47] H. Huang, S. Tu, C. Zeng, T. Zhang, A. H. Reshak, and Y. Zhang. "Macroscopic polarization enhancement promoting photo-and piezoelectric-induced charge separation and molecular oxygen activation". In: *Angew. Chem. Int. Ed.* 56.39 (2017), pp. 11860–11864.
- [48] E. Pelizzetti and C. Minero. "Metal oxides as photocatalysts for environmental detoxification". In: *Comments on Inorg. Chem.* 15.5-6 (1994), pp. 297–337.
- [49] C. Nie, J. Dong, P. Sun, C. Yan, H. Wu, and B. Wang. "An efficient strategy for full mineralization of an azo dye in wastewater: a synergistic combination of solar thermo- and electrochemistry plus photocatalysis". In: *RSC Adv.* 7.58 (2017), pp. 36246–36255.
- [50] F. Wang, Y. Wu, M. S. Hybertsen, and T. F. Heinz. "Auger recombination of excitons in one-dimensional systems". In: *Phys. Rev. B* 73.24 (2006), p. 245424.
- [51] Y. Nosaka and M. A. Fox. "Kinetics for electron transfer from laser-pulse irradiated colloidal semiconductors to adsorbed methylviologen: dependence of the quantum yield on incident pulse width". In: *J. Phys. Chem.* 92.7 (1988), pp. 1893–1897.
- [52] A. J. Bard. "Photoelectrochemistry". In: *Science* 207.4427 (1980), pp. 139–144.

- [53] X. Zhang, T. Peng, and S. Song. “Recent advances in dye-sensitized semiconductor systems for photocatalytic hydrogen production”. In: *J. Mater. Chem. A* 4.7 (2016), pp. 2365–2402.
- [54] M. Butler and D. Ginley. “Prediction of flatband potentials at semiconductor-electrolyte interfaces from atomic electronegativities”. In: *J. Electrochem. Soc.* 125.2 (1978), pp. 228–232.
- [55] B. Chai, T. Peng, P. Zeng, and X. Zhang. “Preparation of a MWCNTs/ZnIn<sub>2</sub>S<sub>4</sub> composite and its enhanced photocatalytic hydrogen production under visible-light irradiation”. In: *Dalton Trans.* 41.4 (2012), pp. 1179–1186.
- [56] K. Rajeshwar. “Photoelectrochemistry and the environment”. In: *J. Appl. Electrochem.* 25.12 (1995), pp. 1067–1082.
- [57] M. Grätzel. “Photoelectrochemical cells”. In: *Nature* 414.6861 (2001), p. 338.
- [58] A. D. Bokare and W. Choi. “Review of iron-free Fenton-like systems for activating H<sub>2</sub>O<sub>2</sub> in advanced oxidation processes”. In: *J. Hazardous Mater.* 275 (2014), pp. 121–135.
- [59] S.-J. Hwang, C. Petucci, and D. Raftery. “In situ solid-state NMR studies of trichloroethylene photocatalysis: formation and characterization of surface-bound intermediates”. In: *J. Am. Chem. Soc.* 120.18 (1998), pp. 4388–4397.
- [60] P. Sabatier. *La catalyse en chimie organique*. Nouveau Monde éditions, 2014.
- [61] A. B. Laursen, I. C. Man, O. L. Trinhammer, J. Rossmeisl, and S. Dahl. “The Sabatier principle illustrated by catalytic H<sub>2</sub>O<sub>2</sub> decomposition on metal surfaces”. In: *J. Chem. Edu.* 88.12 (2011), pp. 1711–1715.
- [62] J. Dean, M. G. Taylor, and G. Mpourmpakis. “Unfolding adsorption on metal nanoparticles: Connecting stability with catalysis”. In: *Sci. Adv.* 5.9 (2019), eaax5101.
- [63] S. Martha, P. C. Sahoo, and K. Parida. “An overview on visible light responsive metal oxide based photocatalysts for hydrogen energy production”. In: *RSC Adv.* 5.76 (2015), pp. 61535–61553.
- [64] E. Topkaya, M. Konyar, H. C. Yatmaz, and K. Öztürk. “Pure ZnO and composite ZnO/TiO<sub>2</sub> catalyst plates: A comparative study for the degradation of azo dye, pesticide and antibiotic in aqueous solutions”. In: *J. Colloid Interface Sci.* 430 (2014), pp. 6–11.

- [65] A. Di Paola, E. García-López, G. Marci, and L. Palmisano. “A survey of photocatalytic materials for environmental remediation”. In: *J. Hazardous Mater.* 211 (2012), pp. 3–29.
- [66] H. Li, W. Tu, Y. Zhou, and Z. Zou. “Z-Scheme photocatalytic systems for promoting photocatalytic performance: recent progress and future challenges”. In: *Adv. Sci.* 3.11 (2016), p. 1500389.
- [67] Q. Xu, L. Zhang, J. Yu, S. Wageh, A. A. Al-Ghamdi, and M. Jaroniec. “Direct Z-scheme photocatalysts: principles, synthesis, and applications”. In: *Mater. Today* 21.10 (2018), pp. 1042–1063.
- [68] Y. Ma, X. Wang, Y. Jia, X. Chen, H. Han, and C. Li. “Titanium dioxide-based nano-materials for photocatalytic fuel generations”. In: *Chem. Rev.* 114.19 (2014), pp. 9987–10043.
- [69] A. Kudo and Y. Miseki. “Heterogeneous photocatalyst materials for water splitting”. In: *Chem. Soc. Rev.* 38.1 (2009), pp. 253–278.
- [70] F. Haque, T. Daeneke, K. Kalantar-zadeh, and J. Z. Ou. “Two-dimensional transition metal oxide and chalcogenide-based photocatalysts”. In: *Nano-micro Lett.* 10.2 (2018), p. 23.
- [71] H. Yin, Y. Wada, T. Kitamura, and S. Yanagida. “Photoreductive dehalogenation of halogenated benzene derivatives using ZnS or CdS nanocrystallites as photocatalysts”. In: *Environ. Sci. & Technol.* 35.1 (2001), pp. 227–231.
- [72] I. Yonenaga. “Thermo-mechanical stability of wide-bandgap semiconductors: high temperature hardness of SiC, AlN, GaN, ZnO and ZnSe”. In: *Phys. B: Condens. Matter* 308 (2001), pp. 1150–1152.
- [73] T. Kida, Y. Minami, G. Guan, M. Nagano, M. Akiyama, and A. Yoshida. “Photocatalytic activity of gallium nitride for producing hydrogen from water under light irradiation”. In: *J. Mater. Sci.* 41.11 (2006), pp. 3527–3534.
- [74] H. S. Jung, Y. J. Hong, Y. Li, J. Cho, Y.-J. Kim, and G.-C. Yi. “Photocatalysis using GaN nanowires”. In: *ACS nano* 2.4 (2008), pp. 637–642.
- [75] P. Dhanasekaran, H. G. Salunke, and N. M. Gupta. “Visible-light-induced photosplitting of water over  $\gamma'$ -Fe<sub>4</sub>N and  $\gamma'$ -Fe<sub>4</sub>N/ $\alpha$ -Fe<sub>2</sub>O<sub>3</sub> nanocatalysts”. In: *J. Phys. Chem. C* 116.22 (2012), pp. 12156–12164.

- [76] H. Chen, D. Jiang, Z. Sun, R. M. Irfan, L. Zhang, and P. Du. "Cobalt nitride as an efficient cocatalyst on CdS nanorods for enhanced photocatalytic hydrogen production in water". In: *Cataly. Sci. & Technol.* 7.7 (2017), pp. 1515–1522.
- [77] Z. Sun, H. Chen, L. Zhang, D. Lu, and P. Du. "Enhanced photocatalytic H<sub>2</sub> production on cadmium sulfide photocatalysts using nickel nitride as a novel cocatalyst". In: *J. Mater. Chem. A* 4.34 (2016), pp. 13289–13295.
- [78] J. Sato, N. Saito, Y. Yamada, K. Maeda, T. Takata, J. N. Kondo, M. Hara, H. Kobayashi, K. Domen, and Y. Inoue. "RuO<sub>2</sub>-loaded  $\beta$ -Ge<sub>3</sub>N<sub>4</sub> as a non-oxide photocatalyst for overall water splitting". In: *J. Am. Chem. Soc.* 127.12 (2005), pp. 4150–4151.
- [79] S. S. K. Ma, T. Hisatomi, K. Maeda, Y. Moriya, and K. Domen. "Enhanced water oxidation on Ta<sub>3</sub>N<sub>5</sub> photocatalysts by modification with alkaline metal salts". In: *J. Am. Chem. Soc.* 134.49 (2012), pp. 19993–19996.
- [80] P. Senthil Kumar, S. Sobiya, M. Selvakumar, S. Ganesh Babu, and S. Karuthapanian. "Hierarchically structured CuO/g-C<sub>3</sub>N<sub>4</sub> heterogeneous semiconductor photocatalyst with improved photocatalytic activity and stability". In: *Energy Environ. Focus* 5.2 (2016), pp. 139–149.
- [81] F. K. Kessler, Y. Zheng, D. Schwarz, C. Merschjann, W. Schnick, X. Wang, and M. J. Bojdys. "Functional carbon nitride materials-design strategies for electrochemical devices". In: *Nature Rev. Mater.* 2.6 (2017), p. 17030.
- [82] Y. Zheng, L. Lin, B. Wang, and X. Wang. "Graphitic carbon nitride polymers toward sustainable photoredox catalysis". In: *Angewandte Chemie International Edition* 54.44 (2015), pp. 12868–12884.
- [83] Y. Guo, F. Kong, S. Chu, L. Luo, J. Yang, Y. Wang, and Z. Zou. "Simultaneous sensitization and hole activation in carbon nitride polymer sensitized TiO<sub>2</sub>". In: *RSC Adv.* 2.13 (2012), pp. 5585–5590.
- [84] S. Kumar, B. Kumar, A. Baruah, and V. Shanker. "Synthesis of magnetically separable and recyclable g-C<sub>3</sub>N<sub>4</sub>-Fe<sub>3</sub>O<sub>4</sub> hybrid nanocomposites with enhanced photocatalytic performance under visible-light irradiation". In: *J. Phys. Chem. C* 117.49 (2013), pp. 26135–26143.

- [85] Y. Wang, R. Shi, J. Lin, and Y. Zhu. “Enhancement of photocurrent and photocatalytic activity of ZnO hybridized with graphite-like C<sub>3</sub>N<sub>4</sub>”. In: *Energy & Environ. Sci.* 4.8 (2011), pp. 2922–2929.
- [86] G. Popov, M. Greenblatt, and M. Croft. “Large effects of A-site average cation size on the properties of the double perovskites Ba<sub>2-x</sub> Sr<sub>x</sub>MnReO<sub>6</sub>: A d<sup>5</sup> - d<sup>1</sup> system”. In: *Phys. Rev. B* 67.2 (2003), p. 024406.
- [87] S. Khalfin and Y. Bekenstein. “Advances in lead-free double perovskite nanocrystals, engineering band-gaps and enhancing stability through composition tunability”. In: *Nanoscale* 11.18 (2019), pp. 8665–8679.
- [88] K. Aleksandrov and V. Beznosikov. “Hierarchies of perovskite-like crystals”. In: *Phys. Solid State* 39.5 (1997), pp. 695–715.
- [89] J. T. Carneiro, T. J. Savenije, J. A. Moulijn, and G. Mul. “Toward a physically sound structure- activity relationship of TiO<sub>2</sub>-based photocatalysts”. In: *J. Phys. Chem. C* 114.1 (2009), pp. 327–332.
- [90] L. Liu, H. Zhao, J. M. Andino, and Y. Li. “Photocatalytic CO<sub>2</sub> reduction with H<sub>2</sub>O on TiO<sub>2</sub> nanocrystals: Comparison of anatase, rutile, and brookite polymorphs and exploration of surface chemistry”. In: *ACS Catal.* 2.8 (2012), pp. 1817–1828.
- [91] Q. Sun, Y. Lu, H. Zhang, H. Zhao, H. Yu, J. Xu, Y. Fu, D. Yang, and Y. Liu. “Hydrothermal fabrication of rutile TiO<sub>2</sub> submicrospheres on wood surface: An efficient method to prepare UV-protective wood”. In: *Mater. Chem. Phys.* 133.1 (2012), pp. 253–258.
- [92] H. Zhang and J. Banfield. “Stability of nanosized TiO<sub>2</sub> particles”. In: *J. Mater. Chem* 8 (1998), pp. 2073–2076.
- [93] H. Zhang and J. F. Banfield. “Understanding polymorphic phase transformation behavior during growth of nanocrystalline aggregates: insights from TiO<sub>2</sub>”. In: *J. Phys. Chem. B* 104.15 (2000), pp. 3481–3487.
- [94] J.-M. Herrmann. “Heterogeneous photocatalysis: fundamentals and applications to the removal of various types of aqueous pollutants”. In: *Catal. Today* 53.1 (1999), pp. 115–129.

- [95] J. Zhang, P. Zhou, J. Liu, and J. Yu. “New understanding of the difference of photocatalytic activity among anatase, rutile and brookite TiO<sub>2</sub>”. In: *Phys. Chem. Chem. Phys.* 16.38 (2014), pp. 20382–20386.
- [96] L. Li, P. A. Salvador, and G. S. Rohrer. “Photocatalysts with internal electric fields”. In: *Nanoscale* 6.1 (2014), pp. 24–42.
- [97] B. Wul and I. Goldman. “Dielectric hysteresis in barium titanate”. In: *Comptes rendus de l'Académie des sciences de l'URSS* 51 (1946), pp. 21–23.
- [98] S. Nayak, B. Sahoo, T. K. Chaki, and D. Khastgir. “Facile preparation of uniform barium titanate (BaTiO<sub>3</sub>) multipods with high permittivity: impedance and temperature dependent dielectric behavior”. In: *RSC Adv.* 4.3 (2014), pp. 1212–1224.
- [99] M. Acosta, N. Novak, V. Rojas, S. Patel, R. Vaish, J. Koruza, G. Rossetti Jr, and J. Rödel. “BaTiO<sub>3</sub>-based piezoelectrics: Fundamentals, current status, and perspectives”. In: *Appl. Phys. Rev.* 4.4 (2017), p. 041305.
- [100] F. Li, M. Zeng, H. Yu, H. Xu, and J. Li. “Dielectric characteristics of B-site-modified hexagonal-barium titanate”. In: *J. Mater. Sci.: Mater. Electron.* 27.3 (2016), pp. 2836–2840.
- [101] R. E. Cohen. “Origin of ferroelectricity in perovskite oxides”. In: *Nature* 358.6382 (1992), p. 136.
- [102] V. M. Goldschmidt. “Die gesetze der krystallochemie”. In: *Naturwissenschaften* 14.21 (1926), pp. 477–485.
- [103] R. D. Shannon. “Revised effective ionic radii and systematic studies of interatomic distances in halides and chalcogenides”. In: *Acta Crystal., Sect. A: Crystal. Phys., Diff., Theor. Gen. Crystal.* 32.5 (1976), pp. 751–767.
- [104] W. Travis, E. Glover, H. Bronstein, D. Scanlon, and R. Palgrave. “On the application of the tolerance factor to inorganic and hybrid halide perovskites: a revised system”. In: *Chem. Sci.* 7.7 (2016), pp. 4548–4556.
- [105] K. Suzuki and K. Kijima. “Optical band gap of barium titanate nanoparticles prepared by RF-plasma chemical vapor deposition”. In: *Jpn. J. Appl. Phys.* 44.4R (2005), p. 2081.
- [106] T. Moss. *Optical properties of semiconductors*. London: Butterworth, 1959.

- [107] S. Wemple. “Polarization fluctuations and the optical-absorption edge in BaTiO<sub>3</sub>”. In: *Phys. Rev. B* 2.7 (1970), p. 2679.
- [108] H. Matsuda, M. Kuwabara, K.-i. Yamada, H. Shimooka, and S. Takahashi. “Optical absorption in sol-gel-derived crystalline barium titanium fine particles”. In: *J. Am. Ceram. Soc.* 81.11 (1998), pp. 3010–3012.
- [109] N. N. Hasbullah, S. K. Chen, K. B. Tan, Z. A. Talib, J. Y. C. Liew, and O. J. Lee. “Photoluminescence activity of BaTiO<sub>3</sub> nanocubes via facile hydrothermal synthesis”. In: *J. Mater. Sci.: Mater. Electrons.* 30.5 (2019), pp. 5149–5157.
- [110] K. Fujihara, S. Izumi, T. Ohno, and M. Matsumura. “Time-resolved photoluminescence of particulate TiO<sub>2</sub> photocatalysts suspended in aqueous solutions”. In: *J. Photochem. Photobiol. A: Chem.* 132.1-2 (2000), pp. 99–104.
- [111] P. Maity, O. F. Mohammed, K. Katsiev, and H. Idriss. “Study of the bulk charge carrier dynamics in anatase and rutile TiO<sub>2</sub> single crystals by femtosecond time-resolved spectroscopy”. In: *The Journal of Physical Chemistry C* 122.16 (2018), pp. 8925–8932.
- [112] S. Lu, Z. Xu, H. Chen, C. Mak, K. Wong, K. Li, and K. Cheah. “Time-resolved photoluminescence of barium titanate ultrafine powders”. In: *J. Appl. Phys.* 99.6 (2006), p. 064103.
- [113] R. Gonzalez, R. Zallen, and H. Berger. “Infrared reflectivity and lattice fundamentals in anatase TiO<sub>2</sub>”. In: *Phys. Rev. B* 55.11 (1997), p. 7014.
- [114] R. A. Parker. “Static Dielectric Constant of Rutile (TiO<sub>2</sub>), 1.6-1060 K”. In: *Phys. Rev.* 124.6 (1961), p. 1719.
- [115] G. Arlt, D. Hennings, and G. De With. “Dielectric properties of fine-grained barium titanate ceramics”. In: *J. Appl. Phys.* 58.4 (1985), pp. 1619–1625.
- [116] D. Mahgerefteh, D. Kirillov, R. S. Cudney, G. D. Bacher, R. M. Pierce, and J. Feinberg. “Anisotropy of the hole drift mobility in barium titanate”. In: *Phys. Rev. B* 53.11 (1996), p. 7094.
- [117] A. G. Chynoweth. “Surface space-charge layers in barium titanate”. In: *Phys. Rev.* 102.3 (1956), p. 705.

- [118] L. Z. Tan, F. Zheng, S. M. Young, F. Wang, S. Liu, and A. M. Rappe. “Shift current bulk photovoltaic effect in polar materialsâhybrid and oxide perovskites and beyond”. In: *NPJ Computational Mater.* 2 (2016), p. 16026.
- [119] R. Von Baltz. “Theory of the anomalous bulk photovoltaic effect in ferroelectrics”. In: *Phys. Status Solidi B* 89.2 (1978), pp. 419–429.
- [120] V. M. Fridkin. “Bulk photovoltaic effect in noncentrosymmetric crystals”. In: *Crystal. Rep.* 46.4 (2001), pp. 654–658.
- [121] J. E. Spanier, V. M. Fridkin, A. M. Rappe, A. R. Akbashev, A. Polemi, Y. Qi, Z. Gu, S. M. Young, C. J. Hawley, D. Imbrenda, et al. “Power conversion efficiency exceeding the Shockley–Queisser limit in a ferroelectric insulator”. In: *Nat. Photon.* 10.9 (2016), pp. 611–616.
- [122] K. T. Butler, J. M. Frost, and A. Walsh. “Ferroelectric materials for solar energy conversion: photoferroics revisited”. In: *Energy & Environ. Sci.* 8.3 (2015), pp. 838–848.
- [123] S. M. Young and A. M. Rappe. “First principles calculation of the shift current photovoltaic effect in ferroelectrics”. In: *Phys. Rev. Lett.* 109.11 (2012), p. 116601.
- [124] M. Trainer. “Ferroelectrics and the Curie-Weiss law”. In: *Euro. J. Phys.* 21.5 (2000), p. 459.
- [125] E. Aksel and J. L. Jones. “Advances in lead-free piezoelectric materials for sensors and actuators”. In: *Sensors* 10.3 (2010), pp. 1935–1954.
- [126] I. Chang. “Dielectric function and the Lyddane-Sachs-Teller relation for crystals with Debye polarization”. In: *Phys. Rev. B* 14.10 (1976), p. 4318.
- [127] G. Philippot, C. Elissalde, M. Maglione, and C. Aymonier. “Supercritical fluid technology: A reliable process for high quality BaTiO<sub>3</sub> based nanomaterials”. In: *Adv. Powder Technol.* 25.5 (2014), pp. 1415–1429.
- [128] T. Hoshina, K. Takizawa, J. Li, T. Kasama, H. Kakemoto, and T. Tsurumi. “Domain size effect on dielectric properties of barium titanate ceramics”. In: *Jpn. J. Appl. Phys.* 47.9S (2008), p. 7607.
- [129] H.-W. Lee, S. Moon, C.-H. Choi, and D. K. Kim. “Synthesis and size control of tetragonal barium titanate nanopowders by facile solvothermal method”. In: *J. Am. Ceram. Soc.* 95.8 (2012), pp. 2429–2434.

- [130] T. Hoshina, S. Wada, Y. Kuroiwa, and T. Tsurumi. “Composite structure and size effect of barium titanate nanoparticles”. In: *Appl. Phys. Lett.* 93.19 (2008), p. 192914.
- [131] J. E. Spanier, A. M. Kolpak, J. J. Urban, I. Grinberg, L. Ouyang, W. S. Yun, A. M. Rappe, and H. Park. “Ferroelectric phase transition in individual single-crystalline BaTiO<sub>3</sub> nanowires”. In: *Nano Letters* 6.4 (2006), pp. 735–739.
- [132] R. Böttcher, C. Klimm, D. Michel, H.-C. Semmelhack, G. Völkel, H.-J. Gläsel, and E. Hartmann. “Size effect in Mn<sup>2+</sup>-doped BaTiO<sub>3</sub> nanopowders observed by electron paramagnetic resonance”. In: *Phys. Rev. B* 62.3 (2000), p. 2085.
- [133] W. Zhong, Y. Wang, P. Zhang, and B. Qu. “Phenomenological study of the size effect on phase transitions in ferroelectric particles”. In: *Phys. Rev. B* 50.2 (1994), p. 698.
- [134] B. Jiang and L. Bursill. “Phenomenological theory of size effects in ultrafine ferroelectric particles of lead titanate”. In: *Phys. Rev. B* 60.14 (1999), p. 9978.
- [135] J. Slater. “The Lorentz correction in barium titanate”. In: *Phys. Rev.* 78.6 (1950), p. 748.
- [136] P. Chandra and P. B. Littlewood. “A Landau primer for ferroelectrics”. In: *Physics of ferroelectrics*. Springer, 2007, pp. 69–116.
- [137] W. Sun. “Size effect in barium titanate powders synthesized by different hydrothermal methods”. In: *J. Appl. Phys.* 100.8 (2006), p. 083503.
- [138] D. Tilley and B. Žekš. “Landau theory of phase transitions in thick films”. In: *Solid State Commun.* 49.8 (1984), pp. 823–828.
- [139] K. Ishikawa, T. Nomura, N. Okada, and K. Takada. “Size effect on the phase transition in PbTiO<sub>3</sub> fine particles”. In: *Jpn. J. Appl. Phys.* 35.9S (1996), p. 5196.
- [140] D. Y. Murzin. “Nanokinetics for nanocatalysis”. In: *Catal. Sci. Technol.* 1.3 (2011), pp. 380–384.
- [141] V. N. Parmon. “Thermodynamic analysis of the effect of the nanoparticle size of the active component on the adsorption equilibrium and the rate of heterogeneous catalytic processes”. In: *Dokl. Phys. Chem.* 413.1 (2007), pp. 42–48.
- [142] D. Y. Murzin. “Thermodynamic analysis of nanoparticle size effect on catalytic kinetics”. In: *Chem. Eng. Sci.* 64.5 (2009), pp. 1046–1052.

- [143] C. Su, Y. Otsuka, C. Huang, D. Hennings, C. Pithan, F. Shiao, and R. Waser. "Grain growth and crystallinity of ultrafine barium titanate particles prepared by various routes". In: *Ceram. Inter.* 39.6 (2013), pp. 6673–6680.
- [144] K. Uchino, E. Sadanaga, and T. Hirose. "Dependence of the crystal structure on particle size in barium titanate". In: *J. Am. Ceram. Soc.* 72.8 (1989), pp. 1555–1558.
- [145] G. Canu and V. Buscaglia. "Hydrothermal synthesis of strontium titanate: thermodynamic considerations, morphology control and crystallisation mechanisms". In: *CrysEngComm* 19.28 (2017), pp. 3867–3891.
- [146] S. Farhadi, Z. Momeni, and M. Taherimehr. "Rapid synthesis of perovskite-type LaFeO<sub>3</sub> nanoparticles by microwave-assisted decomposition of bimetallic La [Fe(CN)<sub>6</sub>]· 5H<sub>2</sub>O compound". In: *J. Alloys Compds.* 471.1-2 (2009), pp. L5–L8.
- [147] V. Mikrovalov. "Microwave-assisted non-aqueous synthesis of ZnO nanoparticles". In: *Materiali in Tehnologije* 45.3 (2011), pp. 173–177.
- [148] S. H. Jhung, J.-S. Chang, J. S. Hwang, and S.-E. Park. "Selective formation of SAPO-5 and SAPO-34 molecular sieves with microwave irradiation and hydrothermal heating". In: *Micro. Meso. Mater.* 64.1-3 (2003), pp. 33–39.
- [149] S. H. Jhung, T. Jin, Y. K. Hwang, and J.-S. Chang. "Microwave effect in the fast synthesis of microporous materials: which stage between nucleation and crystal growth is accelerated by microwave irradiation?" In: *Chem.-A Europ. J.* 13.16 (2007), pp. 4410–4417.
- [150] L. A. Bloomfield. *How things work*. Louis A. Bloomfield., 2001.
- [151] M. Vollmer. "Physics of the microwave oven". In: *Phys. Education* 39.1 (2004), p. 74.
- [152] K. Parker and M. Vollmer. "Bad food and good physics: the development of domestic microwave cookery". In: *Phys. Education* 39.1 (2004), p. 82.
- [153] B. D. Cullity and S. R. Stock. *Elements of X-ray diffraction*. Vol. 3. Prentice hall New Jersey, 2001.
- [154] G. S. Bumrah and R. M. Sharma. "Raman spectroscopy–Basic principle, instrumentation and selected applications for the characterization of drugs of abuse". In: *Egyptian J. Forensic Sci.* 6.3 (2016), pp. 209–215.

- [155] F. A. Settle. *Handbook of instrumental techniques for analytical chemistry*. Prentice Hall PTR, 1997.
- [156] D. A. Skoog, F. J. Holler, and S. R. Crouch. *Principles of instrumental analysis*. Cengage learning, 2017.
- [157] D. Cialla-May, M. Schmitt, and J. Popp. “Theoretical principles of Raman spectroscopy”. In: *Phys. Sci. Rev.* 4.6 (2019), pp. 1–9.
- [158] E. Smith and G. Dent. *Modern Raman spectroscopy: a practical approach*. Wiley, 2019.
- [159] B. Schrader. *Infrared and Raman spectroscopy: methods and applications*. John Wiley & Sons, 2008.
- [160] J. Chastain. “Handbook of X-ray photoelectron spectroscopy”. In: *Perkin-Elmer Corporation* 40 (1992), p. 221.
- [161] J. Kawai, H. Adachi, Y. Kitajima, K. Maeda, S. Hayakawa, and Y. Gohshi. “Inelastic mean free path of photoelectrons in Ag determined by total reflection X-ray photoelectron spectroscopy”. In: *Anal. Sci.* 13.5 (1997), pp. 797–801.
- [162] C. Crowell. “The Richardson constant for thermionic emission in Schottky barrier diodes”. In: *Solid-State Electronics* 8.4 (1965), pp. 395–399.
- [163] R. F. Egerton. *Physical principles of electron microscopy*. Springer, 2005.
- [164] N. J. Hogan, A. S. Urban, C. Ayala-Orozco, A. Pimpinelli, P. Nordlander, and N. J. Halas. “Nanoparticles heat through light localization”. In: *Nano Lett.* 14.8 (2014), pp. 4640–4645.
- [165] G. Gauglitz and T. Vo-Dinh. *Handbook of spectroscopy*. Vol. 1. Wiley Online Library, 2003.
- [166] V. P. Pavlovic, M. V. Nikolic, V. B. Pavlovic, J. Blanusa, S. Stevanovic, V. V. Mitic, M. Scepanovic, and B. Vlahovic. “Raman responses in mechanically activated BaTiO<sub>3</sub>”. In: *J. Am. Ceram. Soc.* 97.2 (2014), pp. 601–608.
- [167] K. C. Verma, V. Gupta, J. Kaur, and R. Kotnala. “Raman spectra, photoluminescence, magnetism and magnetoelectric coupling in pure and Fe doped BaTiO<sub>3</sub> nanostructures”. In: *J. Alloys Compd.* 578 (2013), pp. 5–11.

- [168] G. M. Osoro, D. Bregiroux, M. P. Thi, and F. Levassort. “Structural and piezoelectric properties evolution induced by cobalt doping and cobalt/niobium co-doping in BaTiO<sub>3</sub>”. In: *Mater. Lett.* 166 (2016), pp. 259–262.
- [169] G. Pezzotti. “Raman spectroscopy of piezoelectrics”. In: *J. Appl. Phys.* 113.21 (2013), pp. 1–78.
- [170] Y. Shiratori, C. Pithan, J. Dornseiffer, and R. Waser. “Raman scattering studies on nanocrystalline BaTiO<sub>3</sub> Part IaIsolated particles and aggregates”. In: *J. Raman Spectrosc.* 38.10 (2007), pp. 1288–1299.
- [171] K.-R. Zhu, M.-S. Zhang, Q. Chen, and Z. Yin. “Size and phonon-confinement effects on low-frequency Raman mode of anatase TiO<sub>2</sub> nanocrystal”. In: *Phys. Lett. A* 340.1-4 (2005), pp. 220–227.
- [172] J. Mougin, N. Rosman, G. Lucaleau, and A. Galerie. “In situ Raman monitoring of chromium oxide scale growth for stress determination”. In: *J. Raman Spectrosc.* 32.9 (2001), pp. 739–744.
- [173] S. Jayanthi and T. Kutty. “Dielectric properties of 3d transition metal substituted BaTiO<sub>3</sub> ceramics containing the hexagonal phase formation”. In: *J. Mater. Sci.: Mater. Electrons.* 19.7 (2008), pp. 615–626.
- [174] H. M. Nguyen, N. Dang, P.-Y. Chuang, T. Thanh, C.-W. Hu, T.-Y. Chen, V. Lam, C.-H. Lee, and L. Hong. “Tetragonal and hexagonal polymorphs of BaTi<sub>1-x</sub>Fe<sub>x</sub>O<sub>3-δ</sub> multiferroics using x-ray and Raman analyses”. In: *Appl. Phys. Lett.* 99.20 (2011), p. 202501.
- [175] A. Rani, J. Kolte, and P. Gopalan. “Phase formation, microstructure, electrical and magnetic properties of Mn substituted barium titanate”. In: *Ceram. Int.* 41.10 (2015), pp. 14057–14063.
- [176] I. C. Amaechi, A. Hadj Youssef, D. Rawach, J. P. Claverie, S. Sun, and A. Ruediger. “Ferroelectric Fe–Cr co-doped BaTiO<sub>3</sub> nanoparticles for the photocatalytic oxidation of azo dyes”. In: *ACS Appl. Nano Mater.* 2.5 (2019), pp. 2890–2901.
- [177] J. Baniecki, M. Ishii, T. Shioga, K. Kurihara, and S. Miyahara. “Surface core-level shifts of strontium observed in photoemission of barium strontium titanate thin films”. In: *Appl. Phys. Lett.* 89.16 (2006), p. 162908.

- [178] T.-C. Lin, G. Seshadri, and J. A. Kelber. “A consistent method for quantitative XPS peak analysis of thin oxide films on clean polycrystalline iron surfaces”. In: *Appl. Surf. Sci.* 119.1-2 (1997), pp. 83–92.
- [179] M. C. Biesinger, B. P. Payne, A. P. Grosvenor, L. W. Lau, A. R. Gerson, and R. S. C. Smart. “Resolving surface chemical states in XPS analysis of first row transition metals, oxides and hydroxides: Cr, Mn, Fe, Co and Ni”. In: *Appl. Surf. Sci.* 257.7 (2011), pp. 2717–2730.
- [180] S. Södergren, H. Siegbahn, H. Rensmo, H. Lindström, A. Hagfeldt, and S.-E. Lindquist. “Lithium intercalation in nanoporous anatase TiO<sub>2</sub> studied with XPS”. In: *J. Phys. Chem. B* 101.16 (1997), pp. 3087–3090.
- [181] H. J. Kim, J. Kim, and B. Hong. “Effect of hydrogen plasma treatment on nanostructured TiO<sub>2</sub> films for the enhanced performance of dye-sensitized solar cell”. In: *Appl. Surf. Sci.* 274 (2013), pp. 171–175.
- [182] I. C. Amaechi, G. Kolhatkar, A. H. Youssef, D. Rawach, S. Sun, and A. Ruediger. “B-site modified photoferroic Cr<sup>3+</sup>-doped barium titanate nanoparticles: microwave-assisted hydrothermal synthesis, photocatalytic and electrochemical properties”. In: *RSC Adv.* 9.36 (2019), pp. 20806–20817.
- [183] R. J. Martín-Palma, J. Martínez-Duart, and F. Agulló-Rueda. *Nanotechnology for microelectronics and optoelectronics*. Elsevier, 2006.
- [184] H. Langhammer, T. Müller, R. Böttcher, and H. Abicht. “Structural and optical properties of chromium-doped hexagonal barium titanate ceramics”. In: *J. Phys.: Condens. Matter* 20.8 (2008), p. 085206.
- [185] S. Eden, S. Kapphan, H. Hesse, V. Trepakov, V. Vikhnin, I. Gregora, L. Jastrabik, and J. Seglins. “Observations of the absorption, infra-red emission, and excitation spectra of Cr in BaTiO<sub>3</sub>”. In: *J. Phys.: Condens. Matter* 10.47 (1998), p. 10775.
- [186] M. Hoque, M. I. Guzman, et al. “Photocatalytic activity: experimental features to report in heterogeneous photocatalysis”. In: *Materials* 11.10 (2018), p. 1990.
- [187] D. F. Ollis. “Kinetic disguises in heterogeneous photocatalysis”. In: *Topics Catal.* 35.3-4 (2005), pp. 217–223.

- [188] D. Li, R. Shi, C. Pan, Y. Zhu, and H. Zhao. “Influence of ZnWO<sub>4</sub> nanorod aspect ratio on the photocatalytic activity”. In: *Cryst. Eng. Comm.* 13.14 (2011), pp. 4695–4700.
- [189] X. Zhang, J. Qin, Y. Xue, P. Yu, B. Zhang, L. Wang, and R. Liu. “Effect of aspect ratio and surface defects on the photocatalytic activity of ZnO nanorods”. In: *Sci. Rep.* 4 (2014), p. 4596.
- [190] A. M. Braun and E. Oliveros. “How to evaluate photochemical methods for water treatment”. In: *Water Sci. Technol.* 35.4 (1997), p. 17.
- [191] J. Li, M. Jiang, H. Zhou, P. Jin, K. M. Cheung, P. K. Chu, and K. W. Yeung. “Vanadium dioxide nanocoating induces tumor cell death through mitochondrial electron transport chain interruption”. In: *Global Challenges* 3.3 (2019), p. 1800058.
- [192] M. d. C. B. López, G. Fourlaris, B. Rand, and F. L. Riley. “Characterization of barium titanate powders: barium carbonate identification”. In: *J. Am. Ceram. Soc.* 82.7 (1999), pp. 1777–1786.
- [193] M. M. Lencka and R. E. Riman. “Thermodynamic modeling of hydrothermal synthesis of ceramic powders”. In: *Chem. Mater.* 5.1 (1993), pp. 61–70.
- [194] B. Jaffe. *Piezoelectric ceramics*. Vol. 3. Elsevier, 2012.
- [195] L. Yang, Y. Choi, W. Qin, H. Chen, K. Blinn, M. Liu, P. Liu, J. Bai, T. A. Tyson, and M. Liu. “Promotion of water-mediated carbon removal by nanostructured barium oxide/nickel interfaces in solid oxide fuel cells”. In: *Nat. Commun.* 2.1 (2011), pp. 1–9.
- [196] M. Wittels and F. Sherrill. “Fast neutron effects in tetragonal barium titanate”. In: *J. Appl. Phys.* 28.5 (1957), pp. 606–609.
- [197] A. Rüdiger, T. Schneller, A. Roelofs, S. Tiedke, T. Schmitz, and R. Waser. “Nanosize ferroelectric oxides—tracking down the superparaelectric limit”. In: *Appl. Phys. A* 80.6 (2005), pp. 1247–1255.
- [198] T.-C. Huang, M.-T. Wang, H.-S. Sheu, and W.-F. Hsieh. “Size-dependent lattice dynamics of barium titanate nanoparticles”. In: *J. Phys.: Condens. Matter* 19.47 (2007), p. 476212.

- [199] M. B. Smith, K. Page, T. Siegrist, P. L. Redmond, E. C. Walter, R. Seshadri, L. E. Brus, and M. L. Steigerwald. “Crystal structure and the paraelectric-to-ferroelectric phase transition of nanoscale BaTiO<sub>3</sub>”. In: *J. Am. Chem. Soc.* 130.22 (2008), pp. 6955–6963.
- [200] M. Moreira, G. Mambrini, D. Volanti, E. Leite, M. Orlandi, P. Pizani, V. Mastelaro, C. Paiva-Santos, E. Longo, and J. A. Varela. “Hydrothermal microwave: a new route to obtain photoluminescent crystalline BaTiO<sub>3</sub> nanoparticles”. In: *Chem. Mater.* 20.16 (2008), pp. 5381–5387.
- [201] U. D. Venkateswaran, V. M. Naik, and R. Naik. “High-pressure Raman studies of polycrystalline BaTiO<sub>3</sub>”. In: *Phys. Rev. B* 58.21 (1998), p. 14256.
- [202] D. Tenne, A. Bruchhausen, N. Lanzillotti-Kimura, A. Fainstein, R. Katiyar, A. Cantarero, A. Soukiassian, V. Vaithyanathan, J. Haeni, W. Tian, et al. “Probing nanoscale ferroelectricity by ultraviolet Raman spectroscopy”. In: *Science* 313.5793 (2006), pp. 1614–1616.
- [203] Z. Zhao, V. Buscaglia, M. Viviani, M. T. Buscaglia, L. Mitoseriu, A. Testino, M. Nygren, M. Johnsson, and P. Nanni. “Grain-size effects on the ferroelectric behavior of dense nanocrystalline BaTiO<sub>3</sub> ceramics”. In: *Phys. Rev. B* 70.2 (2004), p. 024107.
- [204] I. Grinberg, D. V. West, M. Torres, G. Gou, D. M. Stein, L. Wu, G. Chen, E. M. Gallo, A. R. Akbashev, P. K. Davies, et al. “Perovskite oxides for visible-light-absorbing ferroelectric and photovoltaic materials”. In: *Nature* 503.7477 (2013), pp. 509–512.
- [205] Y. Ni, H. Zheng, N. Xiang, K. Yuan, and J. Hong. “Simple hydrothermal synthesis and photocatalytic performance of coral-like BaTiO<sub>3</sub> nanostructures”. In: *RSC Adv.* 5.10 (2015), pp. 7245–7252.
- [206] Y. Kayanuma. “Quantum-size effects of interacting electrons and holes in semiconductor microcrystals with spherical shape”. In: *Phys. Rev. B* 38.14 (1988), p. 9797.
- [207] N. Serpone, D. Lawless, R. Khairutdinov, and E. Pelizzetti. “Subnanosecond relaxation dynamics in TiO<sub>2</sub> colloidal sols (particle sizes Rp= 1.0-13.4 nm). Relevance to heterogeneous photocatalysis”. In: *J. Phys. Chem.* 99.45 (1995), pp. 16655–16661.
- [208] A. Barnard and L. Curtiss. “Prediction of TiO<sub>2</sub> nanoparticle phase and shape transitions controlled by surface chemistry”. In: *Nano Lett.* 5.7 (2005), pp. 1261–1266.

- [209] G. L. Bezemer, J. H. Bitter, H. P. Kuipers, H. Oosterbeek, J. E. Holewijn, X. Xu, F. Kapteijn, A. J. van Dillen, and K. P. de Jong. “Cobalt particle size effects in the Fischer-Tropsch reaction studied with carbon nanofiber supported catalysts”. In: *J. Am. Chem. Soc.* 128.12 (2006), pp. 3956–3964.
- [210] M. Temkin. “The kinetics of some industrial heterogeneous catalytic reactions”. In: *Advances in Catalysis*. Vol. 28. Elsevier, 1979, pp. 173–291.
- [211] K. Uchino, N.-Y. Lee, T. Toba, N. Usuki, H. Aburatani, and Y. Ito. “Changes in the crystal structure of RF-magnetron sputtered BaTiO<sub>3</sub> thin films”. In: *Jpn. J. Ceram. Soc.* 100.1165 (1992), pp. 1091–1093.
- [212] HealthCanada. *Guidelines for Canadian drinking water quality: Guideline technical document à Manganese*. (Accessed October 4, 2020). URL: <https://www.canada.ca/content/dam/hc-sc/documents/services/publications/healthy-living/guidelines-canadian-drinking-water-quality-guideline-technical-document-manganese/pub-manganese-0212-2019-eng.pdf>.
- [213] H. Matsuo, Y. Kitanaka, R. Inoue, Y. Noguchi, and M. Miyayama. “Heavy Mn-doping effect on spontaneous polarization in ferroelectric BiFeO<sub>3</sub> thin films”. In: *Jpn. J. Appl. Phys.* 54.10S (2015), 10NA03.
- [214] H. Matsuo, Y. Noguchi, and M. Miyayama. “Gap-state engineering of visible-light-active ferroelectrics for photovoltaic applications”. In: *Nature Commun.* 8.1 (2017), pp. 1–8.
- [215] R. G. Pearson. “Absolute electronegativity and hardness: application to inorganic chemistry”. In: *Inorg. Chem.* 27.4 (1988), pp. 734–740.
- [216] Y.-J. Jiang, L.-Z. Zeng, R.-P. Wang, Y. Zhu, and Y.-L. Liu. “Fundamental and Second-Order Raman Spectra of BaTiO<sub>3</sub>”. In: *J. Raman Spectrosc.* 27.1 (1996), pp. 31–34.
- [217] M. Si, Y. Kang, and Z. Zhang. “Surface-enhanced Raman scattering (SERS) spectra of Methyl Orange in Ag colloids prepared by electrolysis method”. In: *Appl. Surf. Sci.* 255.11 (2009), pp. 6007–6010.
- [218] S. Burikov, T. Dolenko, S. Patsaeva, Y. Starokurov, and V. Yuzhakov. “Raman and IR spectroscopy research on hydrogen bonding in water–ethanol systems”. In: *Molecular Phys.* 108.18 (2010), pp. 2427–2436.

- [219] C. Hu, C. Y. Jimmy, Z. Hao, and P. K. Wong. "Photocatalytic degradation of triazine-containing azo dyes in aqueous TiO<sub>2</sub> suspensions". In: *Appl. Catal. B: Environ.* 42.1 (2003), pp. 47–55.
- [220] I. K. Konstantinou and T. A. Albanis. "TiO<sub>2</sub>-assisted photocatalytic degradation of azo dyes in aqueous solution: kinetic and mechanistic investigations: a review". In: *Appl. Catal. B: Environ.* 49.1 (2004), pp. 1–14.
- [221] H. Lee, Y.-K. Park, S.-J. Kim, B.-H. Kim, H.-S. Yoon, and S.-C. Jung. "Rapid degradation of methyl orange using hybrid advanced oxidation process and its synergistic effect". In: *J. Ind. Eng. Chem.* 35 (2016), pp. 205–210.
- [222] W. Hertl. "Kinetics of barium titanate synthesis". In: *J. Am. Ceram. Soc.* 71.10 (1988), pp. 879–883.



# Résumé en Français

## 1.1 Introduction

Selon les Nations unies (ONU), l'un des besoins fondamentaux de l'homme est l'eau. Malheureusement, l'augmentation constante de la population, associée à l'industrialisation non seulement pressurisée, mais aussi a limité les ressources disponibles en eau. Le degré de pollution peut être déterminé par diverses activités anthropiques et parfois géogéniques. La décharge de produits qui contiennent des colorants, des pigments, des pesticides, des produits pharmaceutiques, etc. dans les masses d'eau sont considérée dangereuse et rend l'eau impropre à la consommation. Cela met même plus en danger la vie de toutes les espèces aquatiques organismes [1]. En d'autres termes, la pollution de l'eau est devenue un défi mondial majeur qui nécessite d'être surmontée. À cet égard, des technologies de traitement existent et comprennent des procédés chimiques [2], électrochimiques [3], de filtration membranaire, biologiques et la catalytiques [4]. La catalyse, qui est largement utilisée dans les grandes stations d'épuration centralisées, utilise essentiellement un matériau semi-conducteur (c'est-à-dire un catalyseur) pour accélérer une réaction chimique par la turbocharge du processus chimique afin de rompre les liaisons de structures chimiques complexes [1]. Cependant, l'utilisation intensive de l'énergie et la chimie joue sur la technologie. Du côté de la chimie (catalyseur), la réduction du temps et du coût du traitement a toujours été les facteurs clés du développement industriel de nouveaux catalyseurs performants. Pour de nombreux procédés catalytiques industriels, les métaux nobles ont souvent été utilisés en raison de leur forte activité catalytique, de leur stabilité chimique et même de leur résistance à la photocorrosion. Le coût semble être le principal facteur qui pousse à renoncer à l'utilisation des métaux nobles. Pour avoir un guide sur le coût de ces catalyseurs, nous allons présenter des chiffres de références. Récemment, le prix de l'or (Au) a sensiblement augmenté (au moment de la

rédaction du présent document) pour atteindre 62,36 \$/gramme, celui du platine (Pt) est de 29,14 \$/gramme, iridium (Ir) est de 52,89 \$/gramme, rhodium (Rh) est de 398,67 \$/gramme, et le palladium (Pd) est de 75,65 \$/gramme, respectivement. [5], cette augmentation est due surtout à la demande croissante des catalyseurs. Par exemple, dans le processus catalytique menant à la production de silicium durcis, les catalyseurs à base de platine sont utilisés et jusqu'à 4 à 6 tonnes de catalyseur sont consommés dans le processus chaque année [6]. Cela se traduit par 117 à 175 millions de dollars qui est un coût énorme. Par conséquent, pour rendre la catalyse durable, il est important de développer un nouveau catalyseur moins cher, mais surtout performant. Les matériaux abondants sur terre, tels que les métaux de transition (MT), sont  $\sim 10^4$  fois plus nombreux que les métaux nobles et présentent également des activités catalytiques prometteuses [7]. En d'autres termes, la transition de catalyseurs à base de métaux nobles à des catalyseurs à base de matériaux abondants permettra de réduire le coût des produits chimiques utilisés dans la catalyse.

On ne peut pas exclure complètement que chacune des technologies de traitement présentent des potentiels dans la dépollution des eaux contaminées, les inconvénients tendent à compromettre leur déploiement et l'applicabilité, en particulier dans les régions éloignées où les maladies liées à la pollution de l'eau sont en hausse. Dans le but de décentraliser les installations conventionnelles de traitement de l'eau, une technologie abordable et durable est nécessaire. La photocatalyse apparaît comme une option. Elle est une technologie verte et son activité repose sur les principes des procédés d'oxydation avancée (AOP) en raison de l'abondance de la lumière du soleil. Après la photoélectrolyse de l'eau en produisent de l'hydrogène en utilisant du TiO<sub>2</sub> monocristallin en 1972 [8], la photocatalyse a pris un développement progressif. Bien que son utilisation pour la production d'hydrogène ait présenté un inconvénient notable, l'exploitation de son pouvoir oxydant a été démontrée plus tard par l'oxydation du polluant industriel, le cyanure en 1977 [9]. Néanmoins, il a été observé que TiO<sub>2</sub> est limité par ces facteurs, mais sans s'y limiter ces facteurs, à savoir: (i) une large bande d'énergie - l'absorption intrinsèque est dans l'ultraviolet (UV) qui ne représente que 3 à 5% du spectre solaire [12, 13] (voir la 1.1) ; (ii) taux de recombinaison élevé- il souffre d'un faible rendement quantique dû à un mauvais porteur de charge séparation [14].

Le dopage non métallique/métallique et les hétérojonctions ont fait partie des stratégies visant à améliorer l'absorption de la lumière et les propriétés catalytiques du TiO<sub>2</sub>. Le dopage des métaux, en particulier avec des matériaux plasmoniques tels que l'argent (Ag), l'or (Au),

le cuivre (Cu), etc. se sont avérés efficaces, car les électrons excités dans la conduction peuvent facilement être attirés par les particules métalliques en raison la différence dans la fonction de travail entre le métal et le TiO<sub>2</sub>. En plus de leurs rôles comme piégeur d'électrons pour augmenter la séparation des paires électron-trou lors de la photogénération, les métaux plasmonique présentent un effet de résonance du plasmon de surface (RSP) qui, à son tour, améliore leur activité catalytique.

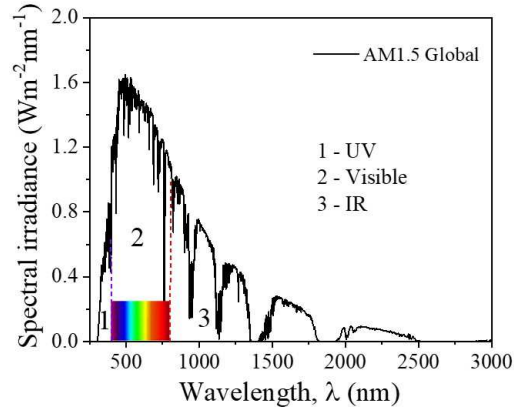


Figure 1.1: Spectre d'irradiation solaire à la masse de l'air 1,5 (AM1,5).

L'effet SPR résulte d'un couplage électromagnétique entre la lumière incidente et les électrons de conduction oscillants, qui aboutissent à une amplification du champ électromagnétique près de la surface du matériau plasmonique [15]. En particulier, Ag et Au présentent un fort pic d'absorption de SPR dans la région visible, ce qui leur donne l'avantage d'être de bons candidats pour la photocatalyse actifs à la lumière visible. Par exemple, l'évaluation photocatalytique effectuée à l'aide des photocatalyseurs plasmoniques Au:TiO<sub>2</sub> [16] et Ag:TiO<sub>2</sub> [17] ont montré des signes de photocatalyse plus élevés que le TiO<sub>2</sub> pur. Cela montre que les métaux nobles chargés en TiO<sub>2</sub> fournissent une activité synergique grâce à un ancien processus de transfert d'électrons. Cependant, la dégradation des constantes de vitesse de Au:TiO<sub>2</sub> ( $0,0241 \text{ min}^{-1}$ ) et Ag:TiO<sub>2</sub> ( $0,0041 \text{ min}^{-1}$ ) pour la réaction du premier ordre semble être plus faible que celle d'un matériau non centrosymétrique tel que le BaTiO<sub>3</sub> ( $0,032 \pm 0,003 \text{ min}^{-1}$ ) [18]. Cela peut être attribué à la séparation des transporteurs de charges supplémentaires par le biais de l'énergie photovoltaïque du bulk, qui sera examinée en détail dans le chapitre .

Sur le plan nanotechnologique, les progrès récents en photocatalyse sont beaucoup plus basés sur la conception des matériaux. Les activités de certains de ces matériaux semblent rivaliser avec des problématiques telles que le fait que les propriétés des matériaux et la ciné-

tique n'ont pas été prises en considération [1, 19]. Pour surmonter ces défis, un matériau avec une amplification importante de la section efficace de la photo-absorption, une capacité d'adsorption et des charges de surface localisées seront considérées comme prometteuses. Ceci peut constituer un paramètre de conception dans la fabrication de nouveaux matériaux fonctionnels. Le titanate de baryum,  $\text{BaTiO}_3$  avec la structure de pérovskite ( $A^{2+}B^{4+}O_3^{2-}$ ) est un matériel intéressant et présente un mécanisme de déplacement du courant connu sous le nom de l'effet photovoltaïque du bulk (BPVE). La longue gamme de champ électrique à la surface contribue à la séparation des porteurs de charge, en particulier pour la configuration non-centrosymétrique du matériau [20]. Comme pour la bande interdite de la forme anatase de  $\text{TiO}_2$ , il présente un bord d'absorption à 390 nm [21] et peut être considéré comme un système de couches de  $\text{BaO}$  et de  $\text{TiO}_2$  le long de (001), présentant les propriétés catalytiques. Techniquement, l'extension de la photosensibilité du  $\text{BaTiO}_3$  écologique par le dopage n'est pas nouveau, mais l'exploitation des charges de surface localisées qui ont culminé de BPVE et garde la promesse d'améliorer les propriétés de transport de charge du matériau, qui est entièrement avantageux pour les applications photocatalytiques.

## 1.2 Objectifs de recherche

Les objectifs généraux de la thèse sont les suivants : (1) utiliser l'ingénierie de bande interdite pour fabriquer le  $\text{BaTiO}_3$  pyroélectrique et actif dans lumière visible, et (2) d'étudier l'effet de la variation de la taille des particules sur la cinétique de la photocatalyse et le transport de masse du  $\text{BaTiO}_3$  pyroélectrique. Pour réaliser ces principaux objectifs: nous avons défini des objectifs spécifiques:

- ◊ Utiliser la technique hydrothermique modulable assistée par micro-ondes pour la synthèse de nanoparticules de titanate de baryum pyroélectrique actives dans la lumière visible.
- ◊ Comprendre l'effet du chrome dans les nanoparticules de titanate de baryum dopées au Cr.
- ◊ Remplacer le chrome par le non toxique fer (Fe) dans les nanoparticules de titanate de baryum dopées au Cr et étudier leurs potentiels pour la restauration de l'environnement.
- ◊ Comprendre l'interaction entre la taille des particules et l'effet photovoltaïque global responsable pour la séparation des porteurs de charge induite par la polarisation dans le

$\text{BaTiO}_3$  dans sa phase tétragonale.

## 2.1 Considération théorique

Le modèle phénoménologique de Landau-Ginzburg-Devonshire (LGD) exprime l'énergie libre de Gibbs en tant que fonction de puissance en série qui dépend de la taille des particules,  $x$ , de la température,  $T$  et paramètre d'ordre, dans ce cas la polarisation spontanée,  $P$  [133]

$$G(x, T, P) = G_0 + \frac{1}{2} \int \left( \alpha_0(T - T_C)P^2 + \frac{1}{2}\beta P^4 + \frac{1}{3}\gamma P^6 + \phi(\nabla P)^2 \right) dV + \frac{\phi}{2\delta} \int P^2 dS \quad (2.1)$$

où  $\alpha = \alpha_0(T - T_C)$ ,  $\beta$ ,  $\gamma$ ,  $\phi$  et  $\delta$  sont tous des paramètres matériels, et  $G_0$  est énergie libre résiduelle de la phase cubique désordonnée à haute température. La cinétique et l'interaction moléculaire particulièrement à l'interface catalyseur-liquide, sont complexes pour un photocatalyseur en phase liquide hétérogène et le modèle thermodynamique est essentiellement utilisé pour décrire l'impact de la taille des particules [141]. Dans une telle situation, le potentiel chimique est utilisé pour décrire le système pour le changement de l'énergie libre. En d'autres termes, remplacer le potentiel chimique par l'énergie libre de Gibbs, ce qui est le cas à température et pression constantes, l'énergie libre de Gibbs peut donc être réécrit comme [142]

$$G(x, T, P) = G(\infty) + \Delta G(x, T, P) \quad (2.2)$$

Pour une réaction d'oxydoréduction dans laquelle il y a une compétition entre la première et l'espèce intermédiaire au cours de la dégradation, le taux de réaction dépendant de la taille,  $R(x)$ , qui est exprimé comme suit [142]

$$k(x) = \frac{k_3 K_1 C_X K_2 C_Y \exp\left(\frac{-2\alpha\eta}{x}\right)}{\left(1 + (K_1 C_X + K_2 C_Y) \exp\left(\frac{-\eta}{x}\right)\right)^2} \quad (2.3)$$

où  $K_{1/2}$  sont les constantes d'adsorption d'équilibre,  $k_3$  est la constante d'adsorption de Langmuir,  $C_{X/Y}$  sont la concentration de X/Y dans la phase liquide,  $\alpha$  est le paramètre de Polanyi. Équation 2.3 peut être encore simplifiée lorsque la vitesse de réaction par unité de poids de la surface est considéré, donc  $k'(x)$  devient

$$k'(x) = k(x) \cdot A_{surface} = \frac{k_3 K_1 C_X K_2 C_Y \exp\left(\frac{-2\alpha\eta}{x}\right)}{\left(1 + (K_1 C_X + K_2 C_Y) \exp\left(\frac{-\eta}{x}\right)\right)^2} \frac{3}{x\rho} = \frac{A' \exp\left(\frac{-2\alpha\eta}{x}\right)}{\left(1 + A'' \exp\left(\frac{-\eta}{x}\right)\right)^2} \frac{1}{x} \quad (2.4)$$

où  $A' = \frac{3k_3K_1C_XK_2C_Y}{\rho}$ ,  $A'' = K_1C_X + K_2C_Y$ , et  $\rho$  est la densité du photocatalyseur ( $6020 \text{ kg/m}^3$  pour le BaTiO<sub>3</sub> [143]). Les équations 2.2 et 2.4 sont techniquement identiques. De plus,  $\eta = 2\sigma V_M/RT$  a la dimension de la taille des particules et dépend de la tension superficielle,  $\sigma$  de la particule, comme dans l'équation 3 de Uchino et al. [144].  $V_M$ ,  $R$ , et  $T$  sont le volume molaire ( $\text{m}^3 \text{ mol}^{-1}$ ), la constante universelle des gaz ( $8,314 \text{ JK}^{-1} \text{ mol}^{-1}$ ) et la température (K). Alors que le préfacteur dans l'équation 2.4 tient compte de la perte du taux de dégradation pour les particules très petites et la dépendance inverse sur  $x$  peut-être visibles sur les larges particules.

## 2.2 Méthodologie

### 2.2.1 Préparation de nanoparticules pyroélectriques de BaTiO<sub>3</sub>

Pour la synthèse de ces échantillons, la méthode hydrothermale assistée par micro-ondes a été utilisée. Il existe deux sources de titane : (i) l'anatase TiO<sub>2</sub> disponible dans le commerce, et (ii) le TiO<sub>2</sub> obtenu par l'intermédiaire de l'alkoxyde de titane. Pour poursuivre le premier objectif de ce projet de recherche, Le TiO<sub>2</sub> commercialement disponible a été utilisé pour la synthétiser du titanate de baryum photo-pyroélectrique, tandis que le TiO<sub>2</sub> a obtenu par l'alkoxyde de titane a été utilisé dans la synthèse du titanate de baryum utilisé pour l'étude de l'effet de la taille des particules sur la cinétique et le transport de masse du photocatalyseur.

Dans le premier cas, 50 mmol de la poudre commerciale de TiO<sub>2</sub> ont été dispersés dans 10 mL d'eau sous agitation magnétique constante à température ambiante. 75 mmol de hydroxyde de baryum octahydraté est ajouté, suivi de 5,2 mmol de nitrate de chrome (III) nonahydraté et de 2,6 mmol de nitrate de fer (III) nonahydraté. Alors que la concentration molaire de l'ion chrome a été maintenue à 4 mol% dans des conditions optimisées, celle de l'ion fer a été variable (c'est-à-dire 0, 4 et 8 mol%). 2 mL de peroxyde d'hydrogène est alors ajouté après 20 min d'agitation magnétique constante. Après 10 min d'agitation, le mélange a été transféré dans un récipient de Teflon logé dans un autoclave de polymère transparent aux micro-ondes (de Parr Instrument). L'ensemble fermé a ensuite été placé à l'intérieur Four à micro-ondes d'un onduleur Panasonic (2,45 GHz) fonctionnant à 120 W pendant 10 min. Le réacteur a été laissé refroidir pendant 2 h après l'exposition initiale aux micro-ondes (pour éviter la surpression), et le processus est répété pour deux autres cycles en utilisant les mêmes conditions de chauffage. Le produit est lavé à l'eau distillée plusieurs fois, filtré et séché au

four à 80 °C pendant 15 h. Les échantillons non dopés ont été préparés de la même manière, sans ajout de MT.

Dans le second cas, 50 mmol de butoxyde de titane et 5 mL d'éthanol ont été mélangés. Après 10 min d'agitation magnétique constante, 75 mmol de hydroxyde de baryum octahydraté dissous dans 5 mL d'eau distillée préchauffé (> 90 °C) qui a été ensuite ajoutée au mélange précédent en présence de 2 mL de peroxyde d'hydrogène. Le polyéthylène glycol (PEG, mol. wt. = 8000) a été ajouté par la suite afin de moduler la taille des particules. Les tailles de particules obtenues par ce moyen sont de 19 nm, 26 nm et 50 nm. Comme il est difficile d'obtenir des tailles de particules inférieures à 19 nm en utilisant du PEG-8000, un agent modificateur de surface à base d'acide oléique a été utilisé. Ainsi, avec 50 mmol de butoxyde de titane et 5 mL d'éthanol sont agités, 1,5 mL d'acide oléique a été ajouté en gouttelettes pour éviter les coagulations ou la précipitation des ions de titane. Le pH du mélange a été ajusté à 13 en utilisant une solution d'hydroxyde de potassium à 5 M après 10 min d'agitation rigoureuse. Ensuite, le baryum a été ajouté et agitée pendant 10 min supplémentaires avant d'être transférée à un conteneur en teflon d'une capacité de 23 mL. Le Teflon a été encapsulé dans un autoclave de polymère transparent aux micro-ondes de Parr Instrument et ensuite placé dans un four à micro-ondes Panasonic Inverter (2,45 GHz) fonctionnant à 360 W pendant 4 min. Après un refroidissement à température ambiante, le produit obtenu alors est lavé à plusieurs reprises dans de l'eau distillée préchauffée avant de sécher dans un four à 80 °C pendant 15 h. En plus, du BaTiO<sub>3</sub> commercialisé, de tailles 100 nm, 2 μm, et 3 μm, a été acheté de Sigma-Aldrich.

## 2.2.2 Caractérisation des échantillons

L'identification de la structure cristalline a été réalisée par la méthode de diffraction des rayons X (DRX) à l'aide d'un Diffractomètre Bruker D8 fonctionnant avec le rayonnement Cu-Kα ( $\lambda = 1,5406 \text{ \AA}$ ) à température ambiante. La plage de balayage et la taille des pas sont respectivement de 20 à 70° and 0,02°, et tous les diffractogramme sont été recueillies à température ambiante. Un microscope électronique à transmission JEOL (JEM-2100F) (TEM) fonctionnant à 200 kV a été utilisé pour caractériser les propriétés morphologiques des échantillons. Les échantillons pyroélectriques ont été dispersés dans 2 mL d'éthanol et soumis à des ultrasons pendant 20 min avant qu'une grille de Cu carbonée ne soit trempée dans la solution. Les spectres Raman sont acquises à l'aide d'un spectromètre Horiba iHR320 avec un

laser DPSS de 473 nm. Pour minimiser l'effet thermique du laser, une puissance relativement faible a été maintenue tout au long de la mesure. La lumière diffusée a été détectée par un CCD refroidi thermoélectriquement (Synapse BIDD QE). Pour les spectres Raman dépendant de la température, un Linkam THMS600 a été utilisé comme source de chauffage. Pour la comparaison directe des spectres acquis à diverses températures, toutes les données Raman brutes ont été corrigées par un facteur thermique Bose-Einstein,  $n(\omega) = \left( e^{-\left( \frac{\hbar\omega}{k_B T} \right)} - 1 \right)^{-1}$ ;  $I_R(\omega) = I(\omega)/[n(\omega) + 1]$  [216],  $I(\omega)$ ,  $\hbar$ ,  $\omega$ ,  $k_B$ , et  $T$  représentent l'intensité Raman observée, la constante de Planck réduite, la fréquence Raman, la constante de Boltzmann ( $1.38 \times 10^{-23}$  J/K) et la température, respectivement. Les études de l'absorption optique ont été réalisées par spectroscopie UV–Vis–NIR (PerkinElmer, Lambda 750). À cet effet, un substrat de quartz a été utilisé comme référence tandis que les échantillons ont ensuite été préparés par un trempage de substrats de quartz prétraités dans une solution dispersée dans l'échantillon, suivie d'un séchage à 80 °C dans un four.

### 2.2.3 Mesure de l'activité photocatalytique

La performance photocatalytique des pyroélectriques a été réalisée à l'aide d'un simulateur solaire calibré (lampe au xénon de 150 W, Modèle - #SS50AAA, PET Photoemission Tech., Inc.). Lors de mesures typiques, 50 mg de chaque échantillon ont été dispersés dans 50 mL de 20 mg/L de solution aqueuse du polluant organique modèle (méthylène orange, MO). Un équilibre d'adsorption-désorption pour saturer la surface du photocatalyseur est obtenu par agitation magnétique du mélange dans l'obscurité pendant 30 min. Comme pour Carp et al. [28], le temps dépendant de la dégradation de MO suit une cinétique L-H d'ordre 1 décrite par l'équation 2.5

$$\frac{d[C_{MO}]}{dt} = k(C_0 - [C_{MO}]) \quad (2.5)$$

où  $[C_{MO}]$  est la concentration de MO,  $C_0$  est la concentration initiale de MO et  $k$  est la constante du taux de dégradation. La concentration résiduelle de MO en fonction du temps a été calculée à partir de l'équation (1) d'Amaechi et al. [176].

## 2.3 Résultat expérimentaux et discussion

### 2.3.1 Nanoparticules de BaTiO<sub>3</sub> pyroélectrique

La cristallinité des nanoparticules telles qu'elles sont synthétisées est étudiée par diffraction de rayons X et les diffractogrammes sont décrits dans la figure 2.1(a). Tous les diffractogrammes montrent des structures polycristallines; et les pics de diffraction peuvent être bien indexés avec le groupe d'espace P4mm de la phase tétragonale selon la carte JCPDS : 01-075-1606 [166]. Les diffractogrammes montrent quelques pics de diffraction dus à la présence de phases secondaires telles que le dioxyde de titane résiduel et le carbonate de baryum.

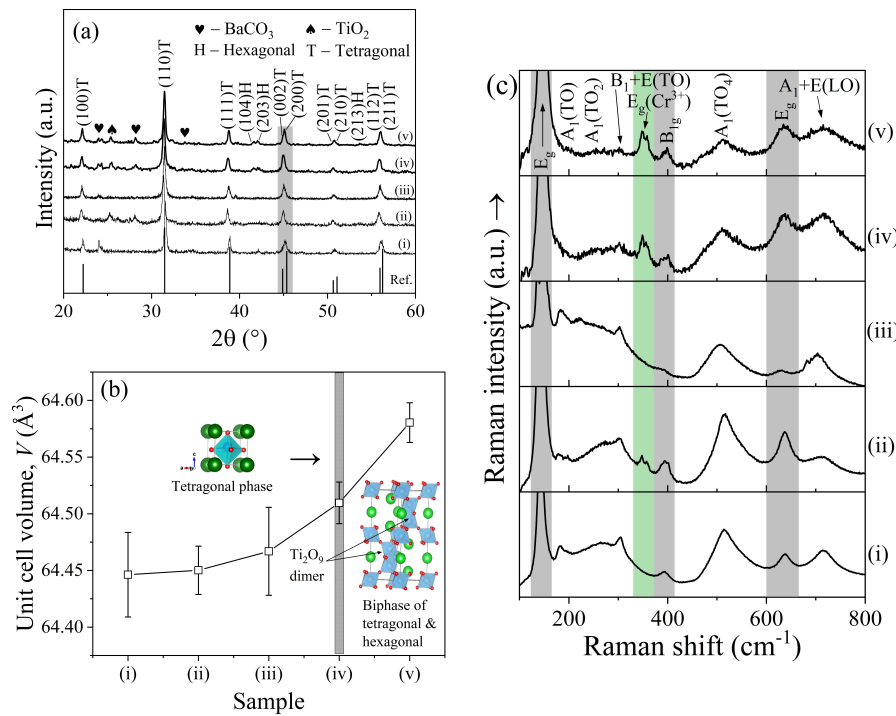


Figure 2.1: Les (a) schémas de diffraction des rayons X, (b) la variation du volume cellulaire unitaire, et (c) Spectres Raman de (i) BaTiO<sub>3</sub>, (ii) 4 mol% Cr:BaTiO<sub>3</sub>, (iii) 2 mol% Fe:BaTiO<sub>3</sub>, (iv) 4 mol% Fe 4 mol% Cr:BaTiO<sub>3</sub>, et (v) 8 mol% Fe 4 mol% Cr:BaTiO<sub>3</sub> pyroélectrique.

Malgré l'augmentation du ratio de composition du baryum au titane, c'est-à-dire  $\text{Ba}/\text{Ti} > 1$ , le diffractogramme de BaTiO<sub>3</sub> continue à montrer un pic de diffraction lié à la forme anatase de dioxyde de titane. Cela peut être dû à la faible surface du TiO<sub>2</sub>, qui limite le taux de Ba<sup>2+</sup> dissous dans la couche de TiO<sub>2</sub>. Selon le modèle de transformation *in-situ* [222], BaTiO<sub>3</sub> est formé par la diffusion continue de l'ion Ba<sup>2+</sup> dans la couche de TiO<sub>2</sub> jusqu'à ce que ce dernier est épuisé. Cependant, lorsqu'une faible surface est présentée, le taux de diffusion est limité

et la réaction est entravée, laissant une quantité résiduelle dans le matériau. La présence du carbonate de baryum est également une réaction secondaire qui résulte de l'hydroxyde de baryum et qui est probablement le dioxyde de carbone atmosphérique est dissous dans l'eau distillée utilisée pour la préparation. Apart la légère la contamination de surface, c'est-à-dire le carbonate de baryum qui est commun à la synthèse de la phase tétragonale semble être stable compte tenu du niveau de concentration de dopant. Dans les systèmes co-dopés, c'est-à-dire les systèmes figure 2.1b-(iv) et (v), l'augmentation de la concentration de l'ion Fe a donné lieu à une biphasé de symétries tétragonale et hexagonale (P63/mmc) illustrée par l'intensité croissante de la diffraction atteint des pics à  $41,4^\circ$  et  $53,8^\circ$  [165]. L'émergence de cette hétérophase s'accompagne d'une légère augmentation du volume de cellule unitaire, comme l'illustre la figure 2.1(b). En effet, pour un grand nombre de défauts, il existe un partage de facette dans le réarrangement structural du dimère  $\text{Ti}_2\text{O}_9$  en plus du partage des coins que possède la phase tétragonale pour accueillir les oxygènes vacants. Ce qui donne lieu à la phase hexagonale.

La spectroscopie Raman permet une analyse structurelle plus poussée. Les spectres Raman des échantillons mesurés à température ambiante sont indiqués dans la figure 2.1(c). Les pics Raman à environ  $185 \text{ cm}^{-1}$ ,  $270 \text{ cm}^{-1}$ ,  $306 \text{ cm}^{-1}$ ,  $519 \text{ cm}^{-1}$  et  $716 \text{ cm}^{-1}$  correspondants aux modes  $A_1(\text{TO})$ ,  $A_1(\text{TO}_2)$ ,  $B_1+E$  ( $\text{TO}_3+\text{LO}_2$ ),  $A_1(\text{TO}_3)$ , et  $A_1+E(\text{LO}_3+\text{LO}_4)$  et qui sont assignés à la phase tétragonale du titanate de baryum [166, 169, 170] généré principalement par un processus à un seul phonon. Le mode  $A_1$  est dû à une vibration en flexion de O-Ti-O alors que  $B_1+E$  est dû à une vibration en torsion de Ti-O<sub>3</sub> dans l'octaèdre et responsable de la présence d'une polarisation spontanée du matériau. Les spectres comportent d'autres modes tels que  $E_g$  à  $144 \text{ cm}^{-1}$ ,  $B_{1g}$  à  $394 \text{ cm}^{-1}$ , et  $E_g$  à  $639 \text{ cm}^{-1}$ , respectivement, et dont la signature est attribuée à la forme anatase de dioxyde du titane [171]. Un mode Raman supplémentaire par exemple en raison de la présence de chrome à l'état d'oxydation 3+ était évident à environ  $354 \text{ cm}^{-1}$  [172]. L'effet du dopage peut être observé dans le pic asymétrique à environ  $519 \text{ cm}^{-1}$  et aussi le pic à environ  $306 \text{ cm}^{-1}$ , qui est sévère, en particulier pour les échantillons co-dopés. Il réussit à affirmer que le dopage supprime la polarisation spontanée dans ces pyroélectriques dopés.

En tenant compte de la signification de la morphologie pour la catalyse, les images TEM de ces échantillons ont été examinés méthodiquement. La figure 2.2 correspond aux images TEM de la des échantillons synthétisés. Des nanograins irréguliers, mais de forme sphérique

ont été observés pour l'échantillon non dopé de BaTiO<sub>3</sub>. Malgré l'agglomération notable, des clusters de nanocristaux plus petits ont été observés à la surface des gros grains. Les grains dopés au chrome et au fer présentent deux morphologies distinctes la première étant constituée d'un mélange de nanosphères et de nanorods.

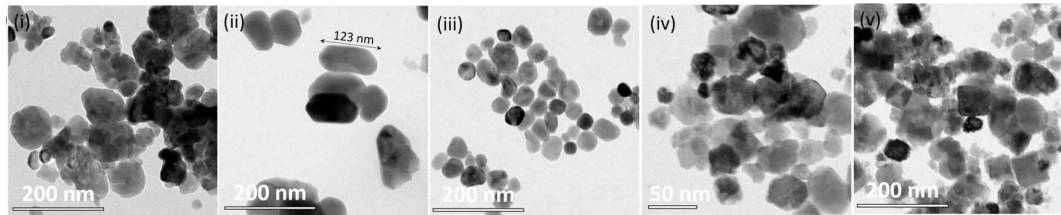


Figure 2.2: Images TEM de (i) BaTiO<sub>3</sub>, (ii) 4 mol% Cr:BaTiO<sub>3</sub>, (iii) 2 mol% Fe:BaTiO<sub>3</sub>, (iv) 4 mol% Fe 4 mol% Cr:BaTiO<sub>3</sub>, et (v) 8 mol% Fe 4 mol% Cr:BaTiO<sub>3</sub> pyroélectrique.

Par contre, le dopage de BaTiO<sub>3</sub> au Fe est principalement constitué de nanoparticules de tailles différentes. Dans les échantillons co-dopés, ces nanorods se transforment progressivement en nanocubes avec l'ajout de fer. La suppression prononcée des structures de type nanorod en (v), est une indication de la présence des régions de défauts répartis de manière inhomogène [176].

Les spectres d'absorption UV-Vis des échantillons mesurés dans la gamme 250 - 800 nm sont indiqués en figure 2.3. L'absorption optique dans le BaTiO<sub>3</sub> est l'excitation entre les états O 2p et les états Ti 3d. Le bord d'absorption de l'échantillon non dopé s'est avéré être ca. 390 nm ( $\sim 3,18$  eV). Il a été observé que les systèmes dopés présentent une absorption amplifiée de la lumière visible en raison de la présence des défauts.

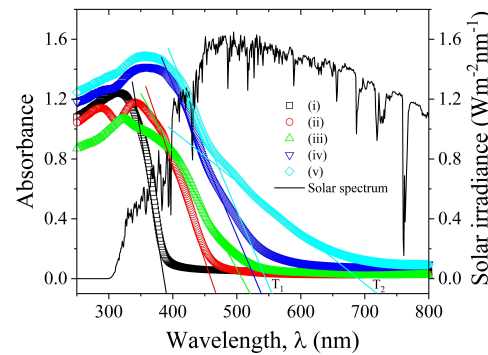


Figure 2.3: Les spectres d'absorption optique des photocatalyseurs tels que synthétisés.

En principe, la nature multivalente des métaux aliovalents utilisés pourrait probablement induire une excitation optique de la paire à couplage d'échange Cr<sup>3+/4+</sup> ou Fe<sup>2+/3+</sup> (et même

les deux dans le cas d'échantillons co-dopés), ce qui entraîne un plus grand nombre de bandes de défauts causés par une forte densité en oxygène vacants [185]. L'absorption de lumière supplémentaire présente un avantage en termes de la récolte de lumière visible et important pour les applications photocatalytiques activées par la lumière visible qui sera discuté par ensuite.

L'activité photocatalytique des pyroélectriques a été évaluée par photodégradation de la solution aqueuse de méthylène orange (20 mg/L) sous irradiation solaire simulée. La courbe de la variation de la durée l'absorption pour la photodégradation de ce polluant organique est indiquée dans la figure 2.4(a). Les résultats indiquent une modification de la concentration de la solution aqueuse de méthylène orange avec le temps d'irradiation sur les photocatalyseurs. Sous illumination, l'effet photocatalytique est visible comme observé dans les traces cinétiques.

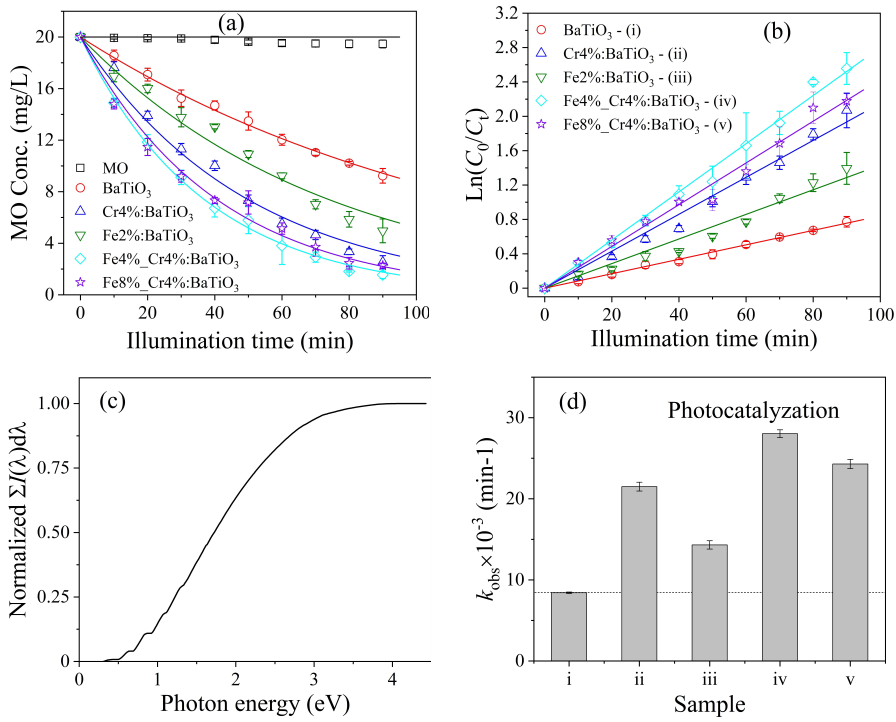


Figure 2.4: (a) La variation de la photodégradation du méthylène orange en fonction du temps sur des pyroélectrique synthétisés, (b) la variation de la cinétique de la photodégradation en fonction du temps (c) la courbe de la variation de l'énergie des photons par rapport l'irradiation spectrale intégrée sur toutes les longueurs d'onde du spectre solaire, et (d) bar graphique montrant les constantes de la vitesse de réaction obtenues pour la catalyse photochimique. Les lignes solides représentent les ajustements (a) exponentiels et (b) linéaires des données.

Les processus cinétiques suivent le mécanisme de Langmuir-Hinshelwood du premier ordre [28] et la courbe de  $\ln(C_0/C_t)$  en fonction du temps d'illumination,  $t$  a été utilisée pour déterminer

la constante de vitesse dégradation. Les pyroélectriques dopés présentent une meilleure activité photocatalytique par rapport à l'échantillon non dopé. Généralement, la constante de vitesse de photodégradation est connue pour avoir une dépendance de la une puissance sur l'intensité lumineuse ( $n$ ), de l'activité quantique sur la gamme de longueurs d'onde du photocatalyseur absorbées ( $\emptyset$ ) et le nombre de photons absorbés par le photocatalyseur ( $I_a$ ) exprimé comme  $k \propto (\emptyset I_a)^n$ ; et  $0.5 < n < 1$  pour les fortes et faibles intensités, respectivement [186, 187]. Le terme ( $\emptyset I_a$ ) est amplifié et de même pour la constante de vitesse de photodégradation des pyroélectriques dopés. Nous avons déduit quantitativement l'étendue de l'absorption des photons à partir de la courbe de l'énergie des photons contre l'irradiation solaire normalisée intégrée sur toutes les longueurs d'onde du spectre solaire comme indiqué à la figure 2.4(c).

On a observé que le BaTiO<sub>3</sub> pyroélectrique dopé au Cr a un meilleur pouvoir photocatalytique par rapport au BaTiO<sub>3</sub> non dopé, et cela est principalement dû à l'amplification de l'absorption de la lumière. En figure 2.4(c), elle absorbe près de 12,2% du spectre solaire contrairement aux 3,9% absorbés par la poudre de BaTiO<sub>3</sub>. Cette amélioration, en plus de la naissance de la contribution de champ cristallin à la forte activité photocatalytique observée dans l'échantillon de BaTiO<sub>3</sub> dopé au Cr. Nous tenons à mentionner à ce stade que l'activité catalytique de notre échantillon dopé au chrome a surpassé celles de Srilakshmi et al. [36] qui ont démontré une absorption de 63,4% recalculée à 90 min, utilisées pour la réduction du nitrobenzène en aniline. Pour exploiter davantage de la lumière cueillie, la structure de BaTiO<sub>3</sub> dopé au Cr a été de nouveau dopée au fer (Fe) avec un ratio de composition molaire du fer et du chrome, 1:1 et 2:1. Il a été observé que l'utilisation des deux dopants à base de métaux de transition améliore encore les performances grâce à une photo-absorption prolongée. Par exemple, le 1:1 et le 2:1 absorbent environ 24,5% et 51,1%, respectivement. L'effet indésirable du co-dopage se met en place immédiatement, la teneur en Fe a été augmentée au-dessus de 4 mol%. Cela implique que, malgré l'avantage de l'absorption de la lumière, la propriété bulk du matériau est censée assurer la séparation des anciens porteurs de charge, ce qui améliore la réactivité de surface est compromis. Par conséquent, la teneur supplémentaire en Fe permet la réduction du nombre de sites actifs en surface, aboutissant à des centres de recombinaison qui limitent la charge globale de la consommation catalytique [27]. La composition molaire 1:1 a un taux de dégradation constante d'environ  $(28.0 \pm 0.5) \times 10^{-3} \text{ min}^{-1}$ , ce qui est 3,3 et 1,3 fois plus efficace que le Prostine et le BaTiO<sub>3</sub> dopé au Cr . Toutefois, l'utilisation du chrome est injustifiée, car il est considéré comme un métal lourd et toxique surtout à l'état

hexavalent. Nous avons contourné ce problème en dopant la même structure avec le fer (Fe) uniquement, car il ne pose aucun problème dans aucun état de valence. Cela a donné une capacité d'absorption de la lumière de 21%, ce qui implique que le dopage au fer étend la bande d'absorption plus loin dans la région visible par rapport au dopage au chrome. Il est intéressant de noter que nous avons déterminé une dégradation constante de vitesse de  $(14.3 \pm 0.5) \times 10^{-3} \text{ min}^{-1}$ , ce qui est 1,7 fois mieux que le BaTiO<sub>3</sub> pyroélectrique.

### 2.3.2 L'effet de la taille des particules sur l'activité photocatalytique des particules polaires de BaTiO<sub>3</sub>: Thermodynamique et Landau-Ginzburg-Devonshire (LGD) phénoménologique approches

Dans cette sous-section, les propriétés microstructurales des échantillons sont examinées, mais le focus est sur l'impact de la taille des particules sur le transport photocatalytique et le transport cinétique du titanate de baryum polaire. Les approches basées sur les données de Landau-Ginzburg-Devonshire (LGD) (pour la structure) et thermodynamique (pour le transport de masse) ont été déployées pour analyser la dépendance de la taille observée à l'échelle nanométrique. Des images TEM représentatives des échantillons de 9 nm à 3 μm sont présentées dans la figure 2.5(a) – (g).

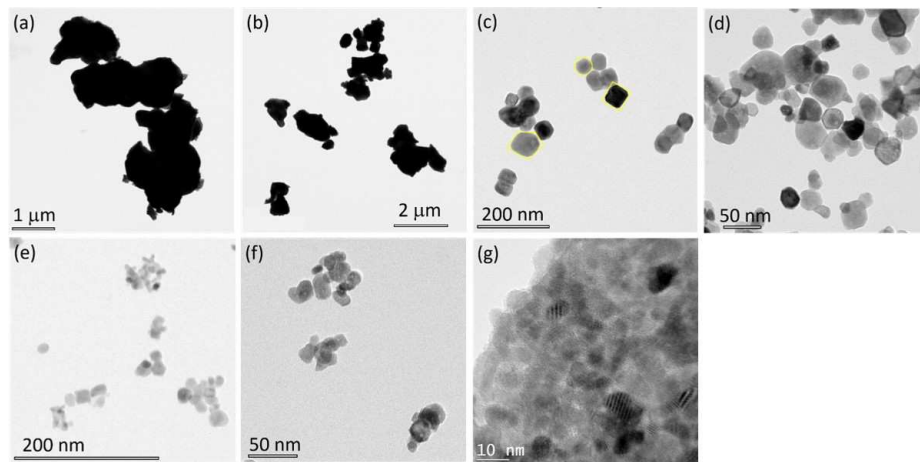


Figure 2.5: Images TEM de (a) 3 μm, (b) 2 μm, (c) 100 nm, (d) 50 nm, (e) 26 nm, (f) 19 nm, et (g) des particules de titanate de baryum de 9 nm.

Les particules (2 μm et 3 μm) sont principalement des particules non sphériques et des agglomérats. La poudre composée de nanostructures formées de 19 à 100 nm montre de formes quadrilatérales et sphériques alors que la poudre de 9 nm est constituée d'amas et forte-

ment agrégée. Les diffractogrammes des particules sont présentés la figure 2.6(a). Alors que la poudre de 9 nm qui a cristallisé en phase cubique, les autres échantillons ont cristallisé en phase tétragonale selon les cartes JCPDS #: 01-075-0213 et 01-089-1428, respectivement [132, 170]. Par rapport à la DRX de la figure 2.1(a), aucun pic de diffraction ne correspond au  $\text{TiO}_2$  résiduel a été observé, indiquant une réaction complète des précurseurs. Le pic de diffraction correspondant à la contamination de surface du  $\text{BaCO}_3$  était présent dans les deux phases. Il s'agit d'une réaction secondaire culminant de l'hydroxyde de baryum, probablement le dioxyde de carbone est dissous dans l'eau distillée utilisée pour la préparation. Le fait de ne pas pouvoir détecter le pic des échantillons en bulk peut être dû au fait que la concentration est inférieure à la limite de détection de XRD considéré comme étant de 5% [194].

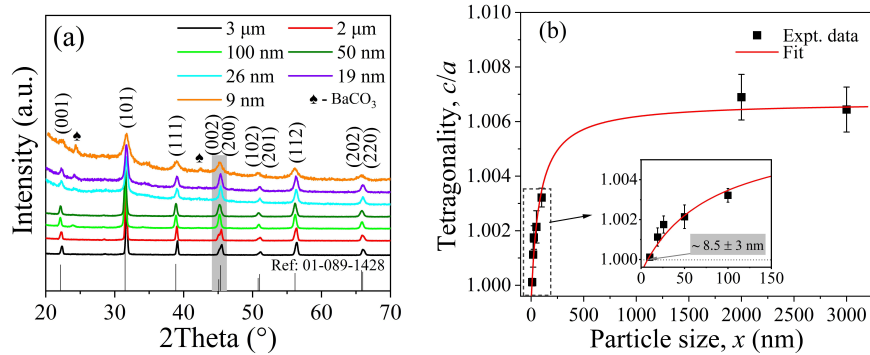


Figure 2.6: (a) Diffractogramme de rayon X et (b) la tétragonalité, le rapport  $c/a$  des tailles de particules en poudres de titanate de baryum. L'encadré (b) présente une vue élargie du rapport  $c/a$  dans la plage, 0 - 150 nm.

Les paramètres de la maille,  $a$  et  $c$ , sont ensuite déterminés à l'aide de raffinements de maille et le ratio, i.e. la tétragoanlité en fonction de la taille des particules est présentée en figure 2.6(b). Un rapport de tétragoanlité une diminution de la tétragonalité a été constatée entre pour des tailles de 19 et 100 nm, et se rapproche de l'unité pour une taille limite. C'est ce que l'on appelle la taille critique, qui représente la limite lorsque le moment dipolaire approche de zéro [197]. La relation empirique [139] a été utilisée pour dénier la relation entre la tétragonalité et la taille des particules. Nous avons obtenu une taille de particules de  $\sim 8.5 \pm 3$  nm ce qui est tout à fait comparable à ce qui a été rapporté dans la littérature [198, 199].

La transition de phase peut être décrite par la dynamique des vibrations des phonon [198] et a donc été étudié par la spectroscopie Raman. Lorsque la taille des particules est réduite, un changement de la phase de transition se produit et, à l'équivalent, une réduction spectaculaire

de la température de Curie, sinon la transition de phase en fonction de la température. Par conséquent, l'étude par la spectroscopie Raman en fonction de la température permet de déterminer la température de transition/Curie,  $T_C$  de ces particules spécialement pour les modes Raman, c'est-à-dire  $B_1+E$  et  $A_1+E$ , qui sont sensibles à la température. La figure 2.7(a) montre la courbe de l'intensité Raman normalisée en fonction de la température des particules et l'intersection du t (ligne rouge continue) avec l'axe de la température est prise comme  $T_C$ . Comme prévu, la  $T_C$  diminue avec la taille des particules (figure 2.7(b)) et avec la valeur empirique [139], une taille critique de  $11,5 \pm 2$  nm a été obtenue à température ambiante, à  $25^\circ\text{C}$  et celle-là est en excellent accord avec le rapport de Zhao et al. [203].

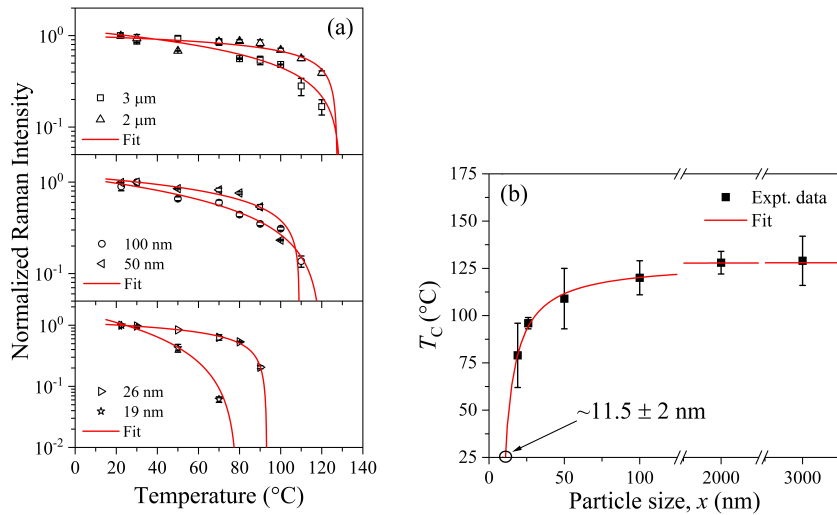


Figure 2.7: (a) Variation de l'intensité Raman normalisée du pic  $B_1+E$  en fonction de la température, (b) la variation de la taille estimée des particules de fonction de  $T$ .

D'après l'étude de la variation de l'absorption de MO en fonction du temps, la performance photocatalytique est évalué en fonction de la constante apparente de la vitesse de la réaction. La figure 2.8 montre la courbe de  $\ln(C_0/C_t)$  en fonction du temps d'irradiation,  $t$  utilisé pour déterminer la constante de la vitesse de réaction. La cinétique montre deux régimes distincts, à savoir 0 – 30 min pour un processus rapide et 30 – 60 min pour un processus légèrement lent. Le processus rapide est attribué au mécanisme L-H du premier ordre alors que l'écart par rapport à la partie linéaire (c'est-à-dire le processus lent) peut être expliqué par une compétition entre le taux de dégradation et la désorption du colorant. Les points de données de la figure 2.9 indiquent les constantes de vitesse de réaction estimées. La constante de vitesse de réaction augmente jusqu'à 19 nm avant de diminuer pour les particules plus petites. Alors

que cela est vrai pour l'augmentation de la superficie (c'est-à-dire le nombre croissant de sites actifs), qui augmente inversement à la diminution en taille de particules, il y a une limite due à l'instabilité du domaine qui contient les sites actifs. À l'échelle nanométrique, la taille de la particule est comparée à la moyenne du trajet libre des porteurs excités et donc de tous les porteurs de charge excités qui contribuent à la charge catalytique consommée. En dessous de cette taille, L'activité baisse immédiatement. Ce comportement peut être associé à la perte d'énergie de l'effet photovoltaïque du bulk est attendu pour les particules en dessous d'une taille critique pour la transition vers une structure centrosymétrique.

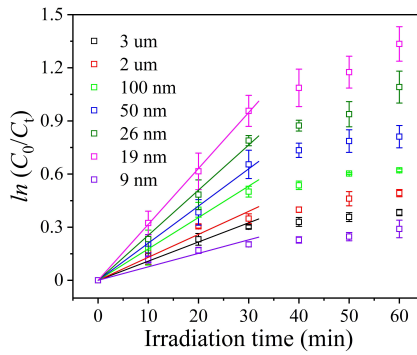


Figure 2.8: Le graphique de  $\ln(C_0/C_t)$  en fonction du temps d'irradiation,  $t$ .

Pour étudier l'effet de la taille intrinsèque sur  $k(x)$ , la fonction empirique similaire à celles trouvée dans Ishikawa et al. [139] et un modèle thermodynamique basé sur l'équation 2.4 sont déployés. Par conséquent la fonction empirique pour la vitesse de la réaction en fonction de la taille peut s'écrire comme

$$k(x) = k(\infty) \left[ 1 - \frac{C}{x - x_0} \right] \quad (2.6)$$

où  $k(x)$ ,  $k(\infty)$ , et  $x_0$  sont la vitesse de réaction pour différentes tailles de particules, la vitesse de réaction pour la poudre en bulk, et la taille critique, respectivement. Les ajustements numériques aux données sont indiqués en figure 2.9(a) et (b) pour les deux modèles.

Pour le formalisme thermodynamique, il convient surtout pour une phase continue de particules [141, 142] et présente une oxydation photocatalytique maximale dans la gamme de 15 à 25 nm avant la diminution. C'est la taille en dessous de laquelle la nanoclusterie et la reconstruction de surface domine [208]. Sur la base du modèle LGD, le résultat de l'ajustement génère  $k(\infty) = (12,0 \pm 1,0) \times 10^{-3} \text{ min}^{-1}$  et  $x_0 = 8,3 \pm 2,0 \text{ nm}$ , où  $x_0$  est en bon accord avec les analyses précédentes. La taille critique des particules montre ici la taille physique pour

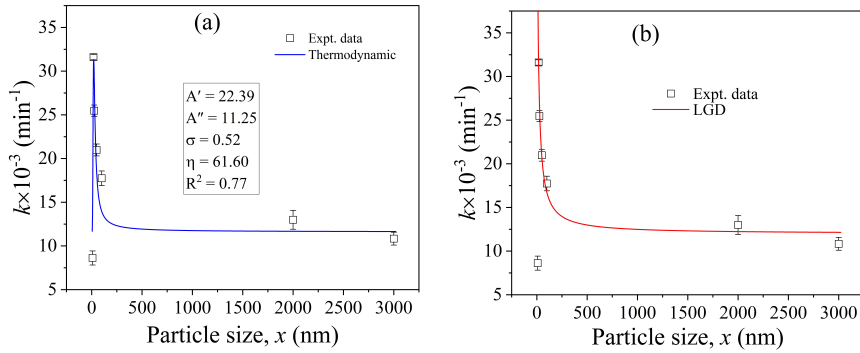


Figure 2.9: La courbe de la variation de  $k$  en fonction de la taille des particules. Les traits solides sont les ajustements numériques selon (a) l'équation 2.4, et (b) l'équation 2.6.

laquelle le moment dipolaire existe toujours dans le cristal. Nous montrons donc cette non-centrosymétrie, une propriété du matériau qui dépend de la taille des particules induit la cinétique de l'activité photocatalyse de BaTiO<sub>3</sub>. De plus, les paramètres de Polanyi  $\alpha$ , et  $\eta$ , sont obtenus à partir de la valeur de l'ajustement sont de 0,52 et 61,60, respectivement, et a été utilisé pour déduire l'énergie de surface des particules à la température ambiante. Sur la base de la taille critique des particules obtenues à partir du modèle LGD, l'énergie de surface de  $8,2 \pm 2 \text{ J/m}^2$  a été déterminée.

## 2.4 Conclusion

L'approche hydrothermale assistée par micro-ondes s'avère reproductible et surtout, évolutive. Cette étude a montré qu'en termes de photo-absorption, le dopage au chrome est bon, mais meilleur avec du fer. Bien que l'utilisation de la lumière soit bénéfique à la photocatalyse, mais sa coexistence avec l'effet photovoltaïque du bulk fournit par la brisure de la symétrie d'inversion du cristal permet une synergie nécessaire pour la séparation des transporteurs à la charge. La performance photocatalytique a été expliquée en termes d'utilisation et la récolte de lumière supplémentaire cueillie, l'effet de la teneur en fer et la tétragonalité qui est une évaluation directe de la propriété du bulk responsable de la séparation du transporteur de charge. La voie de synthèse nous a permis de synthétiser des particules qui ont été comparées à des particules commercialisées. Cette voie de préparation permet d'obtenir des particules de grande pureté et moins d'agglomération avec une tétragonalité élevée contrairement à la voie hydrothermale classique qui permet d'avoir des particules qui se cristallisent.

dans une phase cubique de moindre tétragonalité et parfois de grande symétrie. Nous avons développé une compréhension complète des propriétés structurales en examinant l'évolution de la tétragonalité et de la température de Curie. Alors que la meilleure performance photocatalytique a été obtenue avec la poudre de 19 nm avant la diminution, tant thermodynamique que phénoménologique LGD formalisme ont été proposés pour interpréter les résultats expérimentaux en ce qui concerne le transport des masse à l'interface photocatalyseur-liquide et la structure cristalline, respectivement. En conclusion, nous avons non seulement déterminé la taille optimale des nanoparticules de titanate de baryum pour une activité photocatalytique amplifiée, mais a également poussé sa taille critique à une valeur encore plus faible.